# Fatigue-creep-environment interactions in notched specimens of Ti6246.

**Bryant, Marc Andrew**

# Fatigue–Creep- Environment Interactions in Notched Specimens of Ti6246

By

Marc Andrew Bryant (BEng hons)

Submitted to the University of Wales in fulfilment of the requirements for the Degree of Doctor of Philosophy

Swansea University

2007

## SUMMARY

The continuing drive for efficiency in gas turbine development leads to higher operating temperatures. Ti6246 is an example of an alloy that has continued to thrive due to increased understanding of the interactions of fatigue, creep and environmental damage mechanisms at these increased temperatures. These damage mechanisms, however, are of particular concern at critically stressed features of these components. Therefore there is a requirement to understand the relative contributions of these damage mechanisms to material life, particularly at stress concentrations where fatigue cracks often initiate.

This programme attempts to address these issues for the titanium alloy Ti6246, commonly used in compressor disc applications, though a series of fatigue tests at ambient and elevated temperatures. Strain control tests were conducted using cyclic and dwell waveforms, providing information on cyclic deformation behaviour. Load control tests on notched specimens were performed in air and hard vacuum ($10^{-6}$ Torr), using cyclic and dwell waveforms, allowing the relative effects of fatigue, creep and environment to be partitioned. Crack propagation testing was also conducted on plain and notched specimen geometries under cyclic and dwell conditions. The resulting fracture surfaces were then subjected to analysis to determine the effect of these test conditions on crack initiation and propagation behaviour.

Creep and environmental effects were shown to greatly enhance both fatigue initiation and crack propagation rates at high temperatures, with the environment being the most damaging mechanism. In air, a transition in damage mechanism was seen at high stresses where the material undergoes plastic deformation. This was attributed to ingress of environmental species due to oxide cracking.

## ACKNOWLEDGMENTS

I would like to thank my academic supervisor Professor W.J. Evans (Swansea University) for providing me with guidance and continued support throughout this programme of work.

I would also like to thank my industrial supervisor Mr Paul Webster (Rolls-Royce Plc) for supplying materials and assistance.

Swansea University for providing access to a pool of knowledge via their library and I thank them and the Interdisciplinary Research Centre (IRC) for access to its resources and facilities.

A particular mention is made to Dr Mark Whittaker whose technical assistance and support was invaluable.

Financial support from Rolls-Royce Plc and EPSRC via studentship funding is also gratefully acknowledged.

Finally, I wish to thank my parents who's love and support was never found wanting, and Joanne for her love and endless patience.

## DECLARATIONS AND STATEMENTS

DECLARATION

This work has not previously been accepted in substance for any degree and is not being concurrently submitted in candidature for any degree.

Signed ... .....(candidate)

Date .....23/ 8/ 2007.....

STATEMENT 1

This thesis is the result of my own investigations, except where otherwise stated.

Other sources are acknowledged by footnotes giving explicit references. A bibliography is appended.

Signed .... .....(candidate)

Date .....23/ 8/ 2007.....

STATEMENT 2

I hereby give consent for my thesis, if accepted, to be available for photocopying and for inter-library loan, and for the title and summary to be made available to outside organisations.

Signed ... .....(candidate)

Date .....23/ 8/ 2007.....

## CONTENTS

## 1.0 INTRODUCTION

Titanium alloy development has been instrumental to the advancement of the gas turbine during the latter half of the 20th century. α/β titanium alloys have proven to be particularly useful, with a comparatively low density and excellent corrosion resistance combined with a high operating temperature. These properties have resulted in their continued use in critical rotating components such as discs and blades in the low to high pressure sections of the compressor. The continuing drive to increase engine efficiency however, will mean titanium alloy systems employed in future gas turbine designs will operate under regimes of stress and temperature where the interaction of fatigue, creep and environmental damage shall limit life. This is a situation that will continue in the medium to short term since replacement materials such as metal matrix composites and intermetallics, are expensive to develop, difficult to manufacture and are unproven under service conditions (*Bache 2003*).

The effects of these interactions may reduce the effectiveness of current fatigue design methods, resulting in dangerously inaccurate component life predictions. The main areas of concern on discs are geometry induced stress raisers, particularly in the high-pressure compressor.

Generally, the fatigue life at these stress raisers is determined on the basis of notch design curves or through the use of strain control data. The latter method is based on the assumption that the material in a critical region of the notch root behaves in a similar way to a plain specimen undergoing strain control deformation due to it being constrained by the bulk material surrounding it.

This work considers the strain control response and notch behaviour of the $\alpha+\beta$ titanium alloy Ti6246 at ambient temperatures and temperatures where fatigue, creep and environment interact. In order to assess the relative contributions of these mechanisms to fatigue life, a series of strain and load control tests were carried out in air and vacuum, under cyclic and dwell waveforms, with crack propagation testing also conducted under these conditions.

## 2.0 LITERATURE REVIEW

### 2.1 STAGES OF FATIGUE

Fatigue is defined as a term which applies to changes in properties which can occur in a material due to the repeated application of stresses or strains, although usually this term applies specially to those changes which lead to cracking or failure (General Principles for Fatigue Testing of Metals, 1964). The fatigue process can be divided into the following stages:

**Stage I** is the nucleation (initiation) event during which microstructurally small cracks form. Under laboratory conditions it is difficult to define a point of initiation, since it can be defined as the point of nucleation of flaws along persistent slip bands. In engineering situations a pseudo initiation point is utilized, which in the case of gas turbines, is defined as the development of a 0.75mm surface flaw. This definition includes crack propagation as well as initiation. Since engineering materials contain defects and inclusions, crack growth may also be considered to have begun from the first load application, Suresh 2003 and Evans 2003.

**Stage II** is the short crack growth period where the crack path is heavily influenced by microstructure. The crack and plastic deformation zone surrounding the crack tip are confined to within a few grain diameters. Here, crack growth occurs mainly by single shear in the direction of the primary slip system, resulting in a zig-zag crack path. Therefore stage II fracture surfaces exhibit a serrated or faceted profile, Suresh 2003 and Evans 2003.

**Stage III** is when the crack is sufficiently large for growth rate behaviour to be quantified by linear elastic fracture mechanics. At these higher stress intensity range values, the crack tip plastic zone encompasses many grains. This stage of crack growth involves simultaneous or alternating flow along two slip systems. This slip mechanism results in a planar (mode I) crack path normal to the tensile axis. Stage III crack growth leads to the formation of fatigue striations in titanium alloys.

A plot of log d$a$/d$N$ versus log$\Delta K$ for most engineering alloys has a sigmoidal variation, where it can be seen that there are three identifiable regimes of fatigue crack growth. The first regime is associated with the threshold stress intensity factor range $\Delta K_0$, where the average growth increment per cycle is smaller than a lattice spacing. Below the threshold cracks remain dormant or grow at an undetectable rate. Above the threshold there is a steep increase in log d$a$/d$N$ with log$\Delta K$. The second regime is known as the Paris regime and exhibits a linear variation of log d$a$/d$N$ with $\Delta K$, while the third regime corresponds to the range of high $\Delta K$ values where crack growth rates increase rapidly towards catastrophic failure.

Using analytical methods, *Westergaard 1939* and *Irwin 1957* quantified the near-tip fields for the linear elastic crack in terms of the stress intensity factor, K, which is a measure of the strength (a scale factor) of the stress field in the vicinity of crack tip and is given by:

$$K = \sigma\sqrt{\pi a} \qquad (2.1)$$

where a is the length of an edge crack, or half length of a centre crack. *Suresh 2003*

*and Evans 2003.*

**Stage IV** is the final stage of rapid growth as the fracture toughness is approached. *Suresh 2003* and *Evans 2003.*

## 2.2 Cyclic stress-strain response

Cyclic deformation behaviour refers to a continuous change in the cyclic strength that may occur throughout a test or at least in the first stage of cyclic deformation. Examples of cyclic hardening and cyclic softening (Figures 2.1 and 2.2) (*R. Schubert et al, 1989*), show the stress course and the hysteresis loop shape from a stress-controlled test performed applying a triangular signal with constant amplitude. Cyclic hardening leads to an increase in the stress amplitude, resulting in a larger hysteresis loop. Cyclic softening has the opposite effect: a decrease of $\Delta\sigma/2$ and a reduction of the size of the hysteresis loop. The type of behaviour is mainly determined by the pre-treatment of the material, for example, cold working prior to cyclic loading may result in subsequent cyclic softening, whereas a recrystallization treatment could lead to cyclic hardening.

Asymmetrical cyclic deformation result in transient processes that tend to reduce asymmetry. Figure 2.3 shows a strain-controlled test in which a mean strain is superimposed, resulting in a mean stress arises that slowly diminishes. This process is termed cyclic relaxation. If the test is performed under stress control and a mean stress is applied, the material may show cyclic creep. The mean strain increases continuously, leading to a steady shift of the hysteresis loop to the right.

## 2.3 FATIGUE LIFING METHODS

### 2.3.1 Total-life Approaches

Traditional fatigue design methods involve the characterisation of total fatigue life to failure in terms of the cyclic stress range (the S-N curve) or the strain range approach. The fatigue life incorporates the number of cycles for crack initiation (up to 90% of total life) and propagation to failure. Since crack initiation life forms a major component of the total fatigue life (in smooth tests specimens), traditional stress and strain-based methods often represent design against fatigue crack initiation. In high-cycle low stress conditions, the material primarily undergoes elastic deformation, with fatigue life characterized in terms of the stress-range. Under low-cycle fatigue, stresses are high enough to cause plastic deformation prior to failure, therefore fatigue life is characterized in terms of the strain-range, Suresh 2003.

Total fatigue-life is characterised as function of variables such as the applied stress range, strain range, mean stress and environment. These methodologies combine the damage evolution, crack nucleation and crack growth stages of fatigue into a single, experimentally characterisable continuum formulation, *Suresh 2003*.

### 2.3.2 Stress-life Approach

The stress-life approach was introduced in the 1860s by Wohler *(Wohler, 1867)*. This empirical method is widely used in fatigue analysis, mostly in high cycle fatigue (HCF) applications, where low amplitude cyclic stresses cause primary elastic deformation in a component designed for long life, *(Suresh 2003 p.221)*.

### 2.3.3 The Fatigue Limit

The standard stress-controlled test involves running specimens to failure under a constant amplitude load cycle. A stress-life graph (S-N curve) is then plotted to reveal the stress dependence of the fatigue response. Three specific regimes can be identified. Lives from $10^3$ to $10^5$ cycles are known as low cycle fatigue and lives of $10^5$ to $>10^7$ cycles are called high cycle fatigue (HCF). Beyond $10^6$ cycles the stress-life plot plateaux. This condition is known as the endurance limit, $\sigma_e$. Below this level, ferritic steels may be cycled indefinitely without failure, while austenitic steels and non-ferrous metals $\sigma_a$ (stress amplitude) continue to decline at a shallow angle. Under theses conditions the endurance limit is defined as the stress amplitude the material can support for at least $10^7$ cycles. (Suresh, 2003, p.222 and Evans 2003, p.61)

### 2.3.4 Strain-life approach

When considerable plastic deformation occurs during cyclic loading (e.g. as a result of high stress amplitudes or stress concentrations) the fatigue life is markedly shortened, i.e. low cycle fatigue (LCF). Realizing the importance of plastic strains in causing permanent fatigue damage, Coffin (1954) and Manson (1954) , (Coffin, 1954, p.931-950. and Manson, 1954) independently proposed a plastic strain-based continuum characterization of LCF. (Suresh 2003, p.221)

### 2.3.5 Strain-based Approach to Total Life

Information derived from cyclic stress based continuum analysis mainly applies to elastic and unconstrained deformation. Engineering components, however,

tend to undergo a degree of structural constraint and plastic flow, particularly at stress concentrations. Under these conditions the strain-life approach is considered.

More detailed quantitative procedures have been developed for handling strain control data, giving the approach greater appeal for design and component lifing schemes. Strain control testing may be considered a more appropriate method for LCF testing, while stress control is better suited to HCF as endurance limit assessments. At long lives material response is essentially elastic, so strain and stress control tests should show similar behaviour at a given R-value.

Data is typically plotted as strain range against cycles to failure, with the resultant graph being divided into elastic and plastic components. This is achieved by constructing a tangent to the long life data, forming the elastic component. Then, by subtracting the elastic component from the total strain, the plastic component is obtained. A third regime, defined as the transition life, can be identified where the elastic and plastic lines intersect.

Shorter lives dominated by plastic strain represent LCF behaviour, where the material is controlled by ductility, while lives just in excess of the transition represent an intermediate regime. HCF behaviour occurs when the elastic line becomes asymptotic to the fatigue data and fatigue life is dictated by the rupture strength of the material. Optimising the overall fatigue properties therefore requires a balance between strength and ductility (Mitchell 1978)

The following equations give a mathematical representation of the division into elastic and plastic components:

$$\Delta\varepsilon_t = \Delta\varepsilon_e + \Delta\varepsilon_p \qquad (2.2)$$

$$\Delta\varepsilon_t = C_e N_f^{\alpha_2} + C_p N_f^{\alpha_1} \qquad (2.3)$$

where; $\Delta\varepsilon_t$ = total strain

$\Delta\varepsilon_e$ = elasticity component

$\Delta\varepsilon_p$ = plasticity component

$\alpha_1$ = gradient of plastic line (or fatigue ductility exponent: 0.5 – 0.7 for most metals)

$\alpha_2$ = gradient of elastic line ( or Basquin's exponent)

$C_p$ = plastic strain range at one cycle (or ductility coefficient, or $\varepsilon_f'$)

$C_e$ = elastic strain range at one cycle (or $(\sigma_f' / E)$, where $\sigma_f'$ = fatigue strength coefficient and $E$ = elastic modulus.

Therefore, the plasticity component $\Delta\varepsilon_p = \varepsilon_f'$ and is known as the Manson-Coffin equation. This equation is limited however, since it makes no allowance for the endurance limit or mean stress effects. The following modification was proposed by Manson to accommodate this omission:

$$(\Delta\varepsilon_t - \Delta\varepsilon_e') = \varepsilon_f' N_f^{\alpha_1} \qquad (2.4)$$

where: $\Delta\varepsilon_e'$ = endurance strain range.

To allow for mean stress, Sachs introduced a further modification:

$$(\Delta\varepsilon_t - \Delta\varepsilon_e') = (\varepsilon_f' - \varepsilon_m) N_f^{\alpha_1} \qquad (2.5)$$

where: $\varepsilon_m$ = mean strain (Suresh 2003, p.256-259) and (Evans 2003, p.63-64).

### 2.3.6 Damage-tolerant Approach

The fracture mechanics approach to fatigue design involves a damage-tolerant philosophy, which assumes that all engineering components are inherently flawed. The pre-existing flaw size is determined via a non-destructive detection technique.

Where no flaw is detected the initial crack size is considered to be the resolution of the detection technique. The useful fatigue life is defined as the number of cycles to propagate the crack from the initial size to a critical dimension, which may be based on the materials' fracture toughness.

Crack propagation life prediction using the damage tolerant-approach involves empirical crack growth laws based on fracture mechanics. With respect to linear elastic fracture mechanics, the damage-tolerant method applies under conditions of small-scale yielding (away from plastic strain field of any stress concentrations) and where mainly elastic loading conditions apply.

This inherently conservative approach is widely used in fatigue-critical applications for low cycle fatigue, such as the aerospace industry (Suresh 2003, p.13).

### 2.3.7 Fracture mechanics approach

When cyclic stresses applied to a component are sufficiently small that the zone of plastic deformation ahead of the advancing fatigue crack is a minor perturbation in an overall elastic field, linear elastic fracture mechanics provide appropriate continuum descriptions for fatigue fracture. Paris, Gomez & Anderson 1961 (Paris 1961) and Paris & Erdogan 1963 (Paris & Erdogan 1963) suggested that for a cyclic variation of the imposed stress field, the linear elastic fracture mechanics characterization of the rate of fatigue crack growth should be based on the stress intensity factor range:

$$\Delta K = K_{max} - K_{min} \qquad (2.6)$$

where $K_{max}$ and $K_{min}$ are the maximum and minimum values of the stress intensity factor during a fatigue stress cycle.

Paris, Gomez & Anderson (1961) and Paris & Erdogan (1963) also showed that the fatigue crack growth increment $da/dN$ is related to the stress intensity factor range by the power law relationship:

$$\frac{da}{dN} = C(\Delta K)^m \qquad (2.7)$$

where:

a = crack length

C and m = scaling constants (influenced by microstructure, environment, temperature and load ratio, R). (Suresh 2003, p.332-333)

## 2.4 NOTCHES

### 2.4.1 Effects of Stress Concentrations

Engineering structures invariably contain stress concentration sites, which are the main sites for the initiation of fatigue cracks. The stress and deformation fields in the immediate vicinity of the stress concentration have a strong influence on how the fatigue cracks nucleate and propagate. This stress concentration is described by a factor $K_t$ where:

$$K_t = \frac{\textit{minimum localised elastic stress}}{\textit{nominal stress}} \qquad (2.8)$$

In addition to raising the stress, a notch also creates a biaxial or tri-axial stress field. In practice, the reduction in fatigue strength at a given stress is often less than the $K_t$ factor indicates. This is due mainly to the fact that many notches do not remain in an elastic state under fatigue loads. Stresses at notches can be high enough to induce plastic flow, allowing the stress to redistribute and reduce at the notch surface. The reduction in fatigue strength due to a notch can be characterised by the fatigue notch factor $K_f$ where:

$$K_f = \frac{\textit{fatigue strength of unnotched specimen}}{\textit{fatigue strength of notched specimen}} \qquad (2.9)$$

The level of agreement between theoretical predictions of elastic stress concentration and actual effects is measured by the notch sensitivity index, defined as:

$$q = \frac{K_f - 1}{K_t - 1} \qquad (2.10)$$

The parameter $q = 0$ for no notch effect and $q = 1$ for the full effect predicted by elastic theory (i.e. $K_f = K_t$). The $K_f$ parameter, which is determined experimentally, is not a true constant and has been shown to vary with notch type and severity, material and stress level *(Suresh 2003, p.242-243)* and *(Evans 2003, p.19, 21-22)*

### 2.4.2 Local Strain-based Approach for Notches

The local strain based approach relates deformation in the immediate vicinity of a stress concentration to the remote stresses and the determination of the fatigue life expected for the local stress and strains. This requires knowledge of the local stress and strain histories at the tip of the notch, which can be determined through several techniques, the most effective being full elastic-plastic finite element simulations. This method however, is both expensive and time consuming. As a result, pseudo-analytical methods are commonly used, being cheaper and quicker than finite element analysis, but less accurate. One such method is the Neuber analysis.

### 2.4.3 Neuber Analysis

When elastic deformation occurs at the notch tip the stress and strain concentration factors, $K_\sigma$ and $K_\varepsilon$ are of equal value. Under conditions of plastic

deformation however, the theoretical elastic stress concentration factor, $K_t$, is given by the geometrical mean of the stress and strain concentration factors, as stated in Neuber's rule *(Neuber 1961, p.544-550)*:

$$K_t = \sqrt{K_\sigma K_\varepsilon} \qquad (2.11)$$

The stress redistribution at the notch root due to plastic deformation can then be estimated from this relationship. Maximum stress (and strain) if the material were to remain elastic is calculated using the $K_t$ factor. Plastic flow means this stress is never achieved. Throughout the resultant redistribution the stress and strain at the notch remains constant. Thus, the equivalent plastic stress and strain can be calculated *(Evans 2003, p.31)*.

The prediction of fatigue lives for notched members involves using a modification of Neuber's rule whereby the $K_t$ factor is substituted with $K_f$, giving:

$$K_f = \sqrt{K_\sigma K_\varepsilon} \qquad (2.12)$$

(*Suresh 2003, p.262-265*) and (*Evans 2003, p.30-32*).

## 2.5 HIGH TEMPERATURE FATIGUE

### 2.5.1 Damage Mechanisms at Elevated Temperatures

Fatigue crack nucleation in an alloy at elevated temperatures is influenced by the following mechanisms:

(i) Cracking, induced by cyclic slip

(ii) Grain boundary cavitation

(iii) Grain boundary sliding and the development of wedge cracks

(iv) Nucleation and growth of voids at inclusions and precipitates

(v) Oxidation and corrosion.

### 2.5.2 Cyclic Slip

Cyclic slip is affected by temperature in the following ways. The majority of materials exhibit wavy slip characteristics at temperatures greater than one-half the homologous temperature, while solid solution alloys show an increase in stacking fault energy with increasing temperature Remy, Pineau & Thomas, 1978. (*Remy et al 1978)*. Increase in temperature also allows for dislocation climb and cross slip. At elevated temperatures the kinematic irreversibility of cyclic slip is enhanced by oxidation and / gas diffusion. In some materials the tendency for wavy slip can be inhibited by dynamic strain ageing, which favours slip planarity. Dislocation climb, being time-dependent, makes deformation at elevated temperature strain rate sensitive. At elevated temperatures, the stability of many engineering alloys breaks down, modifying the stress-strain characteristics.

### 2.5.3 Creep Cavitation

At low stresses and temperatures of $0.3\text{-}0.6T_m$ most alloys exhibit creep deformation by grain boundary cavitation. Cavities nucleate at grain boundary triple point junctions, grain boundary particles, ledges on intergranular facets and shear

sliding of grain boundary facets. Creep cavity nucleation occurs well below a nominal stress level of 100MPa, and continues over a large part of the fatigue life (*Riedel, 1987*). Creep cavitation is strongly influenced by the stress waveform, with long hold times in tension resulting in a greater likelihood of cavitation that balanced load cycles (*Majumdar & Maiya, 1980*) and (*Baik & Raj, 1982*).

### 2.5.4. Oxidation

An oxidizing environment can influence the mechanisms of high temperature fatigue crack initiation in the following ways. An oxidizing environment may prevent the closure of cavities at elevated temperatures. Without the protection of an oxide layer, a grain boundary near a free surface may be susceptible to oxygen or embrittling species diffusing along the boundary to react with grain boundary precipitates. Fatigue cracks may nucleate due to enhanced kinematic irreversibility of cyclic slip, caused by a combination of surface diffusion and slip step oxidation. Microscopic stress concentrations may develop due to preferential oxidation at microstructural sites, such as the intersection of a grain boundary with a free surface.

The stress concentrations elevate local stresses, promoting crack nucleation (*Duquette, 1979*). Protective oxide film on a materials surface may be ruptured by repeat fatigue loads, providing a path for chemical attack. Cracking of the film itself, may also lead to the growth of a fatigue flaw (*Wells, 1979*).

### 2.5.5 Environmental Effects on Fatigue

The fraction of fatigue life at which crack nucleation occurs can be significantly affected by the test environment. It was demonstrated by Gough & Sopwith that fatigue life is greatly improved in vacuum, or in dry, oxygen-free environment, compared to moist laboratory air *(Gough & Sopwith 1932)*.

Meyn first showed that striation formation may be completely suppressed in vacuum in aluminium alloys, which form well defined striations in moist air *(Meyn 1968)*. Pelloux reported similar findings for the titanium alloy Ti-6Al-4V in a vacuum of $5x10^{-6}$ torr and suggested that the alternating shear process is reversible provided an oxide film isn't formed on the slip steps created at the crack tip *(Pelloux 1969) and (Pelloux 1970)*. Under load reversal the oxide layer obstructs slip so Pelloux suggested that this would result in a larger net fatigue crack growth increment per cycle in air that in vacuum (*Suresh 2003, p.340-341*).

## 2.6 TITANIUM ALLOYS

Titanium became available in commercial quantities following the Second World War. It is relatively expensive compared with other common metals, but may be the most cost effective in certain applications due to attractive properties. Thus, at the beginning of the 1960's, titanium alloys came into widespread use in aircraft engines, with over 90% of titanium production allocated to aircraft applications. (*Donachie 1982, p.3*). Titanium has two main advantages over other metals, the first being a high strength/weight ratio and the second being good corrosion resistance. This has made it particularly suitable for aerospace applications (*Collings 1984*).

Titanium has a density of 4.5Mg/m$^3$ and has excellent aqueous corrosion resistance, a characteristic conferred on its alloys. Titanium is resistant to oxidation up to 593°C, but is a reactive metal that can dissolve, interstitially, the elements oxygen, nitrogen and hydrogen. This, combined with the allotropic transformation from the lower temperature hexagonal close-packed (HCP) form to the higher temperature body-centred cubic (BCC) at 882°C limits its application temperature, which generally sits at 600°C. The transformation temperature is a function of alloy content. Alpha stabilisers promote higher transformation temperatures, while beta stabilisers promote lower temperatures *(Donachie, 1982, p.4)*.

### 2.6.1 Titanium Alloy Systems

Titanium alloys divide into three classes: alpha, alpha-beta and beta alloys. Alpha alloys are higher in strength then unalloyed titanium and are generally quite ductile. Alpha-beta alloys contain both alpha and beta stabilisers. Beta alloys have a higher density than alpha-beta alloys due to their high alloy content, reducing their strength density values *(Donachie 1982, p.4)*.

Alpha–beta alloys have higher strength than alpha alloys and account for more than 70% of all titanium used. They range from highly β stabilised and deep hardening alloys such as Ti 6246 and Ti 662 (which provide high strength at intermediate temperatures), to lean α–β compositions such as Ti 6-4, where a comparatively high aluminium content gives excellent strength and elevated temperature properties *(Donachie, 1982, p.3)*.

Ti-6Al-2Sn-4Zr-6Mo (Near-β, α+β alloy)is an α+β alloy formed from Ti 6242 by increasing the Mo content to improve age-hardenability (*Collings 1984, p.68*). It is a highly β-stabilised, deep hardening α+β alloy, which has high strength at room and intermediate temperatures. These properties lead to its use in gas turbine compressor parts *(Donachie 1974, p.61-70).*

### 2.6.2 Mechanical Properties and Microstructure

The mechanical behaviour of Ti alloys is strongly dependent on microstructure, which itself depends on processing history. An unusual aspect of Ti alloy metallurgy is the ability to control the microstructure on two different scales virtually independently. Features between 10 and 250μm affect the fatigue and fracture behaviour and are affected by processing. Sub-micron features control strength and are affected by heat treatment *(Flower 1995, p.104-105).*

The properties of titanium alloys not only depend on alloy composition, but also on microstructure, with microstructural morphology depending on the final stages of fabrication and heat treatment. The majority of α–β alloys contain substantial amounts of β-isomorphous elements (such as molybdenum and vanadium), which depress the transformation temperature and stabilize the β phase to lower temperatures.

The mechanical properties required of an alloy may be controlled through the careful selection of an annealing temperature. Low annealing temperatures result in higher strengths due to a fine grain size, while increasing the annealing temperature to just below the β transus results in a decrease in ultimate and yield strengths. High

temperature annealing does result in improved toughness however, and also improves creep strength and fracture toughness through the development of an acicular α structure (transformed β) (*Seagle, 1968).*

Ti 6246 microstructure is formed by following the solution treatment ageing and solution treatment over-aging heat treatments with air cooling, unlike Ti 6-4 and Ti 662. This air cool results in a Widmanstatten α+β in which the β phase is still metastable. Further aging results in precipitation of fine a phase in this β resulting in strengthening due to the fine microstructure, when compared to the coarse microstructures of Ti 6-4 and Ti 662.

This results in Ti 6246 generally having a higher strength than Ti 6-4 and Ti 662. Ti 6246 also displays a correlation between work hardening rate and toughness, though the alloy has a lower toughness overall, when compared with the other two alloys. These differences in properties result different fatigue fracture modes. Ti 6-4 has been shown to fracture through a complex combination of tearing and hole formation growth, while Ti 6246 fractures along prior β grain boundaries.

Titanium alloys are known to creep at room temperature at stresses below the macroscopic yield stress. Neeraj et al (*Neeraj 2005*) have shown that the two-phase α/β alloy, Ti-6242, and single phase binary alloy, Ti-6Al, exhibit a dramatic asymmetry between tension and compression during room temperature creep, with Ti-6242, accumulating about five to six times higher creep strains in tension than in compression. The single phase alloy also exhibits tension-compression asymmetry in creep, although it was observed to be less pronounced compared to the two phase

alloy. The core structure of basal dislocations is altered by the addition of alloying elements, especially oxygen, and that the tension-compression asymmetry is primarily due to the behaviour of these dislocations.

### 2.6.2.1 Fatigue properties of α+β alloys

Fatigue behaviour can be separated into fatigue life and fatigue crack growth rate (FCGR), which itself can be divided into short and long crack behaviour. The fatigue behaviour of Ti alloys is intermediate between high strength steel and high strength Al alloys when compared on a density normalized basis. For α+β alloys there is scope for tailoring the balance between fatigue life and fatigue crack growth behaviour, due to the wide range of microstructural, thermo-mechanical processing and heat treatment options.

Microstructure affects the fatigue life of Ti alloys in two ways. It affects strength and crack initiation behaviour. With α+β alloys the concentration of Al controls whether slip in the α–phase is planar or wavy, with planar slip occurring in localised bands in alloys with Al contents ≥ 5wt%. Higher oxygen contents also cause planar slip to intensify and become localized. Planar slip is a major factor in the fatigue behavior of the alloy along with slip band length. α+β alloys with colony microstructures have the lowest fatigue strength of any microstructural condition because this exhibits a tendency to form long, planar slip bands. Here, the stress to initiate plastic deformation is low, with the onset of plastic deformation concentrated in the planar slip bands, resulting in early crack initiation. Evidence regarding the effect of oxygen on fatigue strength is contradictory because oxygen promotes planar,

localised slip, but also increases yield strength. This is an area that has not been studied systematically.

Microstructures that contain high volume fractions of fine, acicular structure (solution treat and age or β quench) have the best high cycle fatigue (HCF) properties. Microstructures that exhibit greater tensile ductility and good fatigue behaviour (solution treat and age) tend to have slightly better low cycle fatigue (LCF) properties, as predicted by the Coffin-Manson Law. Blocky α or grain boundary α have the greatest effect on fatigue crack initiation behaviour in the higher cycling stress or strain ranges. It is therefore the most detrimental to LCF behaviour and must be carefully monitored in applications where LCF is the limiting factor. These features also result in increased scatter in LCF life in laboratory testing, affecting minimum life LCF curves in design databases *(Flower 1995, p.113-115)*.

Lutjering (*Lutjering 1998*) has shown how decreases in alpha colony size in α+β titanium alloys significantly enhance yield strength, ductility, fatigue crack initiation response and resistance to small fatigue crack growth, while a large colony size improves long crack behaviour, enhances fracture toughness and improves creep resistance.

At temperatures higher than 540°C in oxidising atmospheres inward diffusion of oxygen can result in the formation of an all alpha surface layer called the alpha case, the depth of which increases with increasing exposure time and temperature (*Sung et al 2005)*. This alpha layer is brittle, lending itself to crack initiation and propagation, which seriously degrades the mechanical properties of the bulk material,

with high-cycle fatigue properties suffering considerably. Titanium α case has been known to fail in fatigue at less than half of the life of titanium without α case. The alpha case is developed by the interstitials such as carbon, nitrogen and oxygen diffusing into the titanium material (*Pitt et al 2007*).

### 2.6.3 Crack Growth Behaviour of α+β Alloys

The early stages of fatigue crack growth in α+β titanium alloys, is associated with the development of facetted regions on the fracture surface. These facets form as the crack front addresses the local microstructure, usually having a basal plane orientation and are described as quasi-cleavage facets *(Evans, Bache McElhone, Grabowski, 1997)*. They have been attributed to the separation of intense slip bands under the action of a tensile stress normal to the band.

Ti alloys exhibit a substantial microstructural dependence of fatigue crack growth rate (FCGR) behaviour, and is most pronounced in α+β alloys at yield strengths in excess of 1200MPa. This is due to the ability to vary micron sized microstructural features virtually independently of strength.

Microstructural dependence of FCGR in α+β alloys is strongest in the near threshold range of crack growth rates ($da/dN \leq 5x10^{-5}$mm/cycle). Some dependence is also noted in the Paris regime ($5x10^{-5}$ to $1x10^{-3}$ is Ti-6-4) where $da/dN$ is proportional to $\Delta K^n$ (where the exponent is typically 4-6 for Ti alloys). Above this range the divergence of the $da/dN$ vs. $\Delta K$ indicated the microstructural dependence of $K_{IC}$. *(Flower 1995 p.118)*.

### 2.6.4 Environmental Effects on Crack Growth at Elevated Temperatures

Oxide formation in the crack tip region can lead to closure effects. This is not a major factor at room temperature, where the rate of oxide formation is low. At temperatures of 500°C and greater oxygen forms on the fracture surface in the crack tip region. Oxygen also affects the intrinsic crack growth resistance and it is difficult to separate these two factors. Crack growth tests conducted in air at 520°C by Allison showed artificially high $\Delta K_{th}$ values during decreasing $\Delta K$ (load shedding) tests, suggesting oxide-induced closure *(Allison 1982)*. At higher R-values oxygen penetration should be more pronounced, due to the crack tip remaining open. This is extremely important to high temperature, creep resistant alloys, such as Ti-6-2-4-6.

The greatest effect of environment occurs at $\Delta K$ values that have corresponding $K_{max}$ values just above the threshold for sustained load cracking. Therefore at very low $\Delta K$ values, no effect is observed because the material is immune to the environment. Crack growth rate at high $\Delta K$ levels can be dramatically altered at low frequencies, or if there is a dwell period at the maximum load.

Lesterlin et al *(Lesterlin 1996)* showed that Ti6246 undergoes a significant increase in crack propagation rate from 465°C to 500°C, which these authors attributed to environmental effects. The nature of the active species responsible for fatigue damage at high temperatures has yet to be determined, with two competing theories at present. Petit et al *(Petit, Mendez, Berata Legendre and Muller, 1992)* have attributed the detrimental influence of environment to the embrittling effect of water vapour while other authors have suggested oxygen diffusion *(Ghonem & Foerch 1991) and (Foerch, Madsen and Ghonem 1993).*

More recent work by Sarrazin-Baudoux (*Sarrazin-Baudoux, 2005*) involved crack propagation tests in the near threshold and mid-rate ranges under controlled gaseous environments and water vapour and oxygen pressures. This research has shown a predominant detrimental effect of water vapour, even under very low partial pressure, while showing that gaseous oxygen moderates the influence of water vapour with a competitive adsorption mechanism between $O_2$ and $H_2O$ being proposed.

Work by Demulsant et al (*Demulsant, Mendez 1996*) has suggested that a normal air environment plays an active role in initiation and short crack propagation of titanium alloys. It was also shown that vacuum test conditions results in a drastic reduction in surface crack densities. Evans et al (*Evans 2005)* showed that an increase in R ratio resulted in an increase in crack growth rates, indicating mean stress dependence, a behaviour typical of environmentally assisted crack growth. Lesterlin et al's (*Lesterlin, 1996*) comparison of closure corrected data in air and vacuum at 300°C and 500°C showed a substantial influence of atmospheric environment at 500°C. It was also shown that a lowering of the test frequency induces enhanced crack growth rates at these temperatures, with the effect being accentuated at 500°C. Further research on environmentally assisted fatigue crack growth, has recently been conducted by Henaff et al (*Henaff, 2007*). This work has added to the body of evidence supporting the water vapour adsorption and subsequent hydrogen embrittlement model.

### 2.6.5 Notch Response of α+β Ti Alloy

Bache et al have shown that the microstructural condition strongly influences the form of the cyclic stress-strain curve and the corresponding hardening or softening characteristics of the alloy *(Bache, 1999)*.

Bache et al showed that the $K_t\Delta\sigma$ parameter is a sensitive means of assessing the interaction between microstructure and notch geometry, though deviations from the general trend were did occur *(Bache 1999)*. These deviations were the result of critically stressed volumes of material at the notch root, which are determined by fatigue sensitive weak links (microstructural features), the cyclic yield strength, the shape of the stress-strain curve and the materials hardening or softening characteristics.

Work by Evans *(Evans 1999) (Evans, Bache & Nicholas 2001)* also showed the effectiveness of the $K_t\Delta\sigma$ parameter in correlating notch fatigue behaviour. It was also indicated that high $K_t$ notches tend to have a better fatigue performance that this correlation would suggest, as a result of their smaller plastic zone reducing the probability of critically stressed volumes within this area.

# *LITERATURE*

# *REVIEW*

# *APPENDIX*

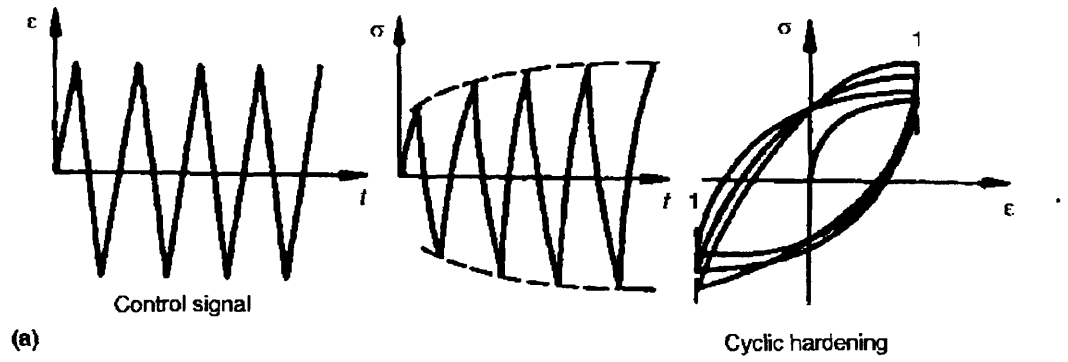


**Figure 2.1: Schematic representation of cyclic hardening**

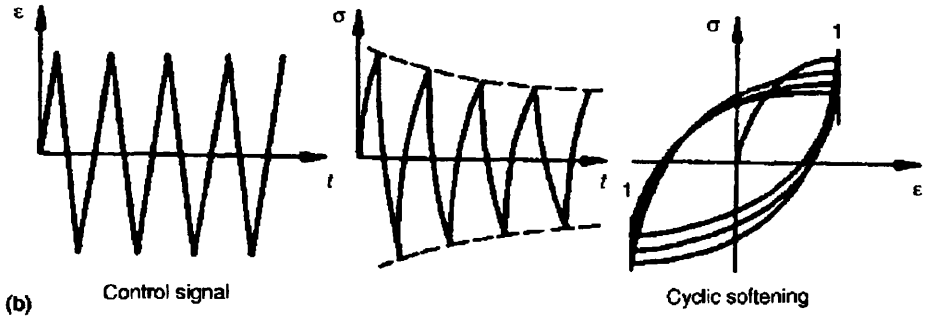


**Figure 2.2: Schematic representation of cyclic softening**

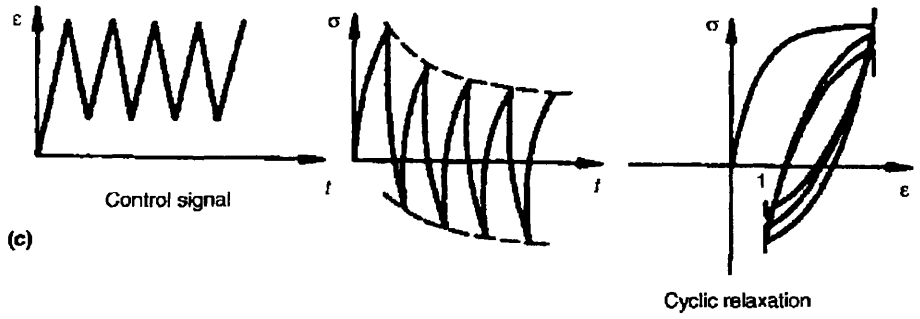


**Figure 2.3: Schematic representation of cyclic relaxation**

## 3.0 PROGRAMME AIMS

The literature review focused on the low cycle fatigue response of the $\alpha+\beta$ titanium alloy Ti 6246 at elevated temperatures, where significant interactions between creep and environment occur. Particular emphasis was placed on the response of these materials, in relation to the presence of stress concentrations, where creep deformation can modify the stress and strain conditions at the notch root and localised oxidation can affect initiation and crack propagation. This investigation has shown that the following areas require further research:

- Notch fatigue behaviour at temperatures where interactions from creep and environment are significant.
- The limitations of life prediction methods at low temperatures are conservative, but is this conservatism valid at high temperatures, where creep and environment failure modes interact with fatigue failure modes?
- What impact do interactions from creep have on crack growth rates?
- The effect of environment on crack growth rates.
- The effect of creep and environment interactions on design curves based on peak elastic stresses ($K_t\sigma$).
- The individual contributions of fatigue creep and environment to fatigue life at elevated temperatures.
- Effect of fatigue / creep / environment interactions on crack initiation.
- Effect of fatigue / creep / environment interactions on material deformation.

In order to explore these issues, a programme involving the following tests was conducted at ambient and elevated temperatures:

- Low cycle fatigue cyclic strain control tests
- Low cycle fatigue strain control tests with dwell periods at peak strains.
- Load control tests of double edged notch (DEN) specimens in air and hard vacuum, under cyclic and dwell conditions.
- Cyclic load control tests of V cylindrical notch (VCN) specimens.
- Fatigue crack propagation tests on plain specimens using cyclic and dwell waveforms.
- Crack initiation recording of DEN specimens under fatigue conditions.
- Fatigue crack propagation tests on DEN specimens using cyclic and dwell waveforms.

## 4.0 EXPERIMENTAL PROCEDURES

### 4.1 Ti6246 Microstructure

The material was tested in the as-received condition, following thermo-mechanical processing and heat treatments. This resulted in a Widmanstatten microstructure expected from a titanium alloy processed above the beta transus temperature, shown in Figure 4.1a and 4.1b, where $\alpha$ grains and acicular $\alpha$, in the coarse prior $\beta$ matrix, which itself consists of grain boundary $\alpha$, are clearly visible. None of the samples were shot peened.

### 4.2 Strain Control Fatigue Testing

Strain control fatigue tests were carried out according to an in house procedure based on BS7270:1990 *(BS 7270 1990)* using an ESH servo-hydraulic test machine with a load range of 50kN, an extension range of 0.2mm and a position range of 10mm.

Waveforms were generated using an external PC, which recorded stress – strain data periodically throughout the test to provide hysteresis loops and peak stress data. Testing was conducted using strain control specimens with a diameter of ~6mm, verified by micrometer according to directives set in the IRC test manual. These specimens were manufactured to an in-house specification shown in Figure 4.2. A UKAS calibrated air-cooled MTS extensometer (gauge length of 12mm) with 85mm ceramic arms controlled the test. Elevated temperature testing was performed in a radiant split furnace and temperature was monitored using calibrated n-type thermocouples.

Strain control testing was performed using an R ratio of 0, 0.5 and –1. A trapezoidal waveform was used during testing; with all strain-controlled tests performed at a constant strain rate ($\delta\varepsilon/\delta t$ = 0.5%/sec) with a 1 second hold at maximum and minimum strains. The waveforms corresponding to these criteria are shown in Figure 4.3 (R = -1), Figure 4.4 (R = 0) and Figure 4.5 (R = 0.5). Dwell tests were performed at the same strain rate with a 120 second hold at maximum strains for unbalanced dwell tests and 120 seconds at maximum and minimum strains for balanced dwell tests. The waveforms of these dwell tests are shown in Figure 4.6.

Specimen life was defined as when the peak load had dropped 10% from the stress. For this programme $10^5$ (100,000) cycles was defined as an LCF "run-out" indicated by a horizontal arrow in graphs.

### 4.3 Load Control Testing

Load control fatigue testing was performed to generate fatigue life data for specimens. Testing was conducted using Double-edged notch (DEN) specimens with a calculated $K_t$ factor of 1.92, a through thickness of 10mm and a distance of 10mm between the notches, as shown in Figure 4.7.

Tests were performed either on a Mayes Servohydraulic test machine with a load range of 100kN or on an ESH Servohydraulic machine with a load range of 50kN, depending on availability, and were completed in accordance with BS3518. Load ranges were selected to be 20, 50 or 100kN, dependent on the peak load applied to the specimen. A fatigue (or endurance) limit of $10^5$ cycles was employed in these tests, at which point the test was stopped. These 'run-out' tests are indicated

by horizontal arrows in the results plots. Vacuum testing was conducted under a hard vacuum of $10^{-6}$ Torr.

### 4.4 Initiation & Crack propagation Testing

Crack propagation testing was conducted using Double-edged notch (DEN) specimens with a calculated $K_t$ factor of 1.92, a through thickness of 10mm and a distance of 10mm between the notches (Figure 4.7), a 10mm x 10mm corner crack specimens (CC10) with a 0.35mm notch machined into one corner (Figure 4.8) and corner crack double-edged notched (DEN) specimens with a calculated $K_t$ factor of 1.92, a through thickness of 10mm and a distance of 10mm between the notches.

Testing was performed on a Mayes Servo-hydraulic machine with a load range of 100kN with loads measured to an accuracy of 0.01kN. A waveform was generated by a PC, which controlled the testing apparatus and periodically took crack growth measurements. Peak and minimum load remained constant throughout the tests with the growth of the crack causing a gradual increase in $\Delta K$ at the crack tip. Initiation tests were conducted at R= 0 at temperatures of 500°C and 550°C. Crack propagation tests were undertaken using a R ratio of 0.1 using a 1-300-1-1 trapezoidal (5 minute dwell) waveform on CC10 specimens, while corner crack DEN specimen tests were conducted at R= 0.05, 0.1 and 0.7. Testing was completed at 20°C, 500°C and 550°C.

Crack propagation testing involved the use of the Direct Current Potential Drop (DCPD) method to record data, which were conducted in accordance with the Rolls Royce procedure MMM 31002. The technique involved periodically (to avoid

heating the specimen) passing a current of 30 amps through a test piece and measuring the electrical potential across the crack plane, with the P.D. being measured using commercially pure platinum (99.99% platinum) wires of 0.05mm thickness. The placements of the wires for DEN initiation, DEN corner crack propagation, DEN centre-hole crack propagation and plain specimen crack propagation are show in Figures 4.9, 4.10, 4.11 and 4.12 respectively.

As the crack propagated a higher voltage was required to drive the current through the specimen due to the decrease in cross sectional area. However, the method requires accurate calibration, which involved taking surface replicas of cracks following initiation testing, by using acetone and polycarbonate at 75% of the peak load. From the replica, a final crack size was measured, using a travelling stage microscope, to an accuracy of 0.005mm. The sample was then tinted by heating in air and cycled to failure at room temperature so that crack length measurements could be verified. This method allowed for the detection of the initiation of a crack in a specimen as early as possible.

### 4.5 Specimen Analysis - Microscopy and Fractography

Fractured test pieces required no preparation prior to microscopy. However, crack propagation tests were halted before fracture and the following procedures were employed. Specimens were heat treated at 400°C encouraging a thin layer of oxide to form, thus colouring all exposed surfaces. Test-pieces were then subjected to fatigue at room temperature, using a positive R to propagate the existing crack to failure. Fracture surfaces were then examined using the Jeol JSM 6100 scanning electron

microscope in conjunction with the Oxford Instruments Link ISIS Software System in order to identify initiation sites, striations and other features.

Metallographic samples were mounted in a conductive Bakelite resin and prepared by grinding with increasingly fine grades of silicon carbide paper before polishing with 6μm and 1μm diamond paste. Etching of the titanium alloy Ti 6246 was performed using Krolls reagent - 2% HF, 3%$HNO_3$, 95% $H_2O$. A Reichart-Jung optical microscope was used in conjunction with a Nikon Coolpix digital camera to study the underlying microstructure of the fractures.

# *Experimental*

# *Procedures*

# *Appendix*

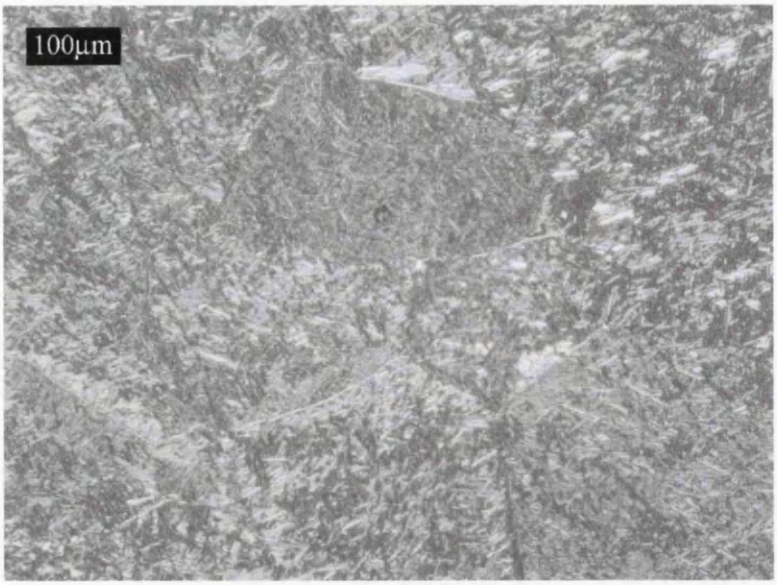


**Figure 4.1a: Optical image of Ti6246 microstructure.**

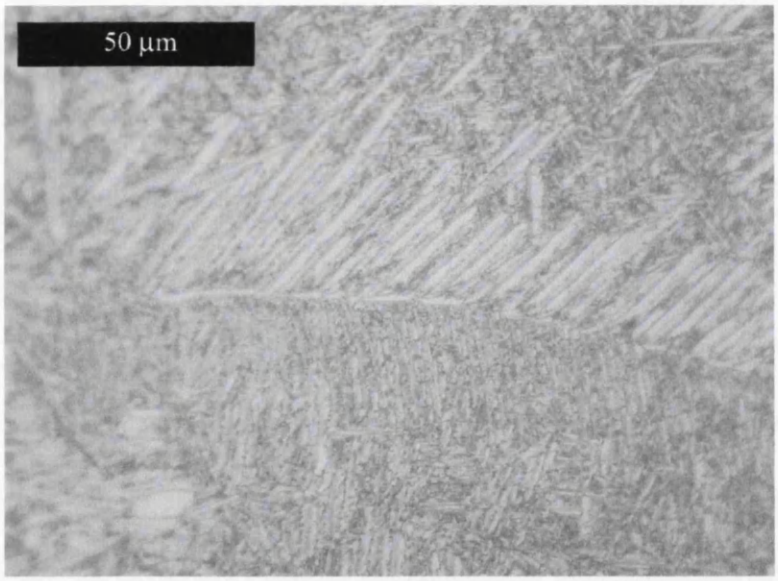


**Figure 4.1b: High magnification optical image of Ti6246 microstructure.**

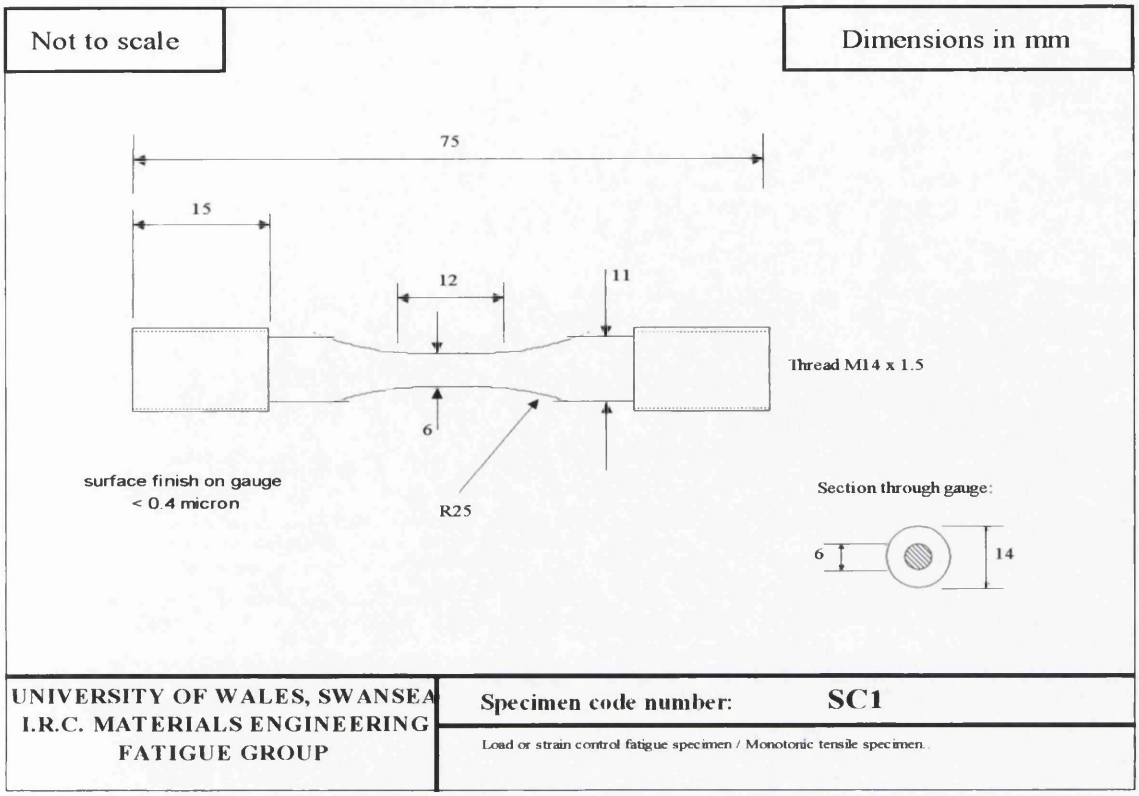


**Figure 4.2: Strain control specimen SC1 specifications.**

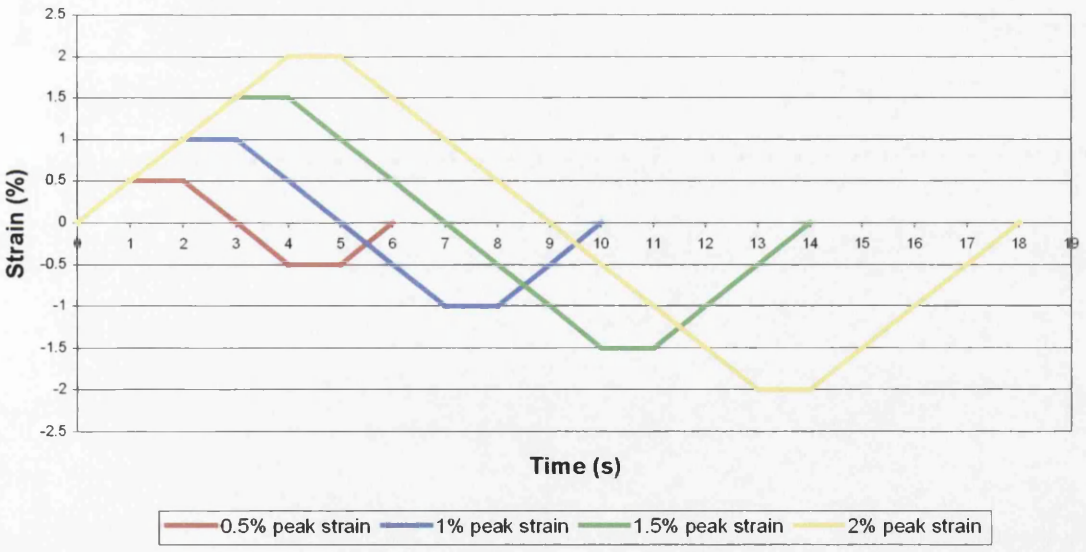


**Figure 4.3: Trapezoidal waveform for 0.5%/s strain rate (R= -1).**

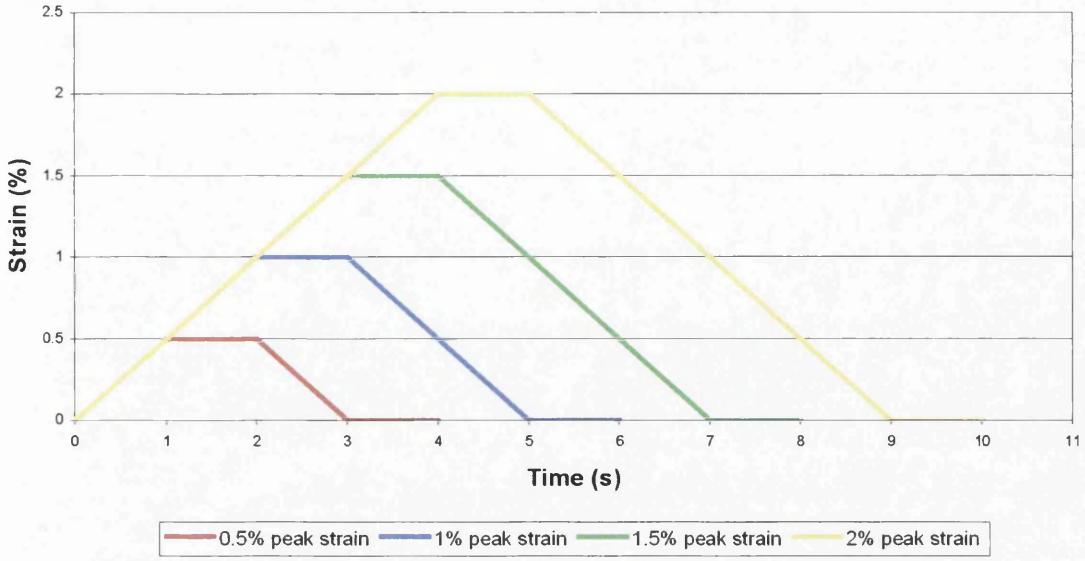


**Figure 4.4: Trapezoidal waveform for 0.5%/s strain rate (R= 0).**

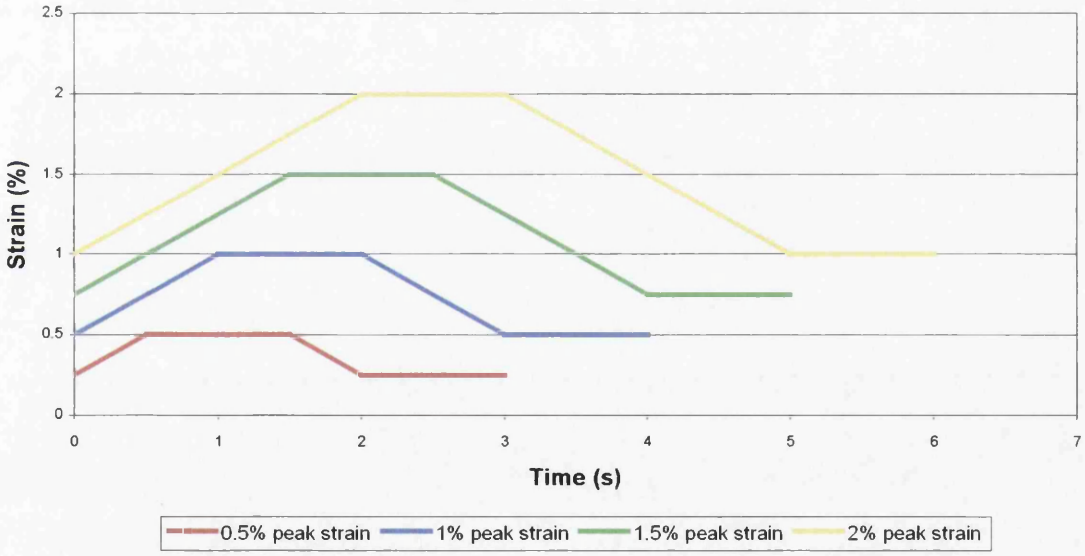


**Figure 4.5: Trapezoidal waveform for 0.5%/s strain rate (R= 0.5).**

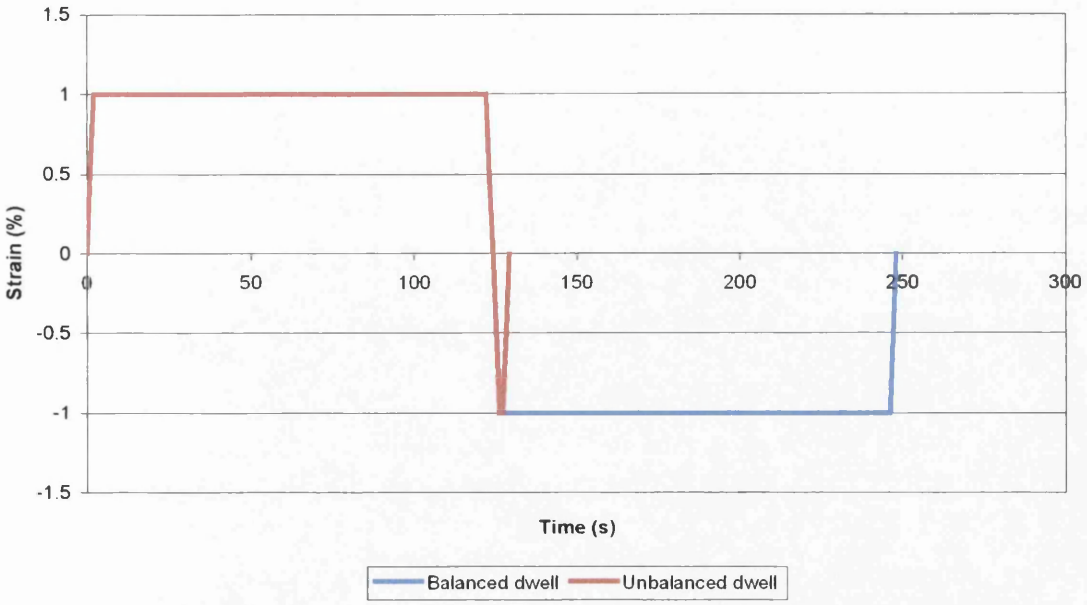


**Figure 4.6: Trapezoidal waveform, 0.5%/s strain rate, 2 minute dwell, (R= -1).**

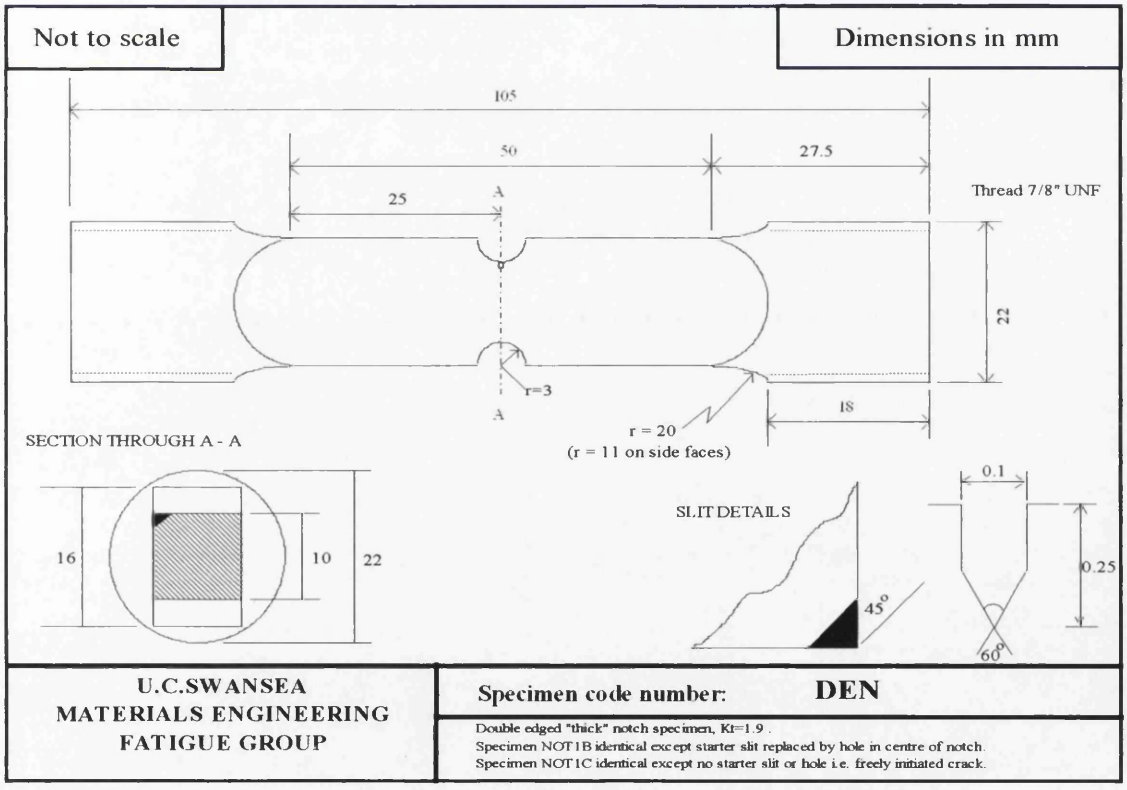


**Figure 4.7: Double edged notch specimen (DEN) specification.**

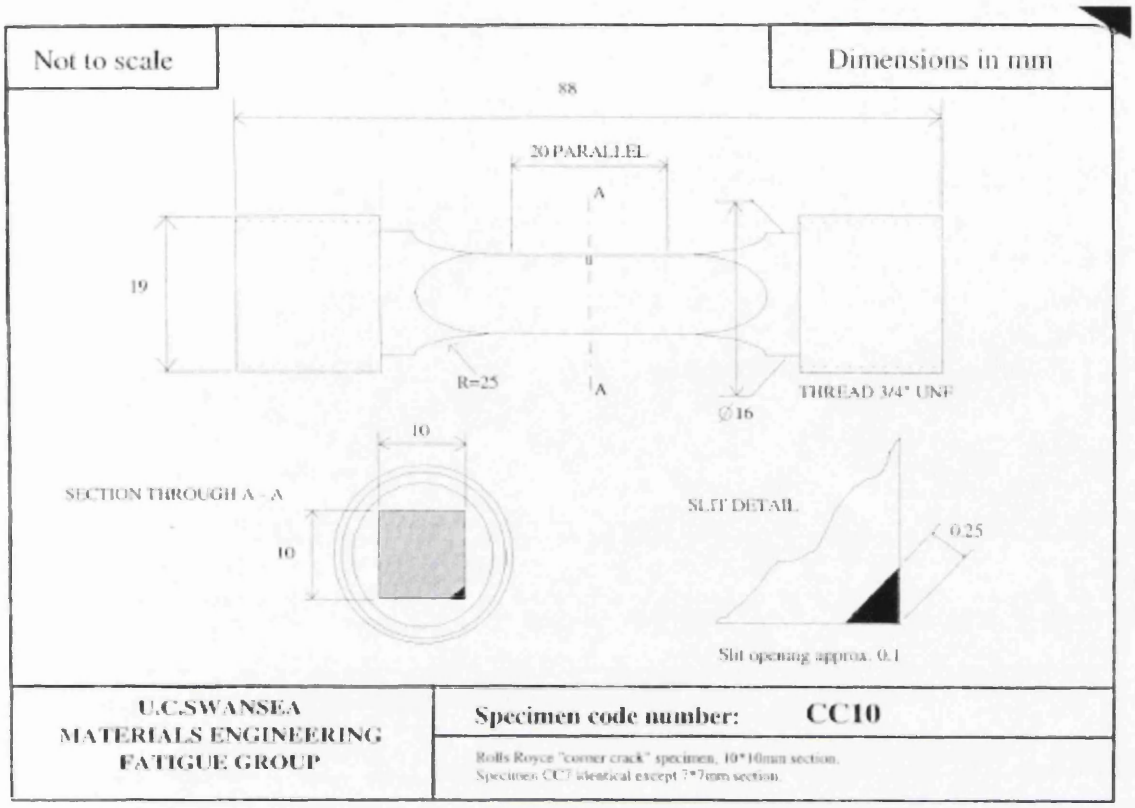


**Figure 4.8: Corner crack specimen (CC10) specification.**

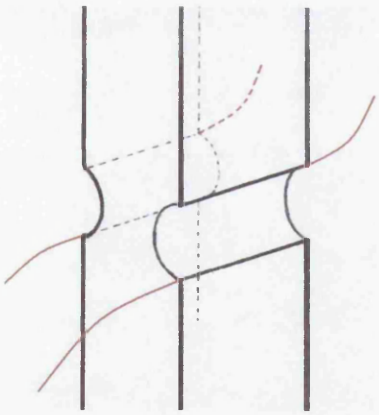

**Figure 4.9: Wire placement for DEN initiation tests**

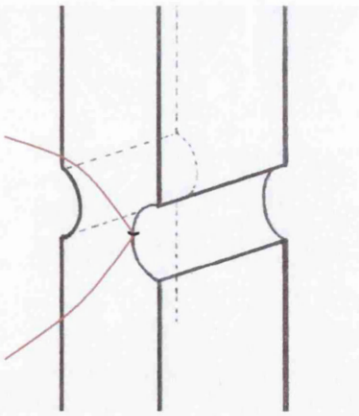

**Figure 4.10: Wire placement for DEN corner crack propagation tests.**

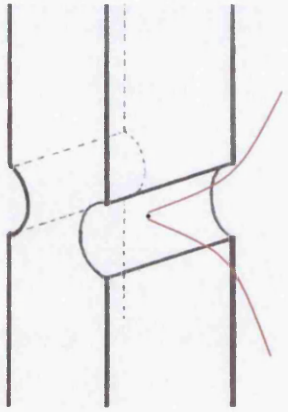

**Figure 4.11: Wire placement for DEN centre hole crack propagation tests.**

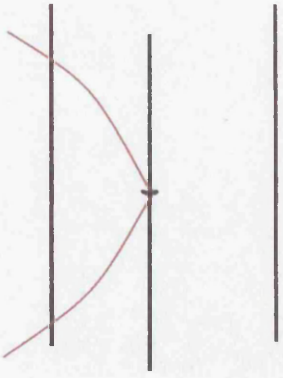

**Figure 4.12: Wire placement for plain specimen crack propagation tests.**

# 5.0 RESULTS

## 5.1 STRAIN CONTROL TESTING

Strain control testing was performed in order to provide information on the mechanical response of the alloy when tested under cyclic loading and also to characterise the alloys fatigue properties when tested at different R ratios and temperatures. This testing is relevant to the constrained regions at notch roots (*Evans, 1999).* The strain control results provided the basis for predicting crack initiation lives of the notched specimens.

### 5.1.1 Cyclic Tests

#### 5.1.1.1 20°C Testing

Cyclic testing began with a standard series of R= -1 tests at 20°C, performed at $\varepsilon_{max}$ = 0.5%, 1%, 1.5% and 2%, with an additional test performed at $\varepsilon_{max}$ = 0.7 to provide additional data for a fatigue curve (Figure 5.2). A series of R= 0 and R= 0.5 tests were also conducted at 20°C. Figure 5.1 shows a strain vs life comparison of the 20°C data, with the results displayed on a standard log-log scale. Figure 5.2 compares the monotonic and cyclic stress-strain behaviour at R= -1, with the material showing evidence of relaxation, and the cyclic yield stress being approximately 800MPa.

A sequencing test (compression first) was conducted at R= 0 at 20°C, with a peak strain of 1% to compare the material response with a tension first test, resulting in the data shown in Figure 5.3. This shows that in compression, the material has a

higher modulus (assuming some yielding due to micro-plasticity, due to a low strain rate of $0.5\%s^{-1}$ and yield strength (UTS).

### 5.1.1.2 Elevated temperature testing

R= -1 strain control testing was conducted at 300, 400, 450, 500 and 550°C at peak strains of 0.5%, 1%, 1.5% and 2%. Comparisons of the monotonic and cyclic stress-strain behaviour at each temperature are presented in Figures 5.4 to 5.8. At $300^0$C the cyclic stress curve matches that of the initial curve with no indication of cyclic hardening or softening, while at $400^0$C what appears to be cyclic hardening at higher (1.5%) peak strains is observed. This trend becomes more pronounced as temperature increases to $450^0$C and $500^0$C, though the 0.5% peak strain test result may be considered anomalous. At $550^0$C creep relaxation is observed once again.

The general trend observed from the initial loops at all peak strains (Figures 5.9 to 5.12), is a decreasing modulus and yield stress as the temperature increases. This drop is most apparent between 20°C and 300°C. At 0.5% peak strain no plastic deformation is evident. At greater peak strains the substantial difference between maximum stress at $20^0$C and the high temperatures becomes more pronounced. At peak strains of 1.5% and above, widening of the loops and bowing (Bauschinger) effect in compression is observed, thus making it difficult to obtain accurate modulus values in compression. The specimen buckling in compression of the 550C test at 2% peak strain is also clearly visible.

The decrease in modulus is also apparent in the stabilised condition, shown in Figures 5.13 to 5.15, with what appears to be hardening at 450$^0$C. At peak strains of 1% and 1.5% a large amount of stress relaxation at 20°C is evident, in comparison to the higher temperatures. This corresponds to the data seen in Figure 5.2.

Figures 5.16 through 5.18 show a temperature comparison of normalized stress vs cycles plots at peak strains of 0.5%, 1% and 1.5% respectively. At a peak strain of 0.5% a constant stress throughout the tests corresponds to the elastic behaviour of the material as seen in Figures 5.9 and 5.13, while the significant decrease in stress at 20°C, in comparison to the elevated temperature tests, further indicates the stress relaxation at room temperature.

A $\sigma$-$N_f$ curve of all the R= -1 cyclic (Figure 5.19) data shows that there is a large difference between the 20°C curve and that of the high temperature data. Figure 5.20 presents a $\Delta\varepsilon$-$N_f$ plot of the same data, where at the higher strain ranges of 2 and 3% the fatigue lives across the range of tested temperatures are tightly grouped. At strain ranges below 1% temperature differences result in a wider range of lives.

#### 5.1.1.3 Dwell Tests

Dwell tests were conducted at 450, 500 and 550°C at a peak strain of 1% and R= -1, in order to investigate fatigue behaviour at temperatures where time dependent effects may have a strong influence.

A comparison of the initial stress-strain loops for trapezoidal 2 minute unbalanced dwell tests at all temperatures is shown in Figure 5.21, with a peak strain of 1% and R= -1. The effect of the 2-minute dwell can be seen at the positive peak strain end of the loop. Figure 5.22 gives a closer examination of this area in the form of a stress against time plot for the initial loop of each test at all temperatures. At 450°C the stress remains constant after an initial period of stress relaxation, while at 550°C the stress continues to fall during the 2-minute dwell period. A similar drop is seen at 500°C, though to a lesser extent than 550°C. Examinations of the stabilised loops, shown in Figure 5.23, also display a marked difference between temperatures. At 500°C and 550°C the mean stress has dropped into compression, while at 450°C the mean stress is tensile. The difference in mean stress is also clear in Figure 5.24, which shows a stress against time plot in the stabilised condition.

Balanced trapezoidal 2-minute dwell tests (trapezoidal, 1-120-1-120) were conducted at the same temperatures to see whether the creep deformation seen in the unbalanced tests was reversible. A comparison of the initial stress-strain loops of the balanced and unbalanced tests at 550°C is shown in Figure 5.25. The stress relaxation of the balanced test can be seen in both tension and compression and is shown clearly in the stress against time plot, Figure 5.26. A comparison of the stabilised loops (Figure 5.27) show a mean stress of approximately zero for the balanced dwell test, compared to a compressive mean stress for the unbalanced test. Finally, an S-N curve comparing both balanced and unbalanced dwell data with cyclic data of the same temperatures is presented in Figure 5.28.

## 5.2 LOAD CONTROL TESTING

### 5.2.1 Double Edge Notch (DEN) Fatigue Tests

DEN fatigue tests were conducted at a range of peak stresses to produce fatigue curves under air and hard vacuum ($10^{-6}$ Torr) conditions for both cyclic and dwell waveforms. In order to do this cyclic tests were conducted at temperatures of 20, 450, 500 and 550°C in air at R= 0, with some R= -1 tests at 20°C. To take account of environmental effects, cyclic-vacuum tests were performed at 450 and 550°C. Creep effects were highlighted through 2-minute dwell tests (1-1-120-1) at 500 and 550°C, while creep and environmental effects were separated by 2-minute dwell tests, run in vacuum at 550°C.

A comparison of air and vacuum tests at 450°C are presented in Figure 5.29. It can be seen that vacuum test lives are approximately an order of magnitude greater than air test lives. Dwell test were not conducted at 450°C due to minimal creep effects in Ti6246 at this temperature, as indicated in the strain control testing at this temperature, described previously.

Figure 5.30 show a comparison of dwell and cyclic data at 500 and 550°C. At these higher temperatures a significant decrease in life is apparent for the 2 minute dwell tests.

It is worth noting that although strain control tests at 550°C showed significantly more creep than 500°C tests, the decrease in life due to dwell was no greater at 550°C than at 500°C in DEN tests.

Previous figures have shown the extent of reduction in life caused by creep and environmental effects. Figure 5.32 compares cyclic and dwell tests in air and vacuum at 550°C, and shows the effect of the combined fatigue-creep-environment interaction at high temperatures. The 550°C cyclic data in vacuum can be treated as a baseline for the creep and environment effects at high temperature since the vacuum negates the environmental mechanisms and the 1 second hold time of the cyclic test is insufficient to cause significant creep damage at these stress levels. The effect of creep can be assessed by comparing the baseline with the 550°C dwell data in vacuum. The environmental effect can be determined through comparison with the 550°C cyclic data in air. From this it can be seen that environmental effects account for a greater decrease in specimen life than creep effects. A comparison of the baseline data with the 550°C dwell data in air, show the combined effects of creep and environment. From this, it can be seen that the effect is cumulative, with this set of data having the shortest life of all test conditions at 550°C.

The plot in Figure 5.33 presents a comparison of all the DEN fatigue tests during this programme. The overall trend when comparing all the data is that of a distinct transition of the fatigue curve of air tests from a steep gradient to a shallow gradient below a stress of approximately 1000MPa, corresponding to a life of $10^4$ cycles. This transition is not seen in the 20°C and vacuum data, which tends to show a more typical decrease in life with increasing stress.

Figure 5.34 compares only the cyclic data, in air, at 450, 500 and 550°C. It can be seen at elevated temperatures, that the fatigue curve up to $10^4$ cycles has a steep gradient, which then becomes extremely shallow at longer lives. It is also worth

noting that specimens tested at 500°C have longer lives than 450°C tests at a given peak elastic stress.

### 5.2.2 V Cylindrical Notch (VCN) Tests

VCN tests were conducted in order to provide additional notch response information by providing data for $K_t$ values of 2.8. This involved R = 0 cyclic testing at 20, 450, 500 and 550°C, an S-N curve of which, is presented in Figure 5.35. It can be seen that there is a significant drop in fatigue life between 20°C and 450°C, which is also reflected in the strain control data conducted during this programme. It is also worth noting that the expected drop in fatigue life from 450°C to 500°C is present, unlike in the DEN tests.

A comparison of the cyclic, R = 0 VCN and DEN data in air (Figure 5.36), show good correlation between the data (shown on a $K_t\sigma_{max}$ basis).

### 5.2.3 Initiation Tests, DEN Specimen, Air, R= 0

In order to gain crack initiation and growth data for the DEN tests, potential difference (P.D.) monitoring was employed during the air tests at 550°C under R = 0 loading conditions. Three of these tests were interrupted, with crack replicas produced and measured, to allow for a correlation to be made between voltage change and crack length. The results of this are shown in Figure 5.38. This also provided a linear fit for a range of voltages over which a crack length can be determined (Figure 5.39). This information was then used to determine crack length versus the number of cycles, as shown in Figure 5.40. The data indicates that life to a crack 2.19mm in length, as a

fraction of the total life, varied from 80% to 90% of the total life. Ultimately, this information allows da/dN vs ΔK data to be generated. All the data used, were for crack lengths that were between the smallest and largest detected cracks.

Consistent results were obtained, despite the fact that accuracy was reduced because the P.D. wires were connected across the entire notch, to allow free initiation of the cracks, as shown in Figure 5.44. From this graph a small increase in the crack growth rate from 500°C to 550°C cyclic tests can be seen, while there is a significant increase in crack growth rate at 550°C when a 2 minute dwell period is added.

Figure 5.45 shows a comparison of the freely initiated crack data with the corner cracked DEN and plane specimen corner crack tests. It can be seen that the freely initiated crack tests start with a very high $\Delta K$ compared to the crack propagation tests. This is due to the high stresses used during these tests, compared to the crack propagation tests. It appears that the freely initiated data may converge with the crack propagation data for both dwell and cyclic tests at 550°C.

## 5.3 CRACK PROPAGATION TESTS

### 5.3.1 Plane Corner Crack (CC10) Specimens

Plane specimen corner crack propagation testing during this programme concentrated on extended dwell waveforms in order to compare with previous work (*Ford 2002*) conducted in air and vacuum at 450, 500 and 550°C using 2-minute dwell and cyclic waveforms. Therefore tests were conducted at 20, 500 and 550°C with a 5 minute hold (1-1-300-1) at peak stress and R= 0.1.

Figure 5.47 compares cyclic (1-1-1-1), 2 minute (1-1-120-1) and 5 minute (1-1-300-1) dwell data at 500°C. It can be seen that the cyclic data shows the slowest crack propagation rate, with the rate increasing as the dwell period increases.

#### 5.3.1.1 CC7 Pre-deformed, 20C, R= 0

Crack growth involves propagation through a plastic region at the notch root. The effect prior fatigue damage has on growth kinetics was explored by pre-straining corner crack specimens under strain control and then monitoring subsequent growth from corner slits. Figure 5.48 demonstrates that applied strain ranges up to 1% did not affect growth characteristics.

### 5.3.2 Double Edge Notch (DEN) Crack Propagation Tests

Crack propagation of DEN specimens was undertaken using either a centre hole or a corner slit to initiate the crack. Cyclic corner crack DEN tests were conducted at 20°C and 500°C with R ratios ranging from 0.05 to 0.7, while one 500°C 2 minute dwell test was performed at R = 0.1. Centre hole tests were performed at 450 and 500°C with a R ratio of 0.1. Again, this data was generated to complement previously generated data (*Ford 2002*).

Figure 5.49 compares centre hole and corner crack DEN tests with an R ratio of 0.1 at 500°C. From this it can be seen that the growth rates correlate. A comparison of plane and DEN corner crack specimens at 550°C presented in Figure 5.50 shows good correlation between DEN and plane specimen test. At lower $\Delta K$ values however,

it can be seen that the data begins to diverge. In order to determine whether this divergence was the result of creep effects at this temperature, or a miscalculation of the DEN specimen K values, a similar test was conducted at 20°C with the results shown in Figure 5.51. It can be seen that there is no discrepancy between this data, indicating that it is unlikely to be a K value miscalculation. What is also clear in Figure 5.50, is the increase in crack propagation rate as R ratio increases.

A plot of the cyclic, R= 0.1 and 2 minute dwell, R= 0.1 (both at 500°C) compared with previous DEN specimen data (Evans, Jones & Bache) is shown in Figure 5.52. The previous data is taken from tests of centre hole DEN specimens of 3mm diameter, compared to the 10mm diameter specimens of this programme. The cyclic test shows good correlation with the previous data, although the 2 minute dwell data has a large amount of scatter, the effect of the dwell period is clear with an increased crack growth rate at a given $\Delta K$ compared to the cyclic data at 500°C.

A comparison of centre hole and corner crack DEN crack propagation data at 450, 500 and 550°C is presented in Figure 5.53. This shows an increase in the crack propagation rate as temperature increases, emphasising the increased role of creep and environmental damage. The R= 0.7 test at 550C indicates that the damage accumulation is enhanced by mean stress, promoting either faster creep rates or accelerated environmental cracking.

## 5.4 PREDICTION OF NOTCHED SPECIMEN BEHAVIOUR

### 5.4.1 The Coffin-Manson Method

The Coffin-Manson method *(Coffin 1973), (Manson 1965)* involves separating R= -1 strain control data into elastic and plastic components, shown in the equation *5.1*:

$$\Delta\varepsilon_{Tot} = C_e N_f^{\alpha 2} + C_p N_f^{\alpha 1} \qquad (5.1)$$

At room temperature:

$C_e = 0.0361$

$C_p = 1.0301$

$\alpha 1 = -0.792$

$\alpha 2 = -0.1233$

In order to calculate the strain at the notch root, the Neuber *(Neuber 1961)* appoximation was employed, which involves the redistribution of a hypothetical elastic line, in order to calculate the conditions in the plastic zone at the notch root. This is defined through the following relationship:

Stress ($\sigma$) x strain ($\varepsilon$) = constant *(5.2)*

Figure 5.54 shows the redistribution process represented by the hyperbolic curve AB. Where this curve intercepts the stabilised cyclic stress-strain curve, the stabilised condition in defined. By assuming elastic deformation of the material the

line BC is added, which is extended to the applied stress, giving minimum stress and strain values. This elastic unloading response was used after examining R= 0 and R= -1 FEM data. The strain data determined for the notch root was then inputted into the Coffin-Manson equation, allowing notch life prediction to be performed.

The notch life predictions using the Coffin-Manson method are shown in Figure 5.55, where it provides a good prediction for DEN R= -1 data, but overestimates the R= 0 DEN data. It must be noted that these observations do not take into account the results of the potential difference monitoring of freely initiated notch tests. These showed that 80 to 90% of DEN fatigue life was spent growing a fatigue crack to 2.19mm, leaving 10-20% of total fatigue life for crack propagation. By comparison, cracks in strain control tests, once initiated, propagate quickly to failure.

Notch life predictions were also done for the VCN data and resulted in good predictions of experimental data shown in Figure 5.55.

### 5.4.2 The Walker Strain Method

The Walker strain method involves quantifying mean stress effects through the correlation of different R value data (*Walker 1970*), by using equation *5.3*:

$$\Delta\varepsilon_W = \frac{\sigma_{max}}{E}\left(\frac{\Delta\varepsilon E}{\sigma_{max}}\right)^m \qquad (5.3)$$

where; $\Delta\varepsilon_w$ = Walker strain

$\sigma_{max}$ = maximum stabilised stress

$E$ = modulus

$\Delta\varepsilon$ = strain range

m = Walker exponent

Altering the Walker exponent through a process of curve fitting, until the strain control data of different R values correlated, resulted in m = 0.45 at 20°C. Fitting a curve to this correlated data resulted in the following equation:

$$\Delta\varepsilon_w = 0.0346 N_f^{-0.1525} \qquad (5.4)$$

The conditions at the notch root were calculated using the Neuber method, described previously, with the strain range and maximum stabilised stress values being used to calculate a Walker strain for the notched specimen. This allows notched specimen lives to be predicted. For R= -1 data the Walker method provided an accurate prediction, while there is a slight over-prediction for R= 0 notches. At 450°C the Walker strain method provided a reasonable prediction of R= 0 notched specimen lives, shown in Figure 5.56.

# *RESULTS*

# *APPENDIX*

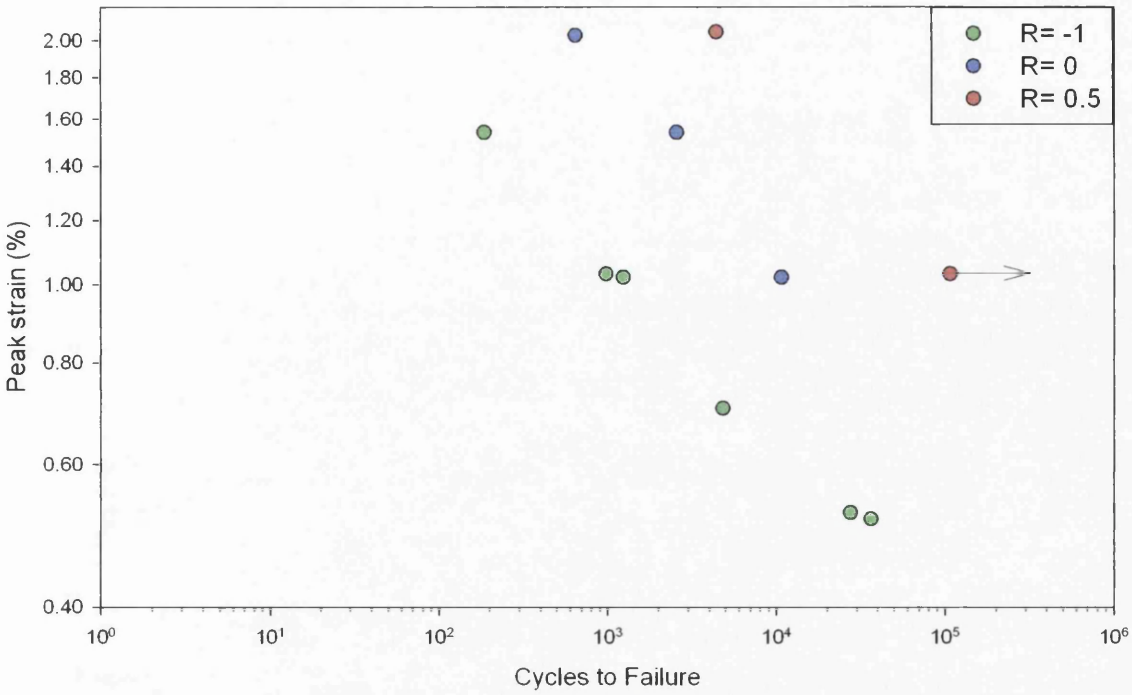


**Figure 5.1 - Strain-life at 20°C**

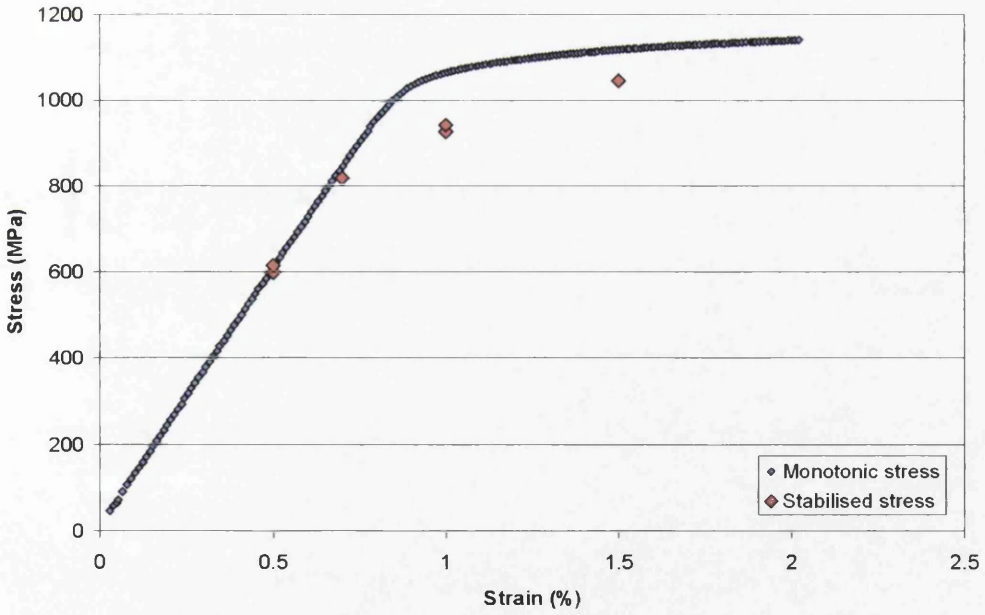


**Figure 5.2 - Cyclic and monotonic comparison at 20°C**

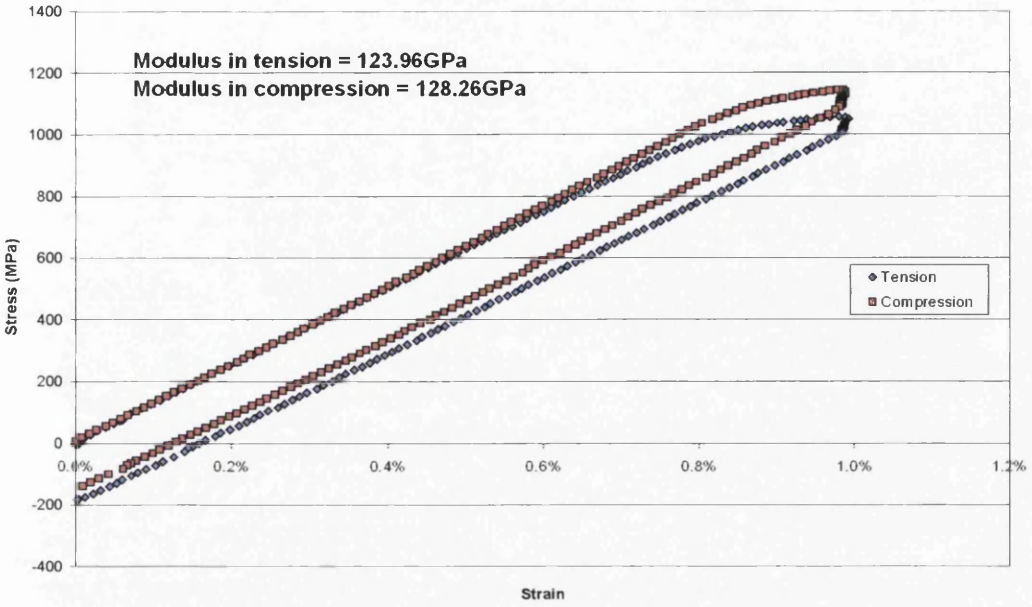


**Figure 5.3 – Comparison of tension/compression 1st loops at 20°C, R= 0**

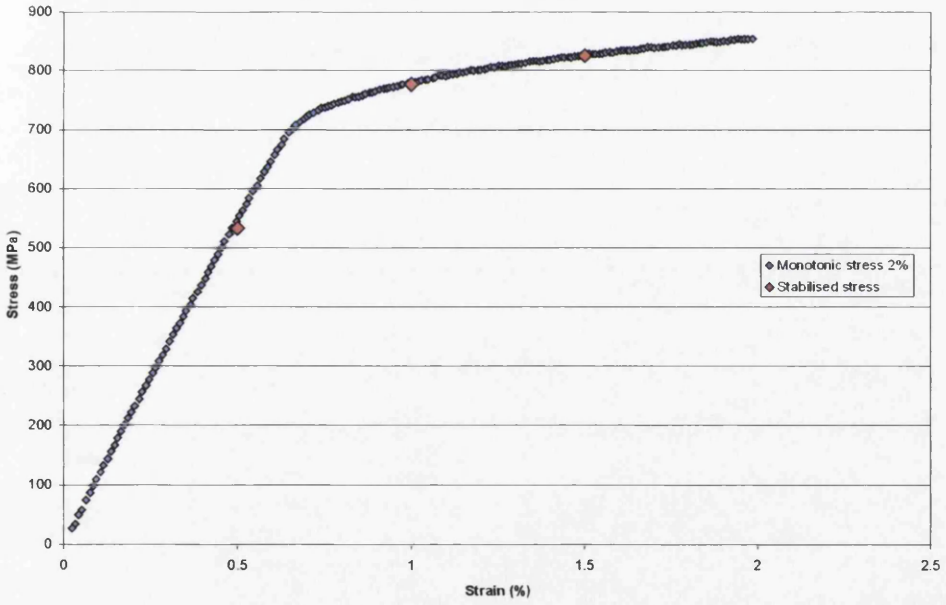


**Figure 5.4 - Cyclic and monotonic comparison at 300°C**

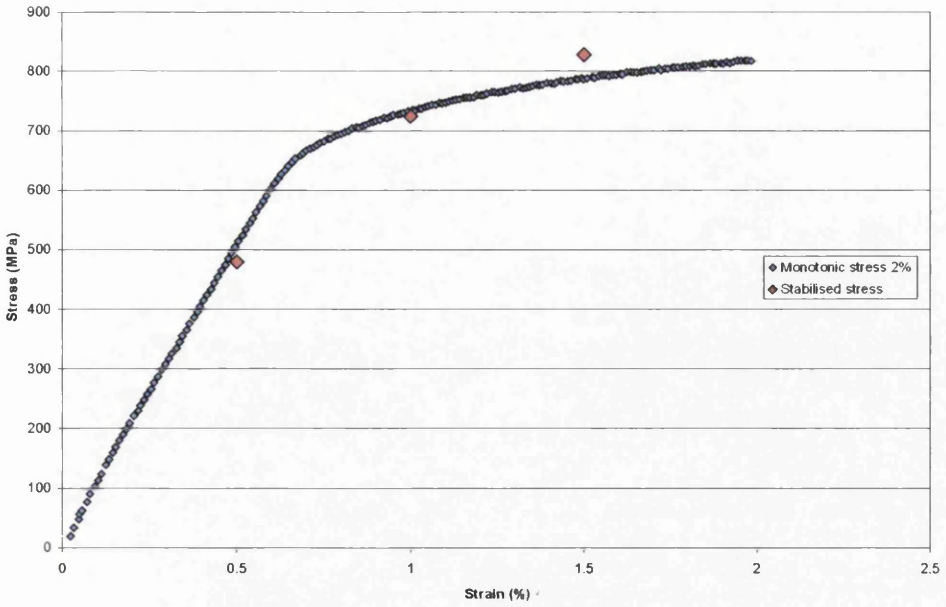


**Figure 5.5 - Cyclic and monotonic comparison at 400°C**

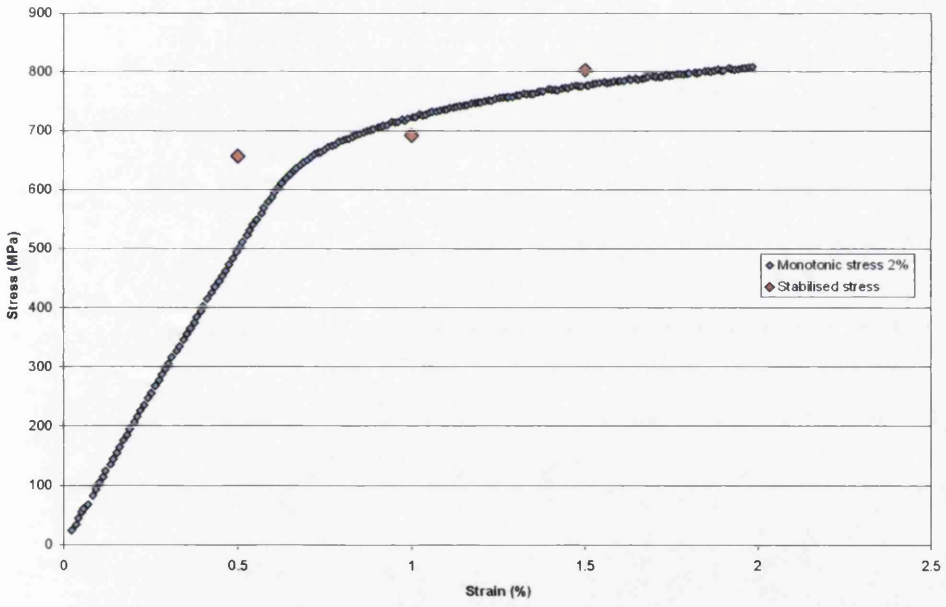


**Figure 5.6 - Cyclic and monotonic comparison at 450°C**

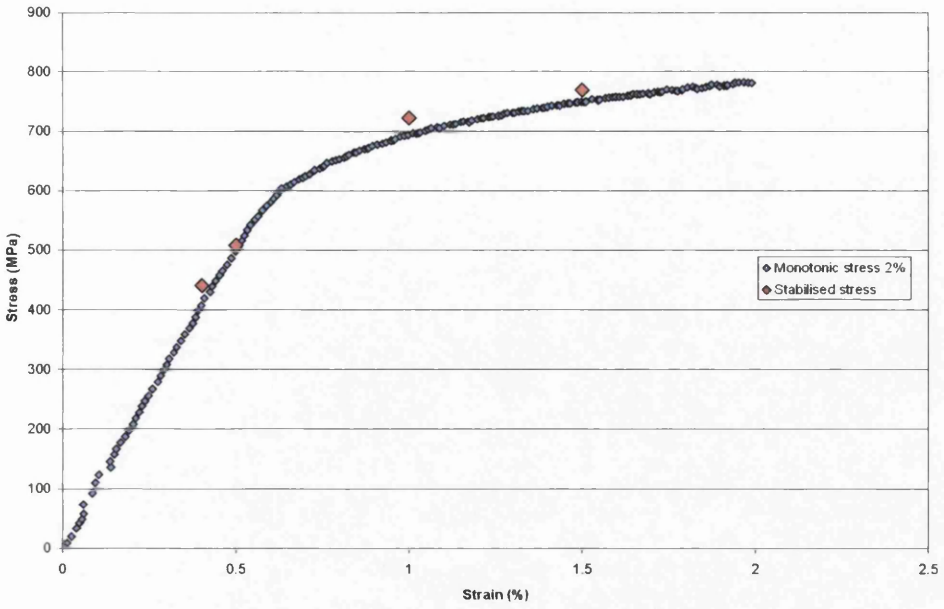


**Figure 5.7 - Cyclic and monotonic comparison at 500°C**

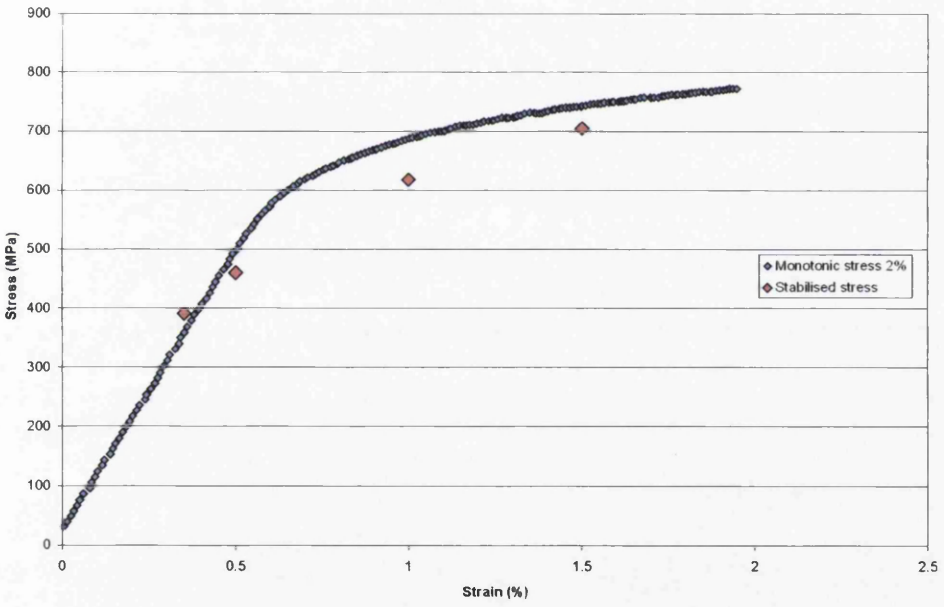


**Figure 5.8 - Cyclic and monotonic comparison at 550°C**

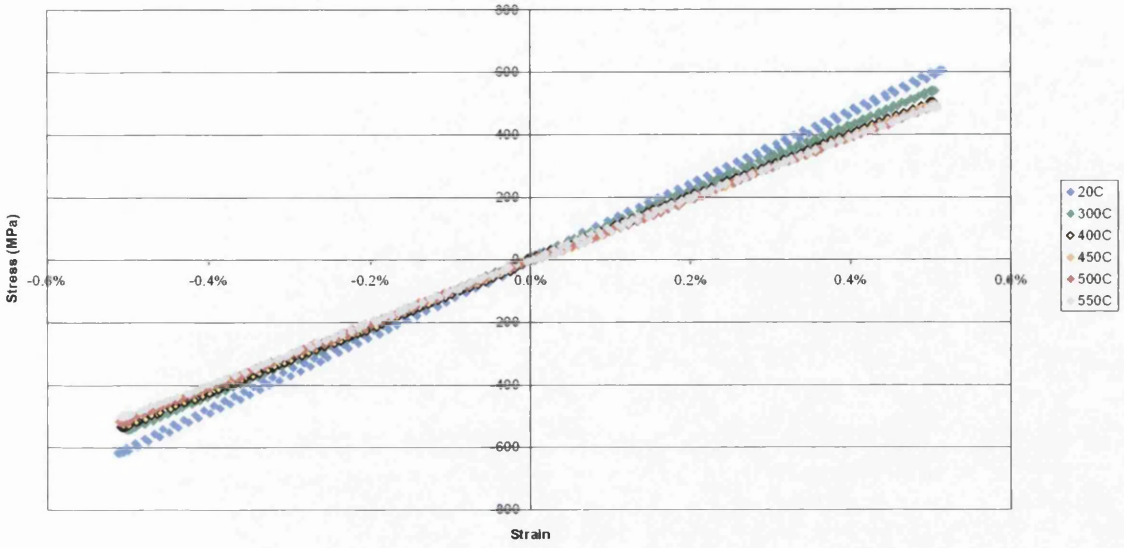


**Figure 5.9 - Comparison of initial loops of 0.5% peak strain tests for all temperatures**

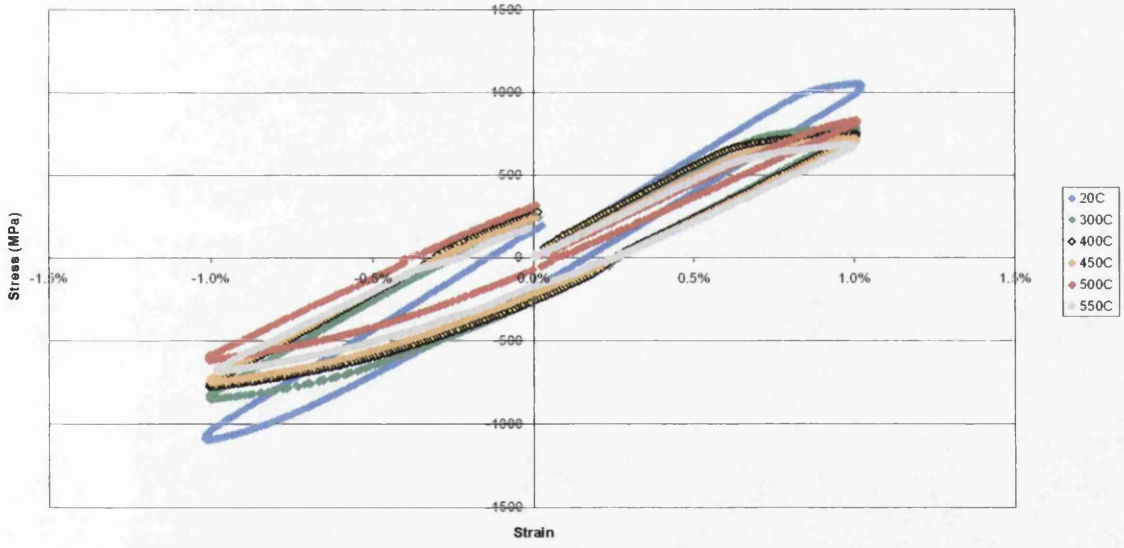


**Figure 5.10 - Comparison of initial loops of 1% peak strain tests for all temperatures**

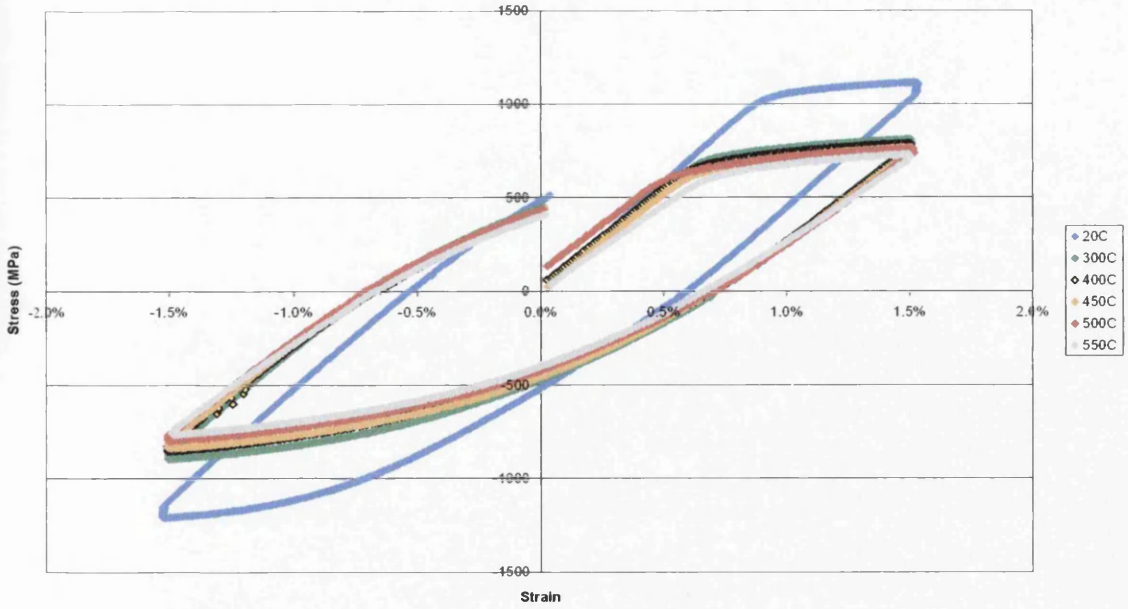


**Figure 5.11 - Comparison of initial loops of 1.5% peak strain tests for all temperatures**

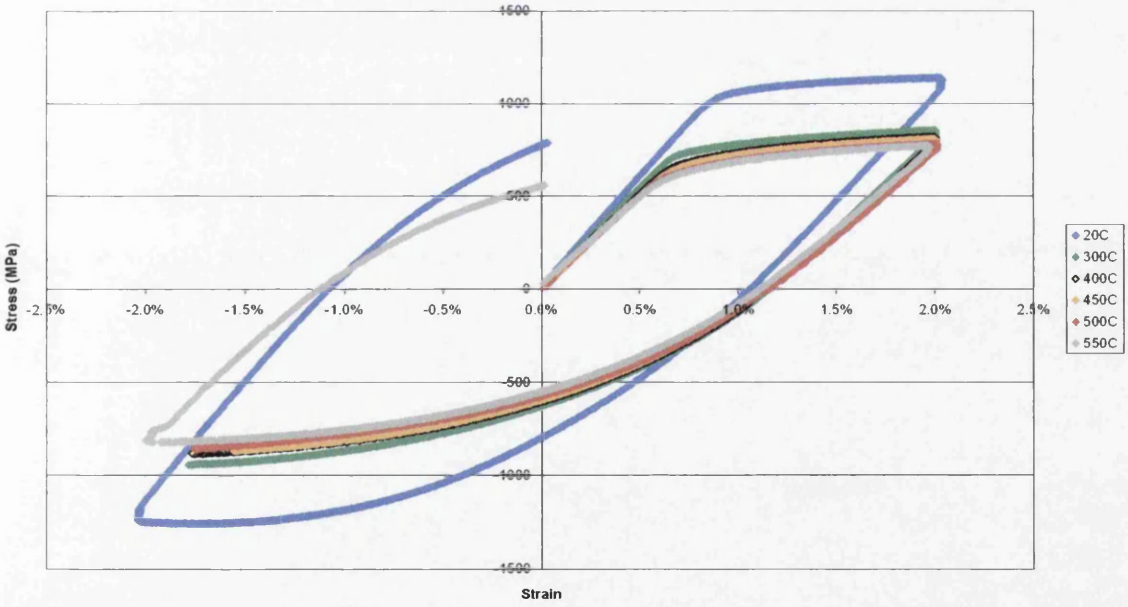


**Figure 5.12 - Comparison of initial loops of 2% peak strain tests for all temperatures**

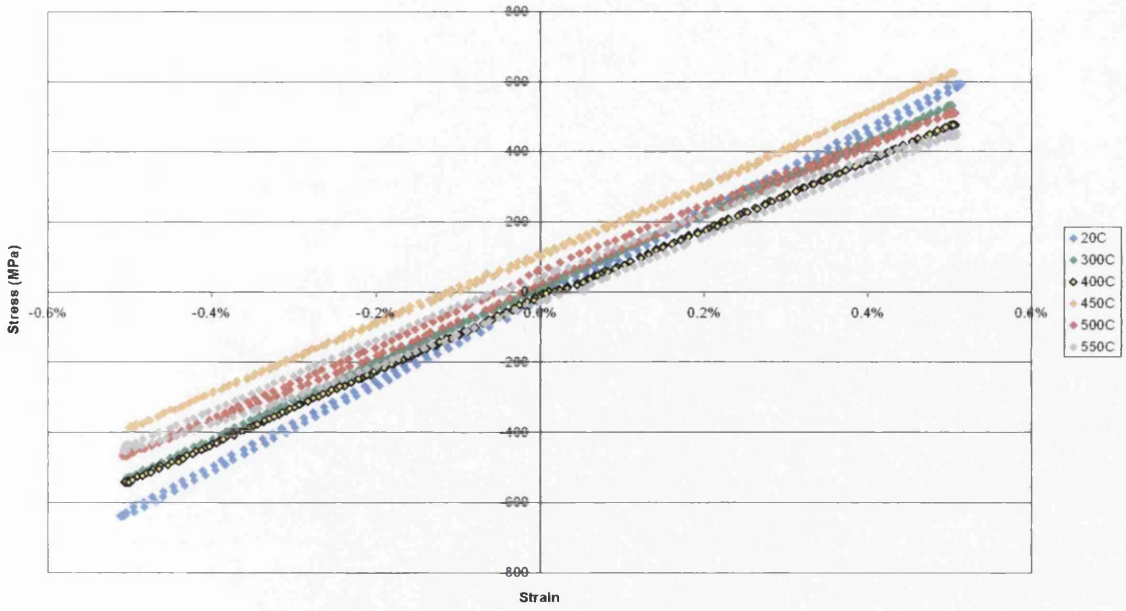


**Figure 5.13 - Comparison of stabilized loops of 0.5% peak strain tests for all temperatures**

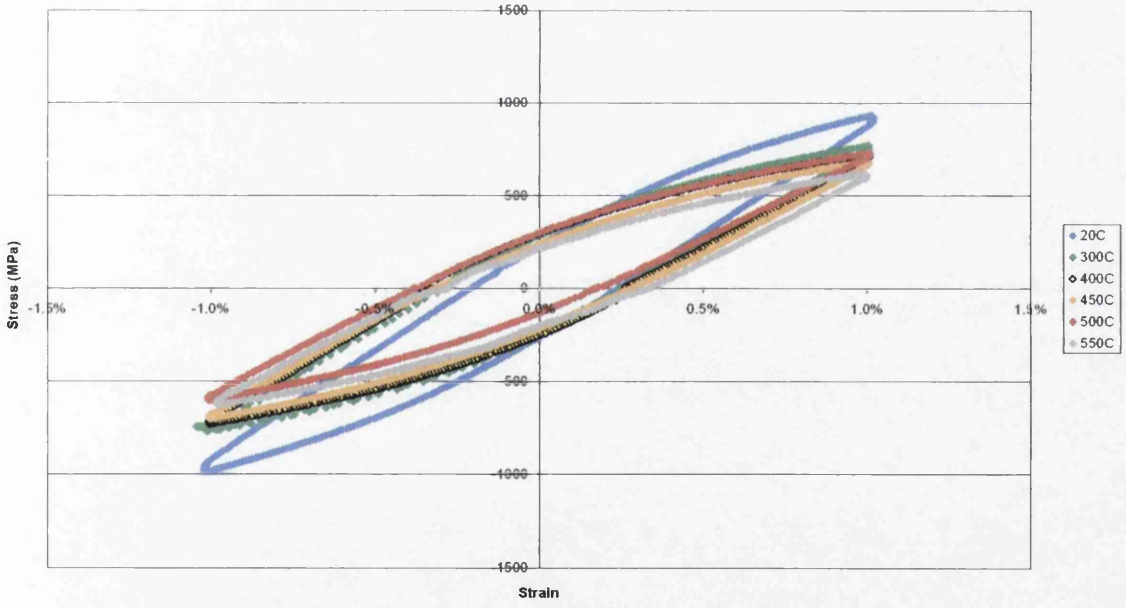


**Figure 5.14 - Comparison of stabilized loops of 1% peak strain tests for all temperatures**

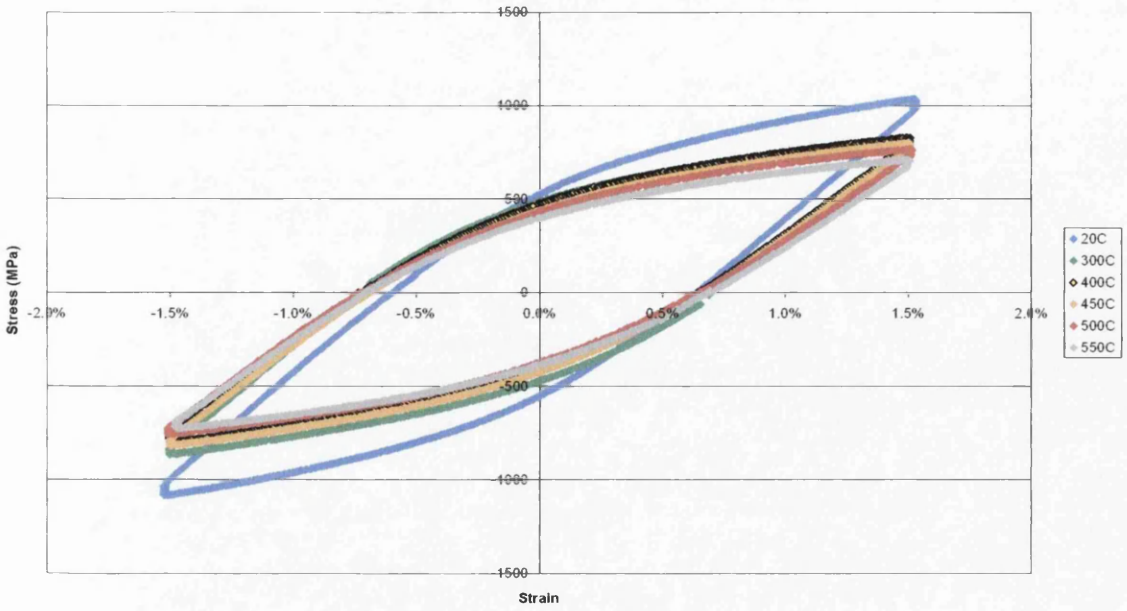


**Figure 5.15 - Comparison of stabilized loops of 1.5% peak strain tests for all temperatures**

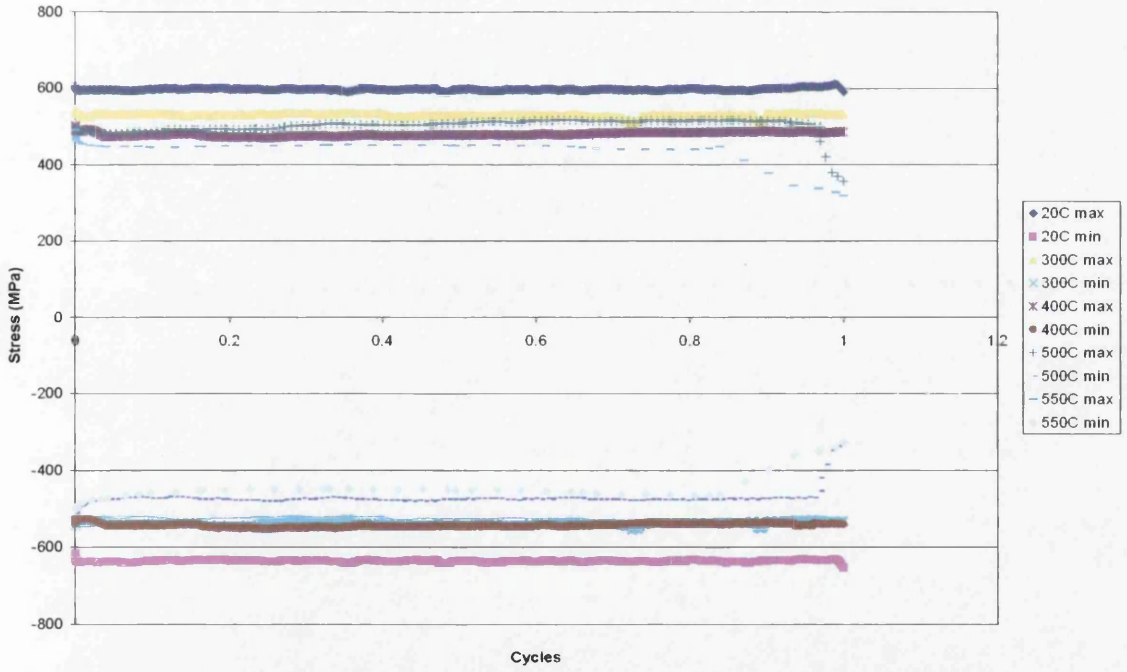


**Figure 5.16 – Normalized comparison of max/min stress – cycles of 0.5% peak strain tests at all temperatures**

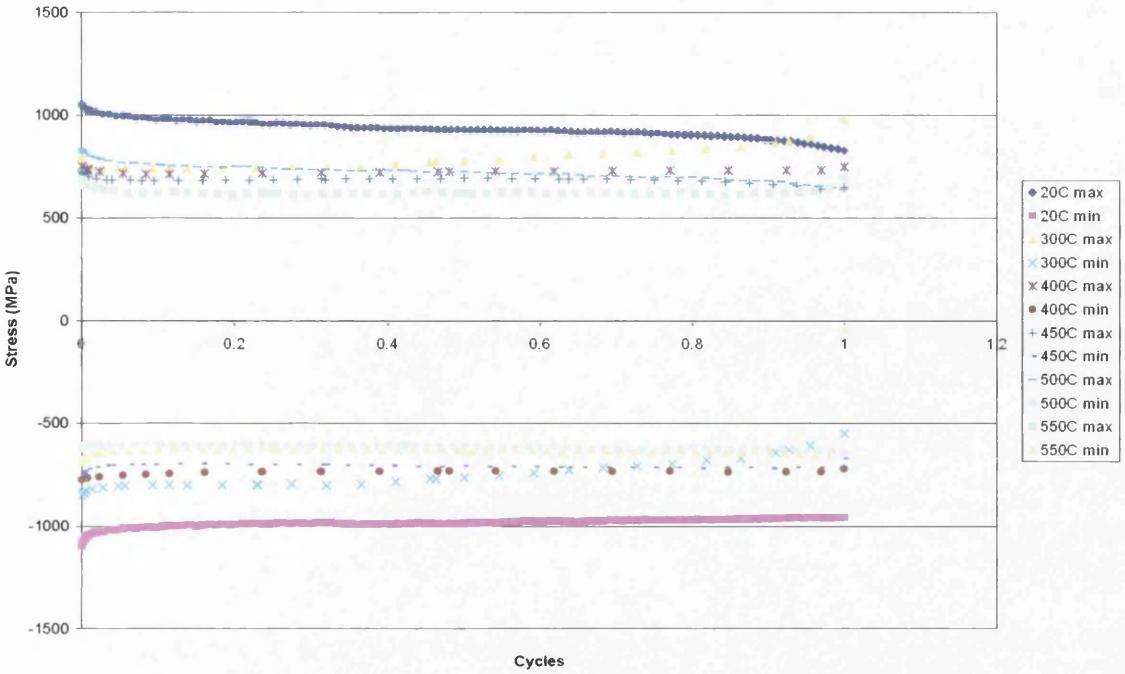


**Figure 5.17 - Normalized comparison of max/min stress – cycles of 1% peak strain tests at all temperatures**

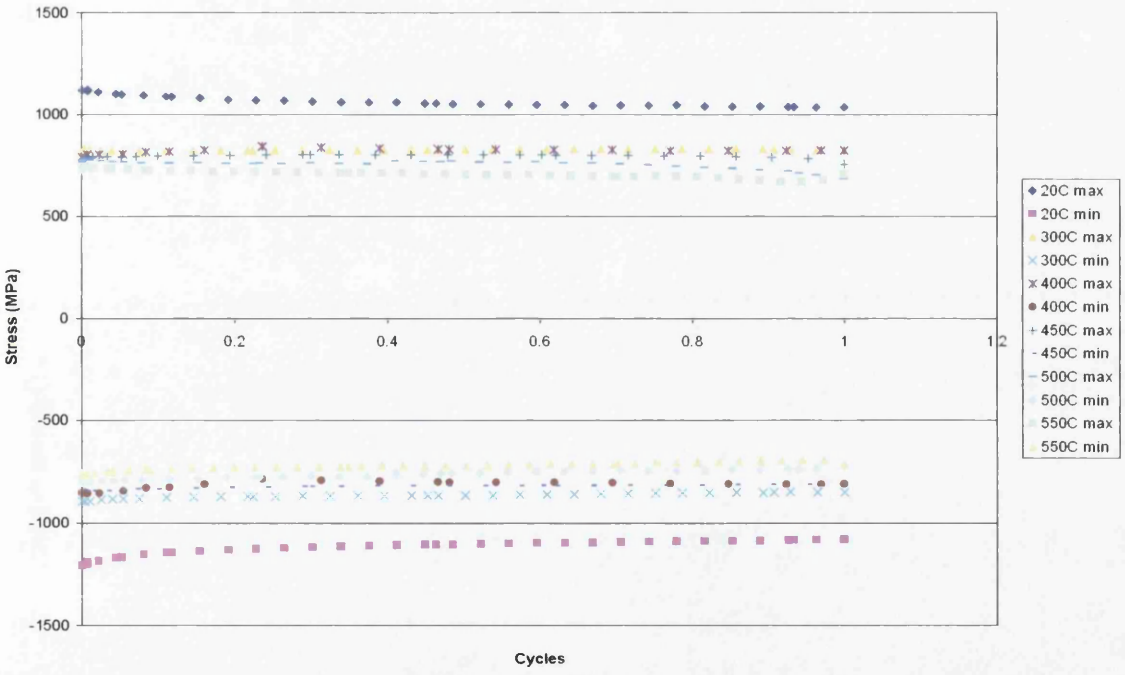


**Figure 5.18 - Normalized comparison of max/min stress – cycles of 1.5% peak strain tests at all temperatures**

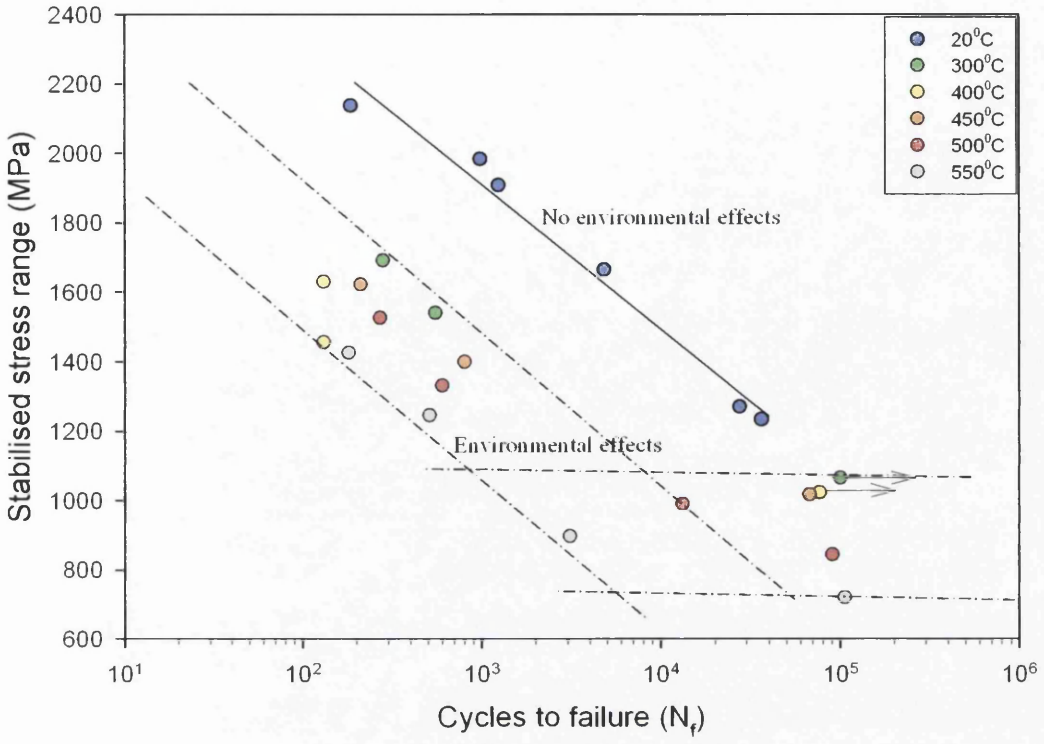


**Figure 5.19 – Stabilised stress – life comparison of cyclic strain control data at all temperatures**

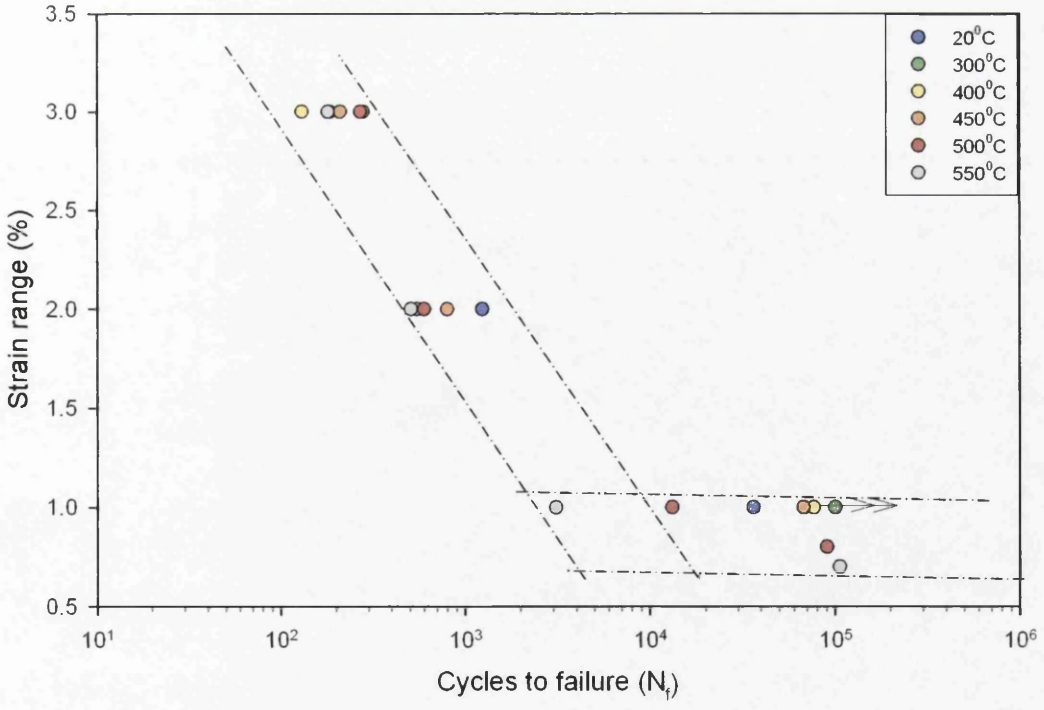


**Figure 5.20 – Strain range vs life comparison of cyclic strain control data at all temperatures**

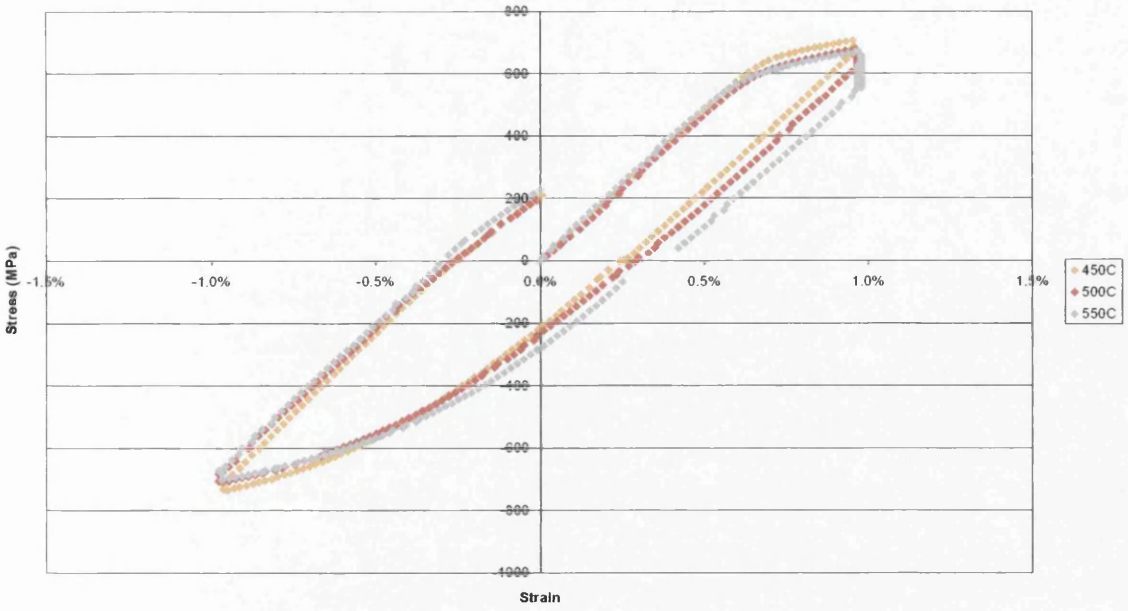


**Figure 5.21 - Comparison of unbalanced 2 minute dwell, initial loops at 450 – 550°C**

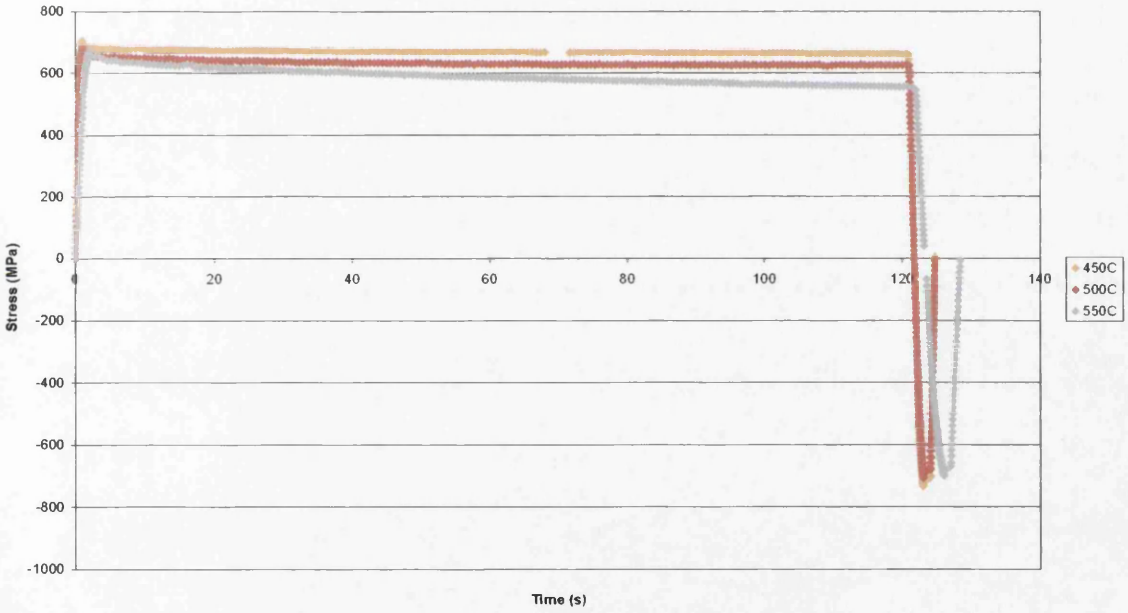


**Figure 5.22 – Stress-time comparison of initial cycles of unbalanced 2 minute dwell at 450 – 550°C**

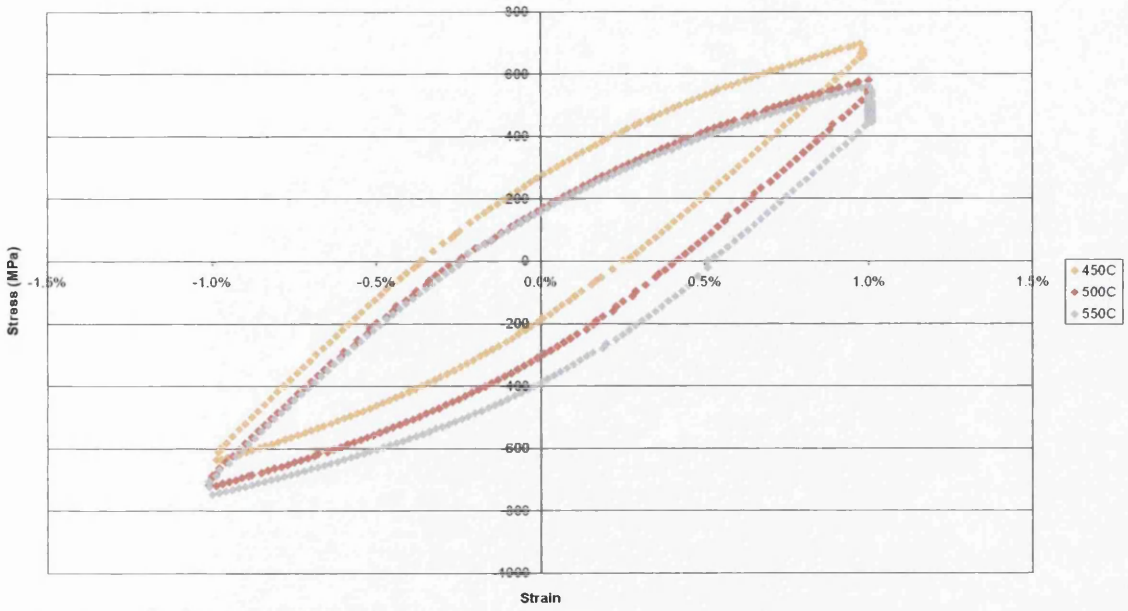


**Figure 5.23 - Comparison of unbalanced 2 minute dwell, stabilised loops at 450 – 550°C**

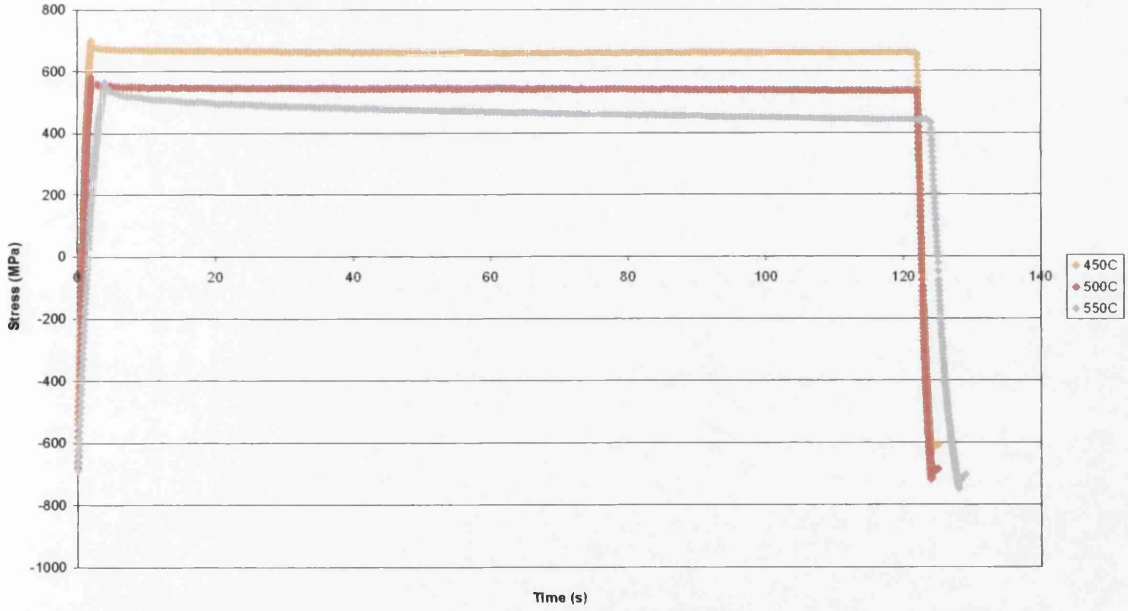


**Figure 5.24 - Stress-time comparison of stabilised cycles of unbalanced 2 minute dwell at 450 – 550°C**

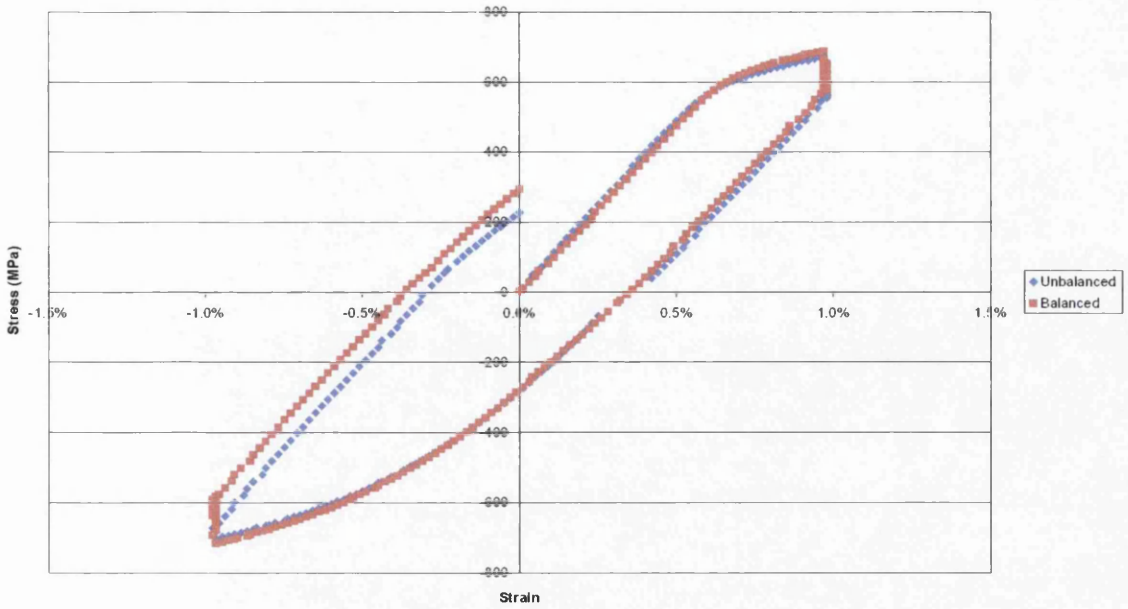


**Figure 5.25 - Comparison of initial loops of balanced and unbalanced 2 minute dwell at 550°C**

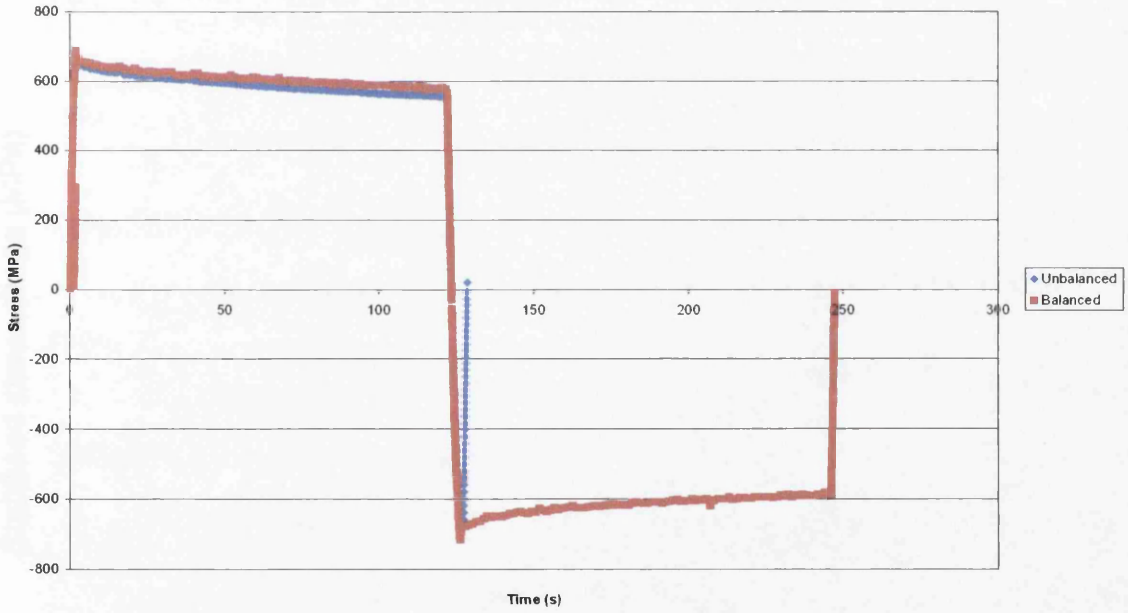


**Figure 5.26 - Stress-time plot of stabilised cycle of 2 minute dwell in tension at 450 – 550°C**

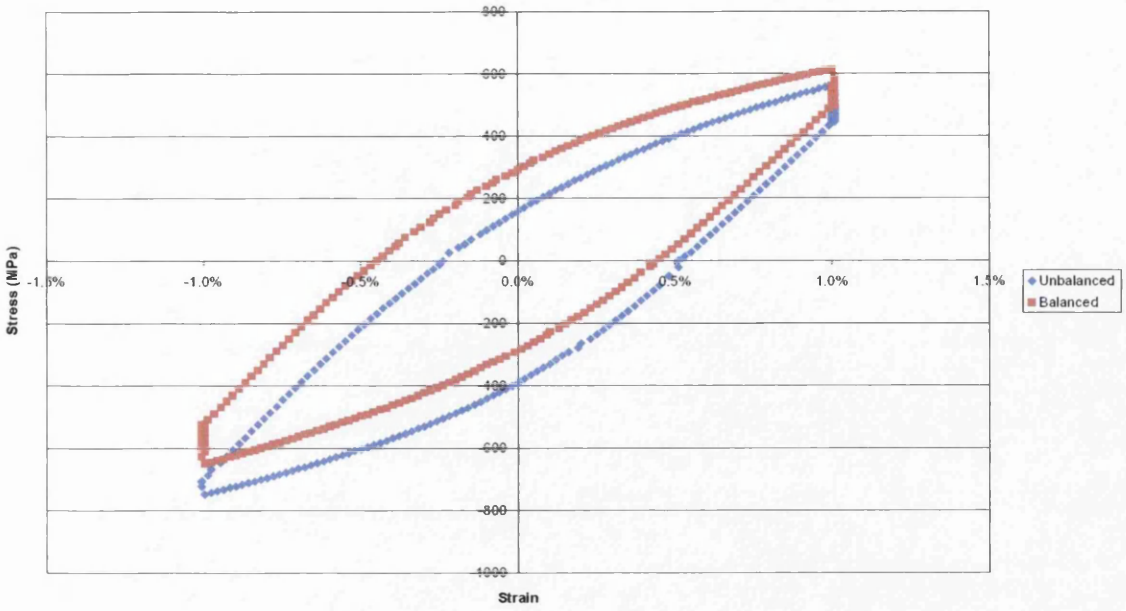


**Figure 5.27 - Comparison of stabilised loops of balanced and unbalanced 2 minute dwell at 550°C**

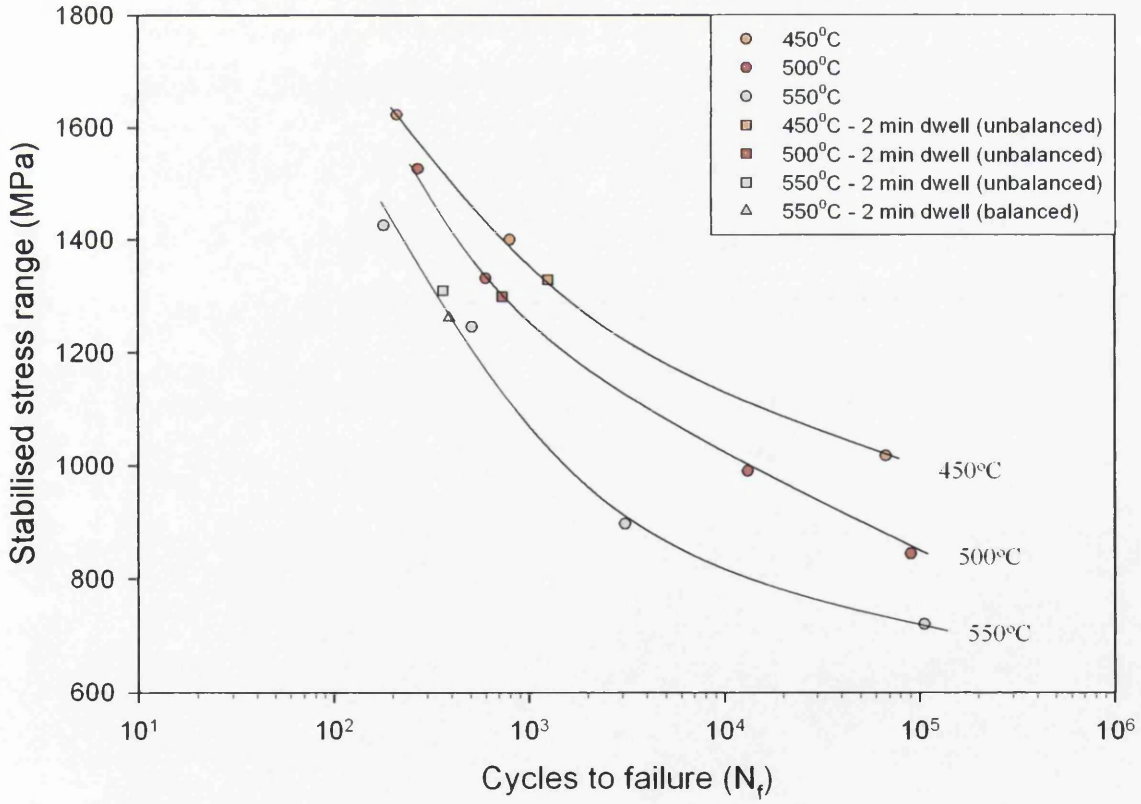


**Figure 5.28 – Stabilised stress range – life comparison of cyclic and dwell tests**

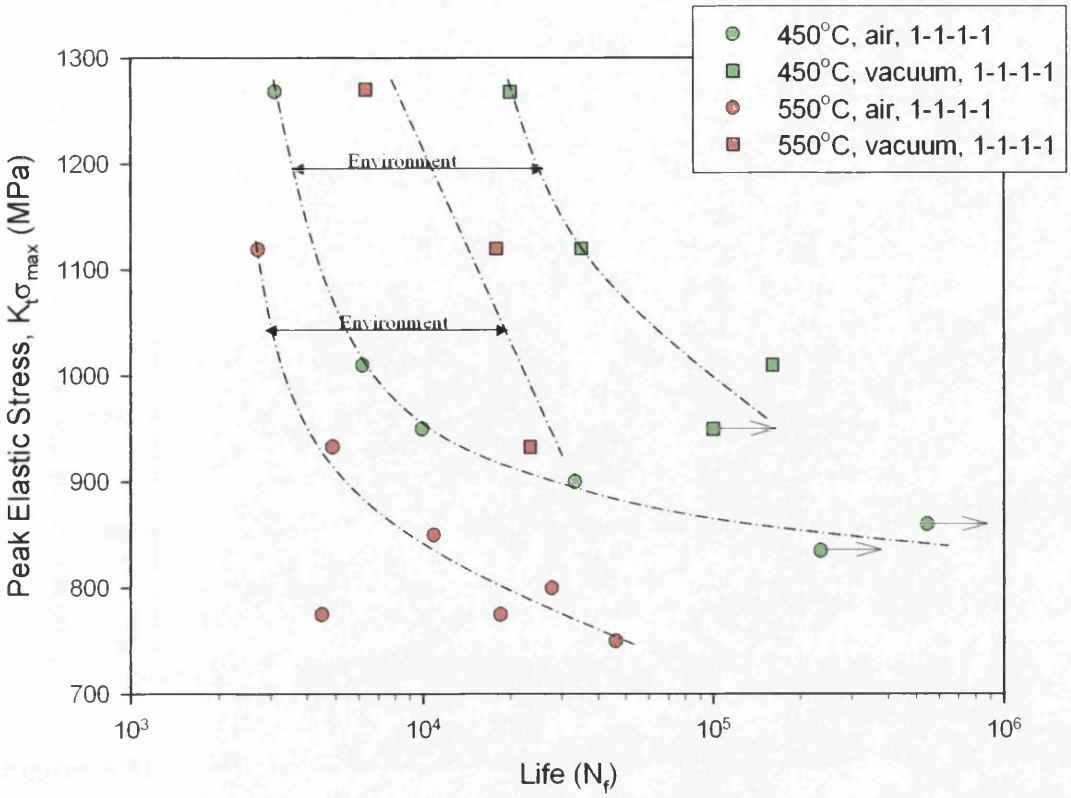


**Figure 5.29 – Comparison of cyclic air and vacuum DEN data at 450 and 550°C**

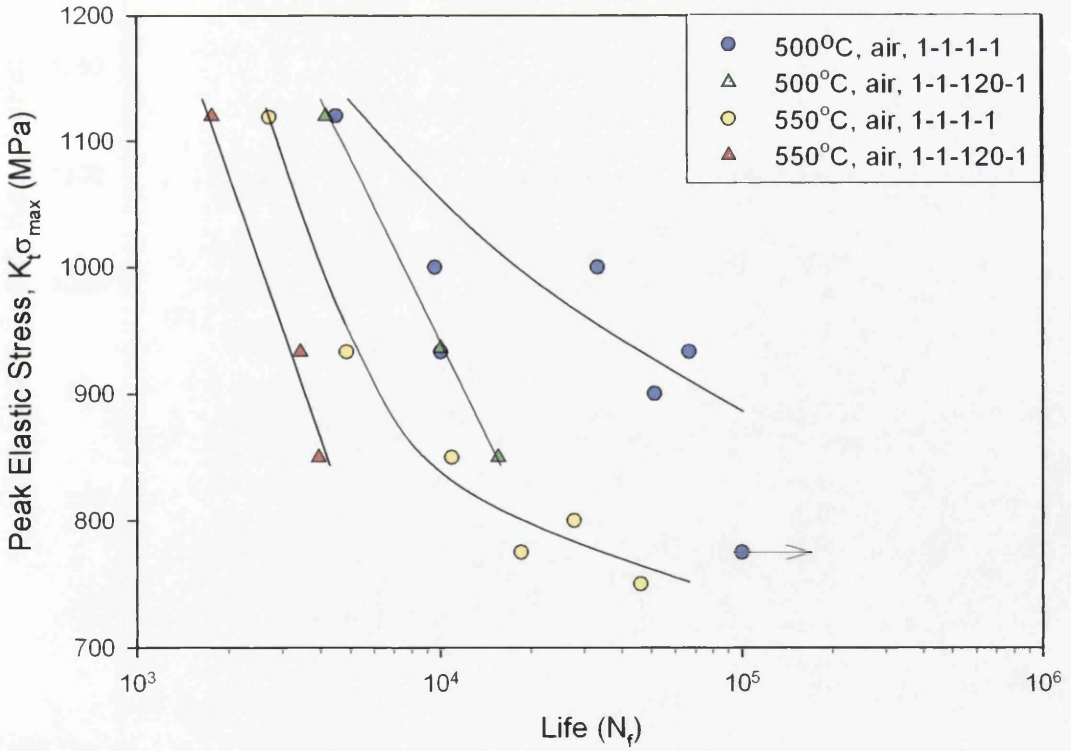


**Figure 5.30 - Comparison of cyclic and dwell DEN data at 500 and 550°C, in air**

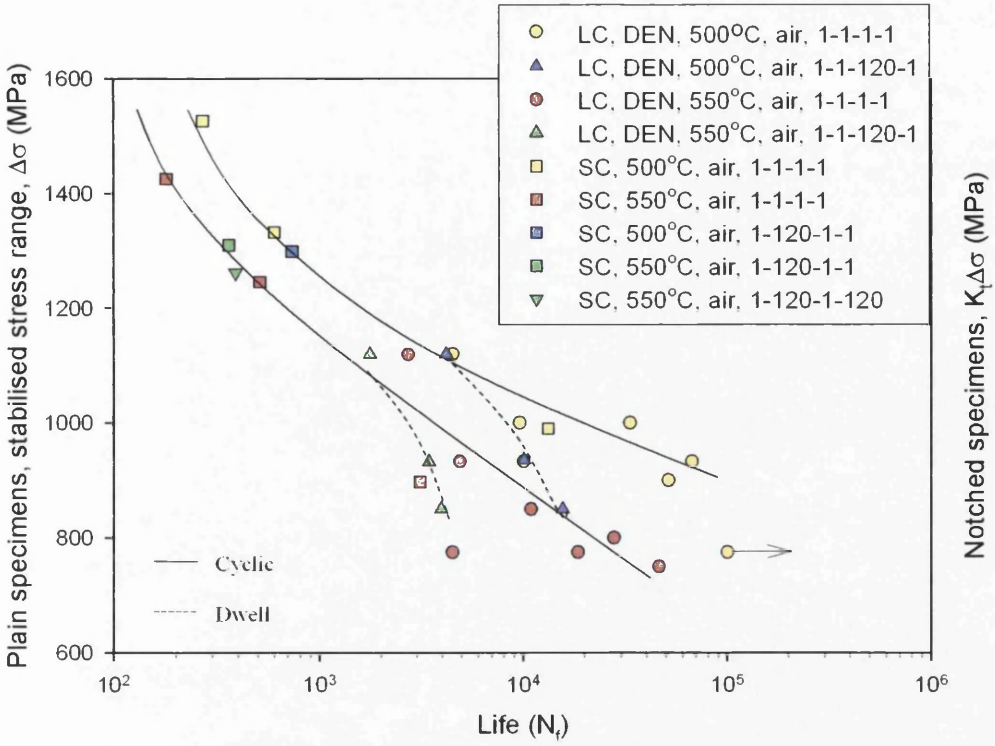


**Figure 5.31 – Comparison of cyclic and dwell strain and load control DEN data**

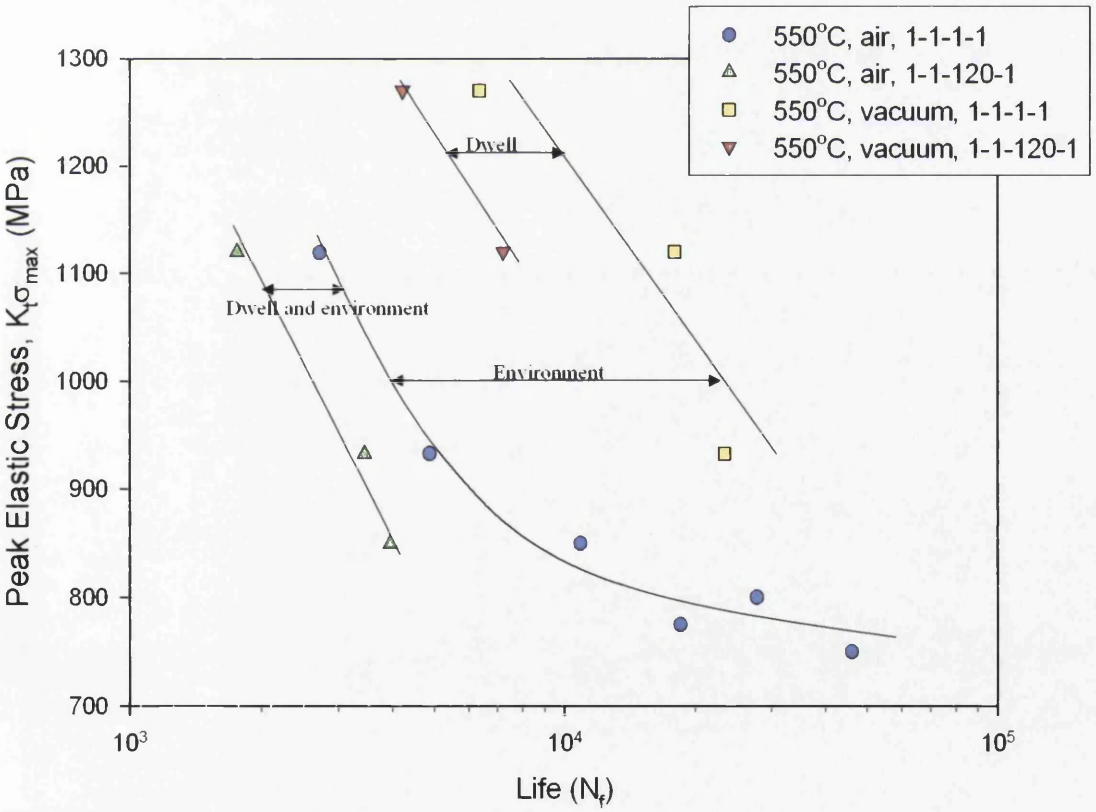


**Figure 5.32 – Comparison of cyclic and 2 minute dwell data in air and vacuum at 550°C**

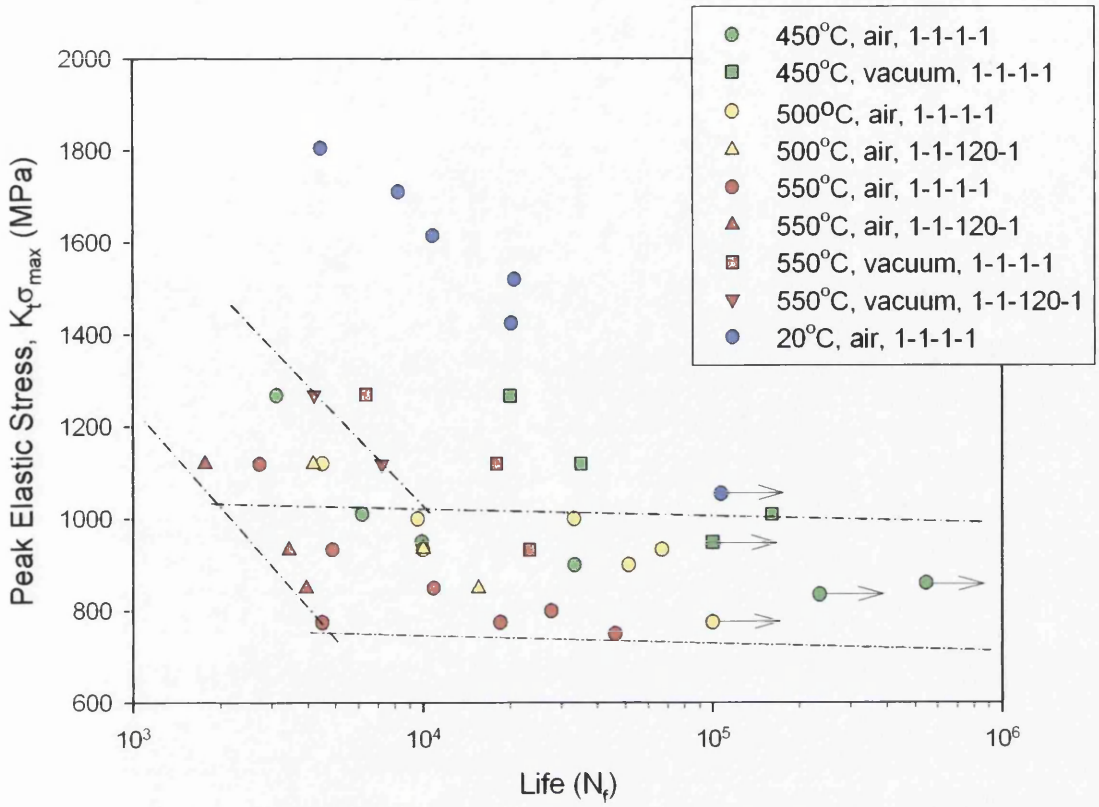


**Figure 5.33 – Comparison of all DEN data**

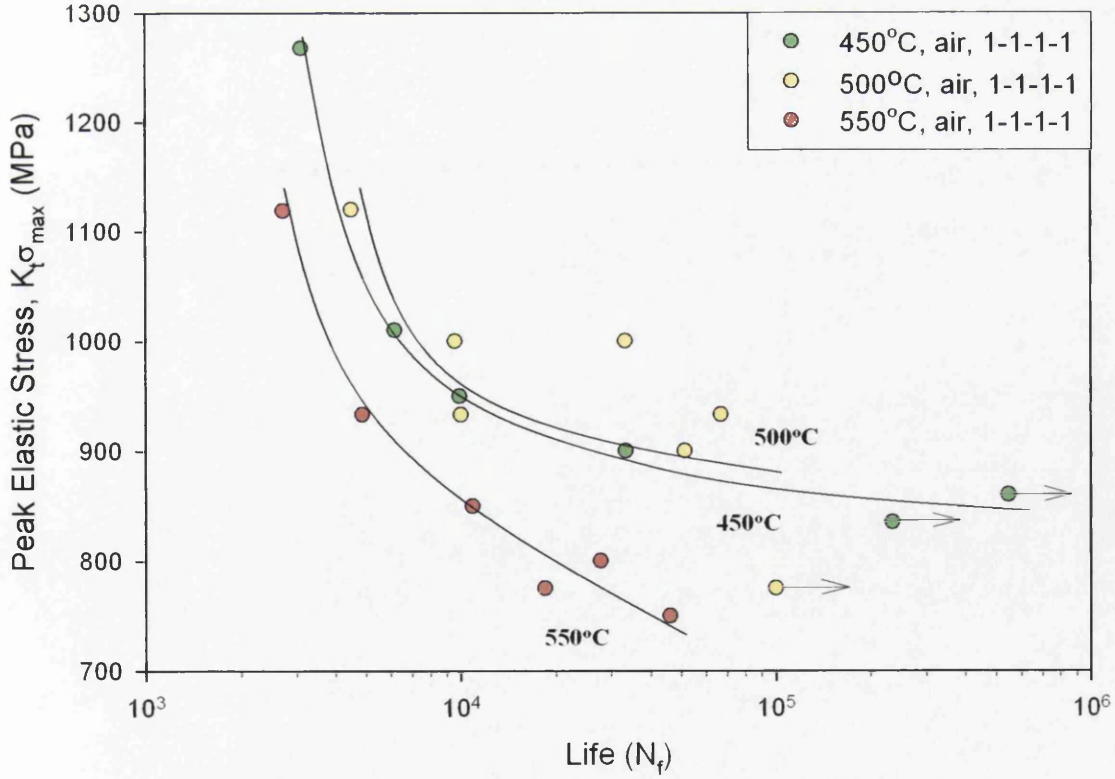


**Figure 5.34 Comparison of cyclic DEN tests at elevated temperatures**

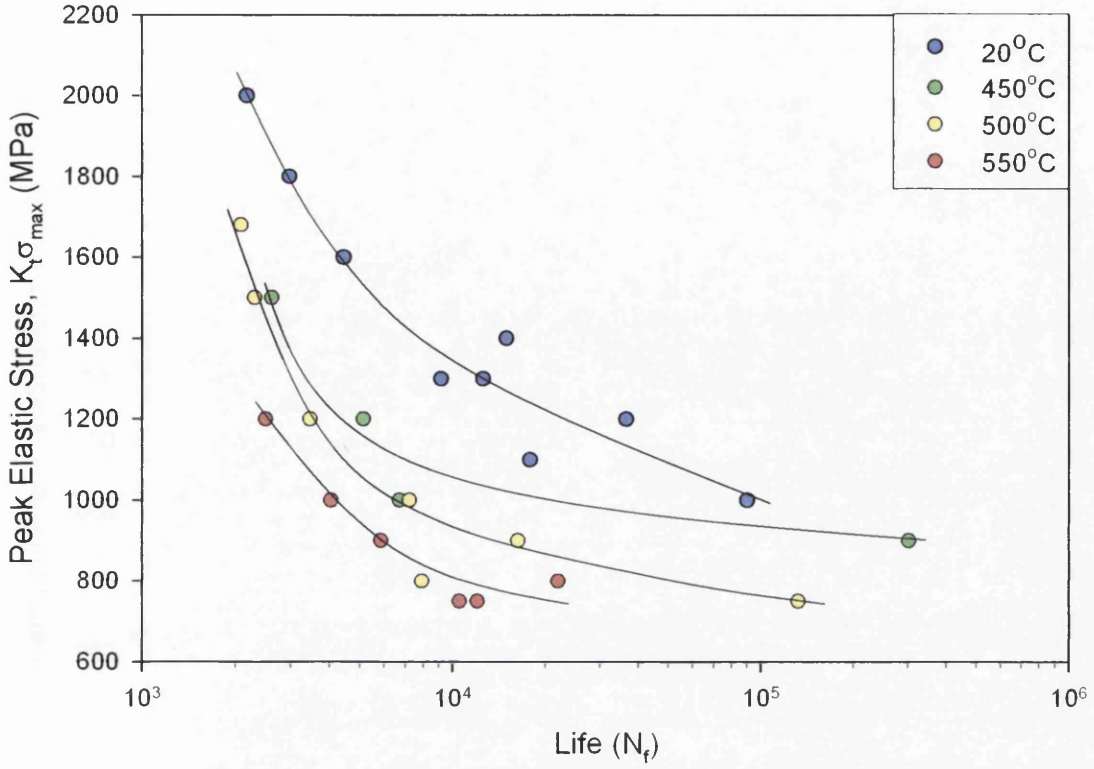


**Figure 5.35 – Comparison of cyclic VCN from 20°C – 550°C**

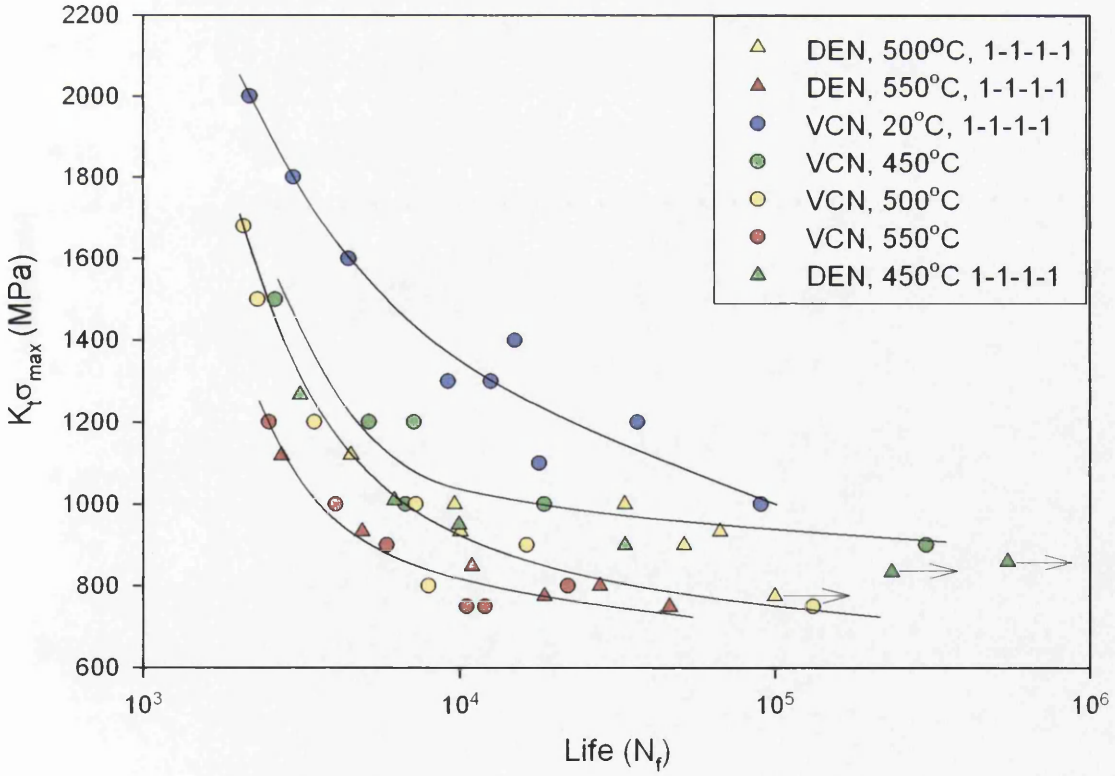


**Figure 5.36 – Comparison of DEN and VCN cyclic data**

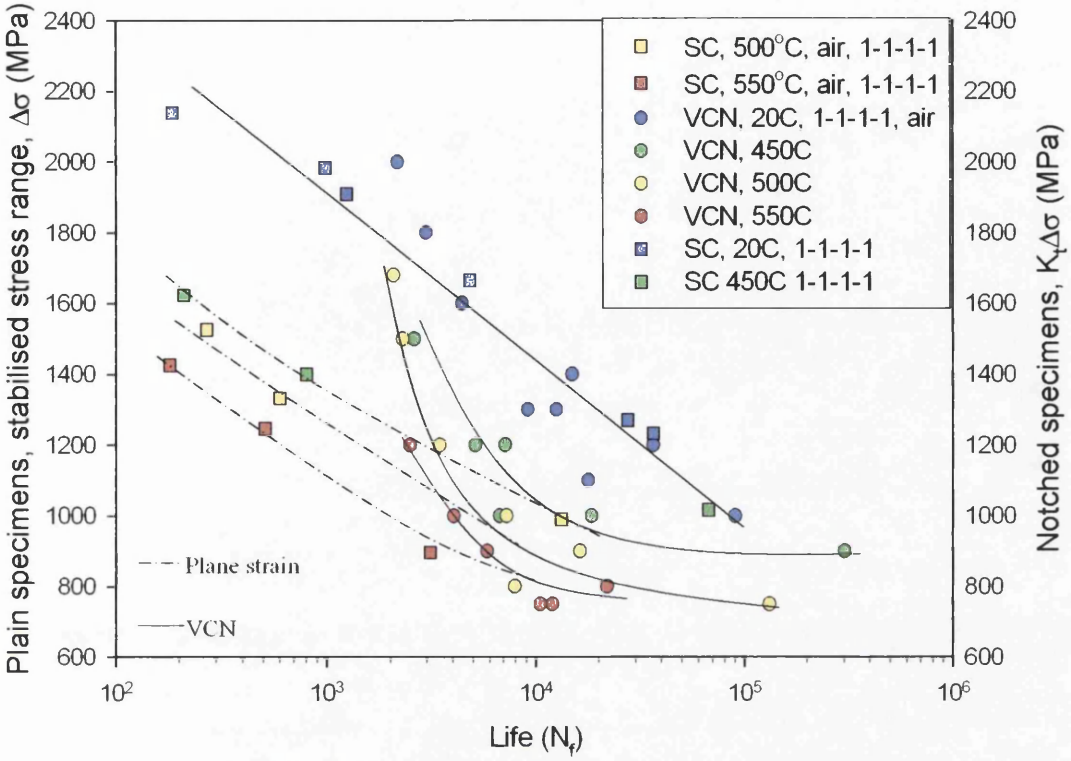


**Figure 5.37 - Comparison of strain control and VCN data**

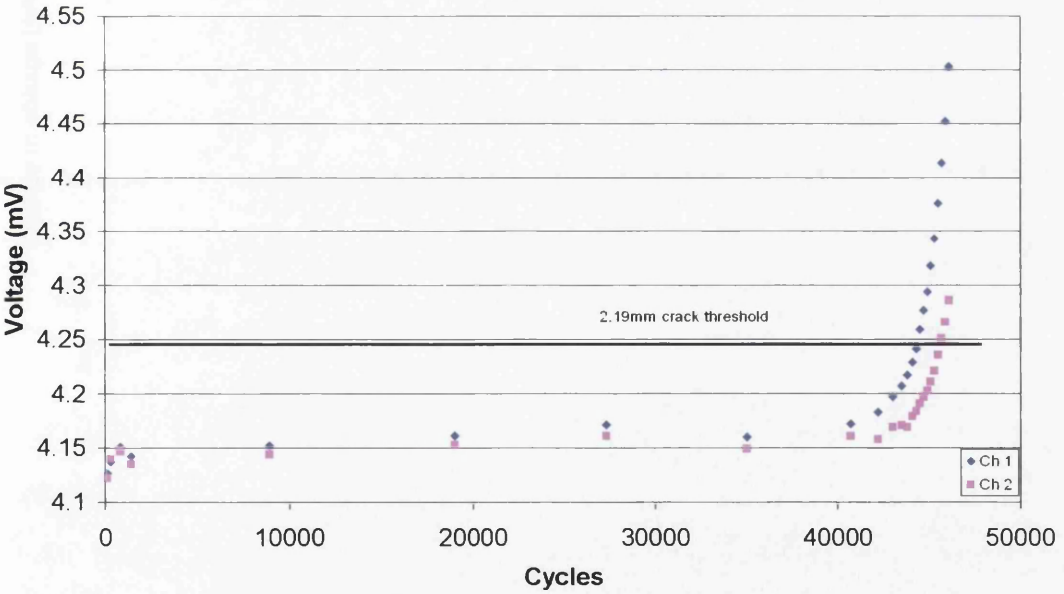


**Figure 5.38 – Voltage for a cyclic freely initiated DEN (550°C, 750MPa peak stress, $N_f$=46104)**

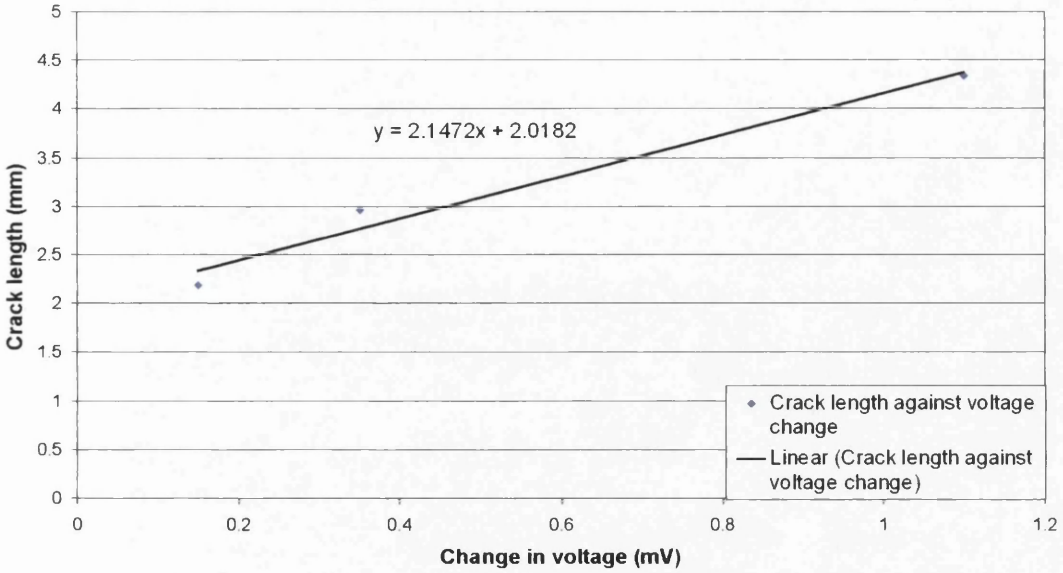


**Figure 5.39 – Crack length against voltage change for freely initiated DEN specimens**

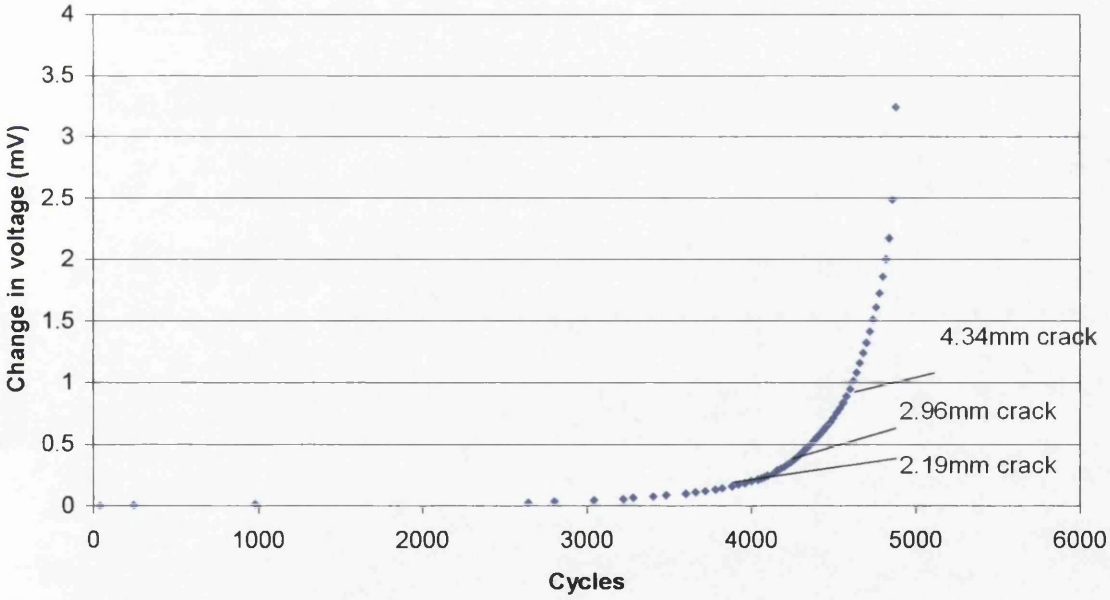


**Figure 5.40 - Voltage against cycles for a cyclic freely initiated DEN (933MPa peak stress, $N_f$=4882)**

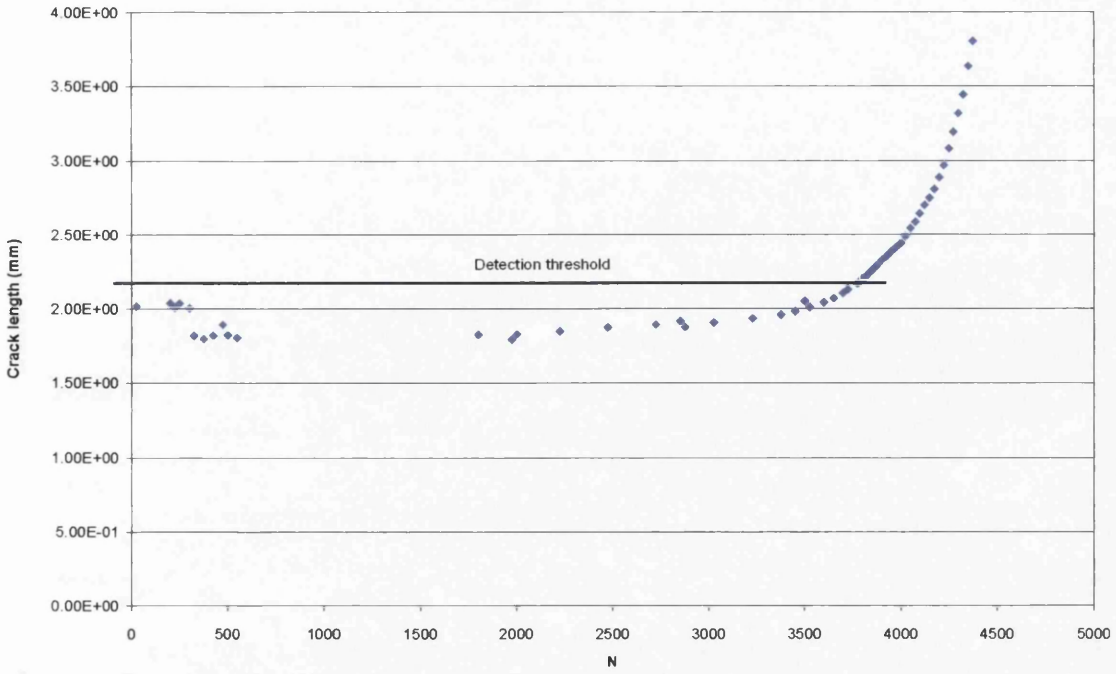


**Figure 5.41 – Change in length against cycles for a cyclic freely initiated DEN (1120MPa peak stress, Nf = 4507)**

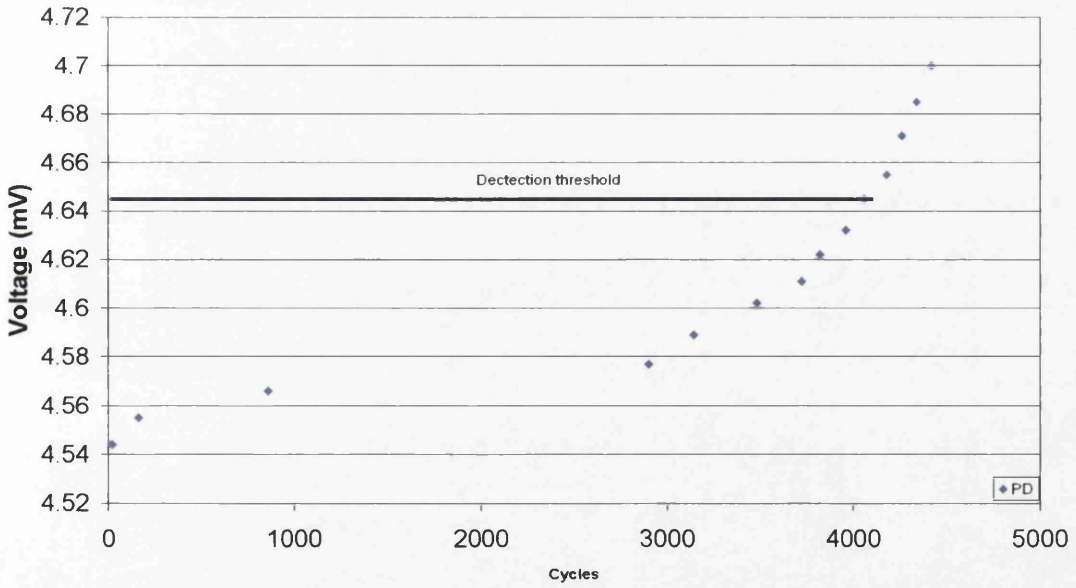


**Figure 5.42 - Voltage against cycles for a cyclic freely initiated DEN (936MPa peak stress, Nf=4424)**

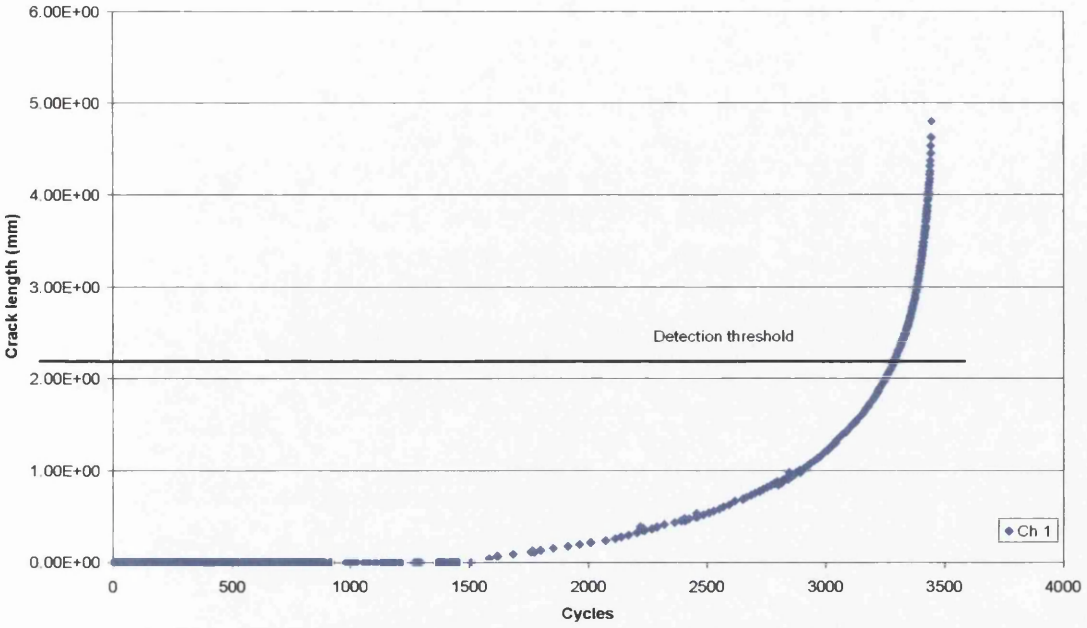


**Figure 5.43 – Crack length against cycles for a cyclic freely initiated DEN test (550C, 1-120-1-1, 933MPa peak stress)**

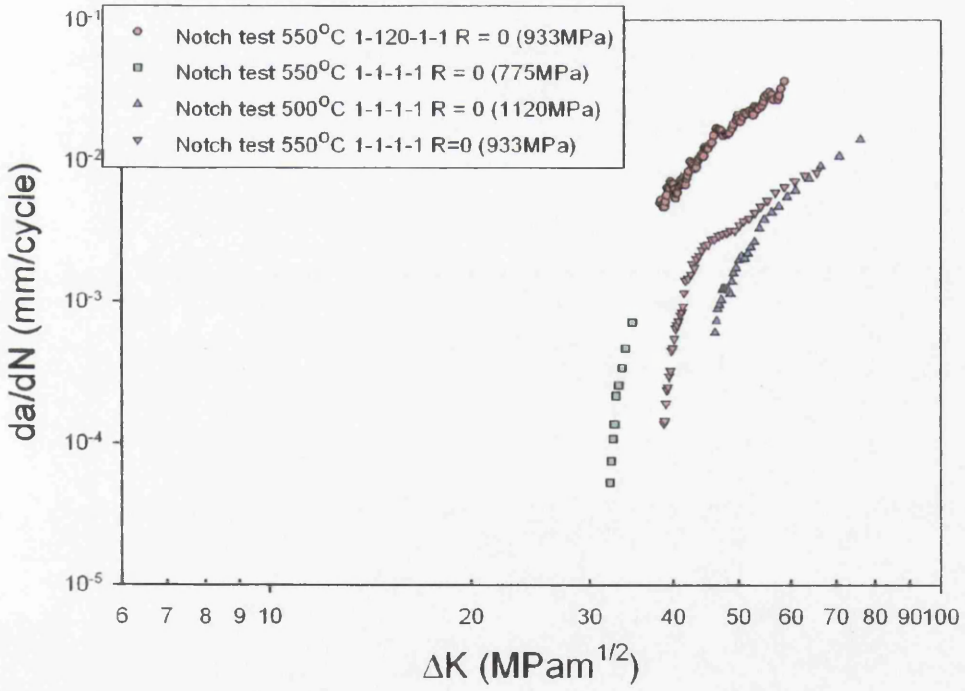


**Figure 5.44 – Comparison of freely initiated DEN crack propagation tests**

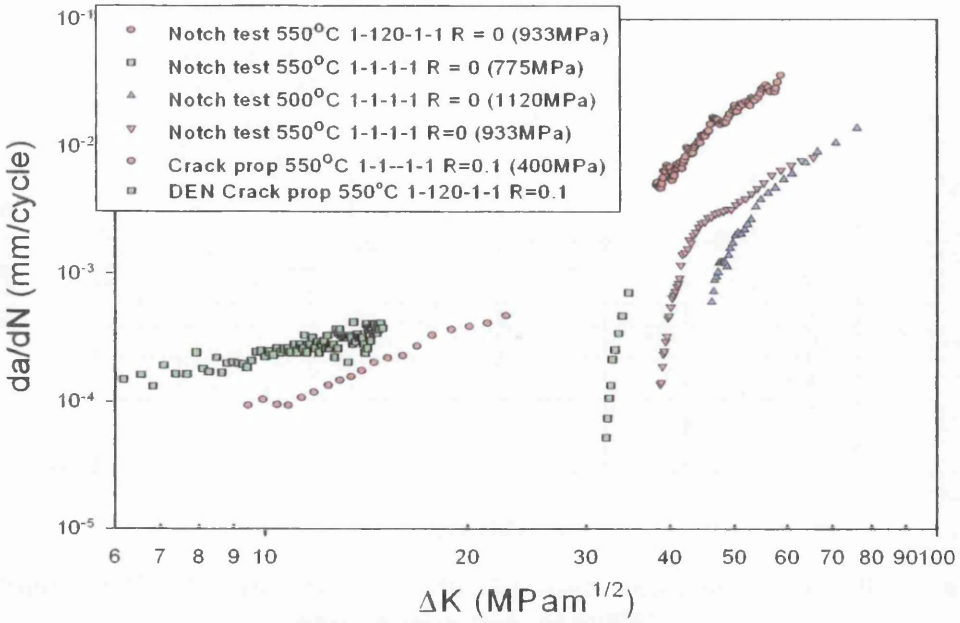


**Figure 5.45 - Comparison of freely initiated DEN and corner crack propagation tests**

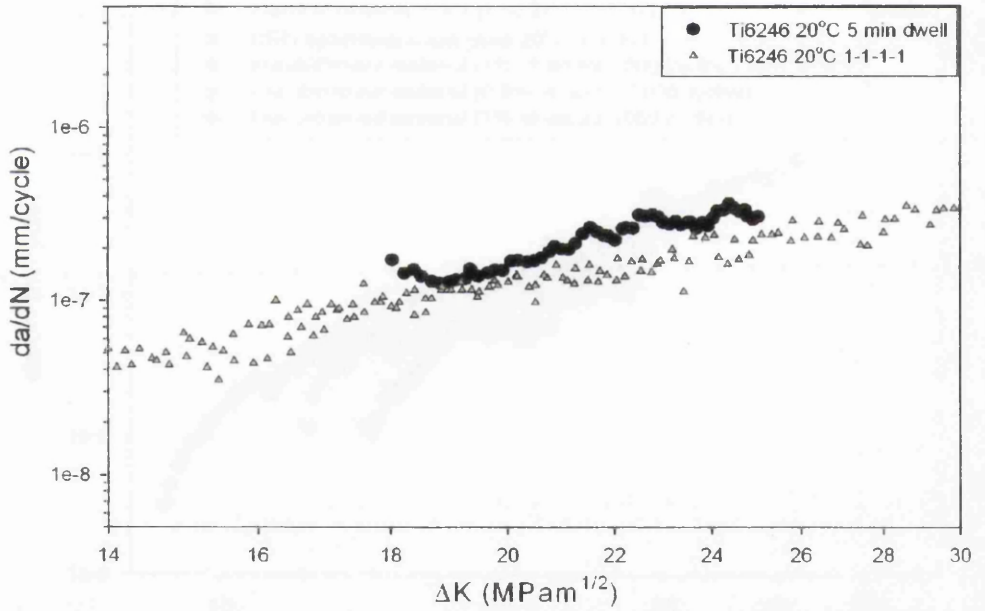


**Figure 5.46 – Comparison of cyclic and 5 minute dwell crack propagation tests at 20°C**

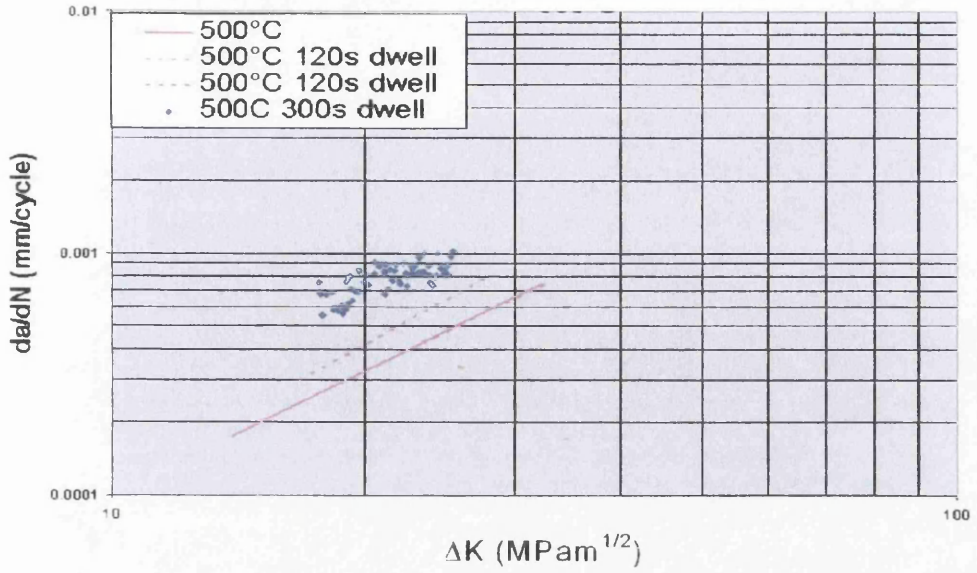


**Figure 5.47 – Comparison of cyclic, 2 minute and 5 minute dwell crack propagation tests at 500°C.**

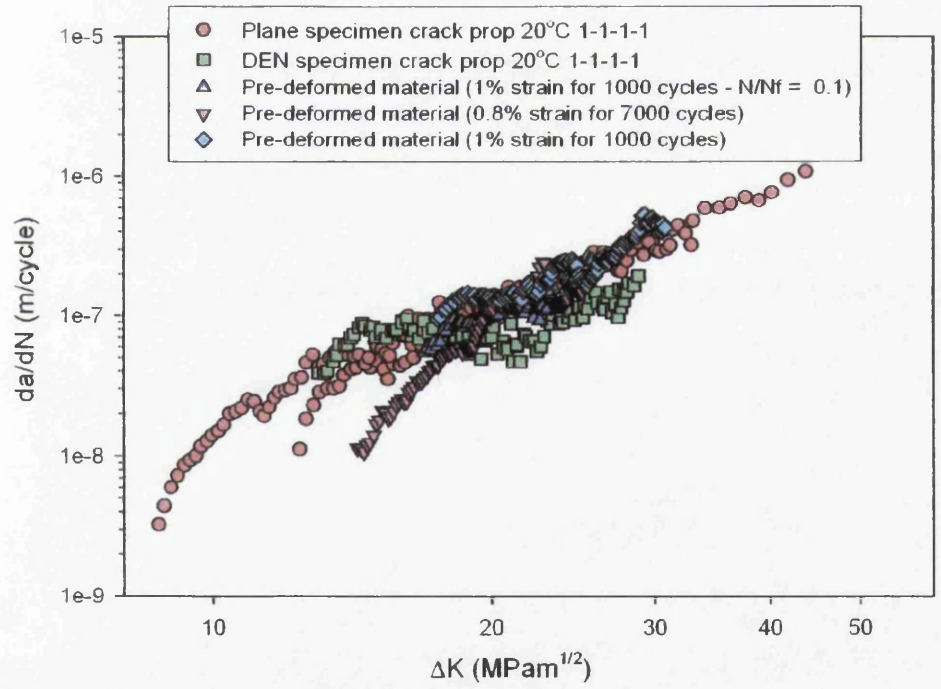


**Figure 5.48 - Comparison of pre-deformed and standard crack propagation tests**

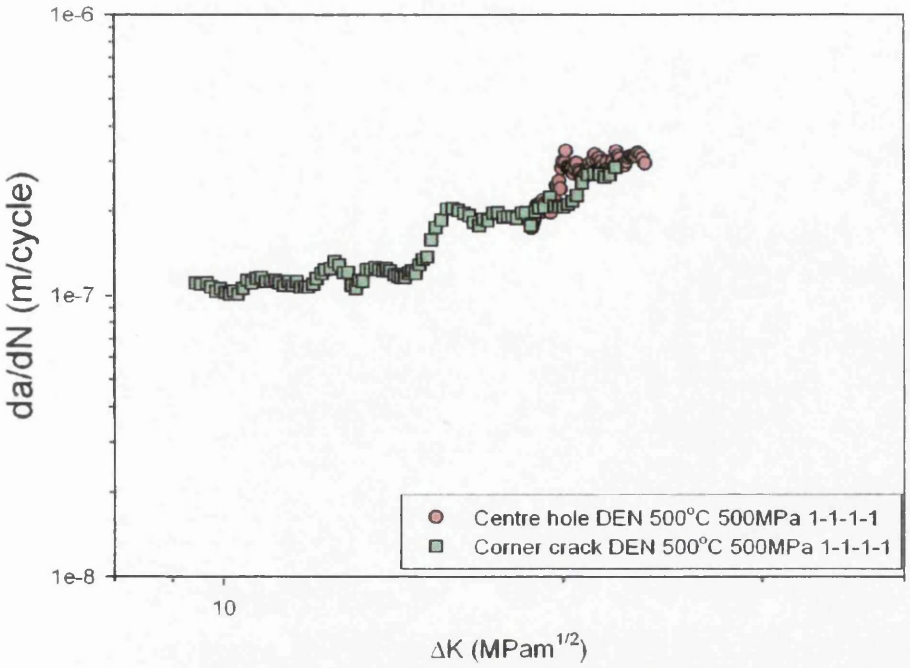


**Figure 5.49– Comparison of centre hole and corner cracked DEN crack propagation tests.**

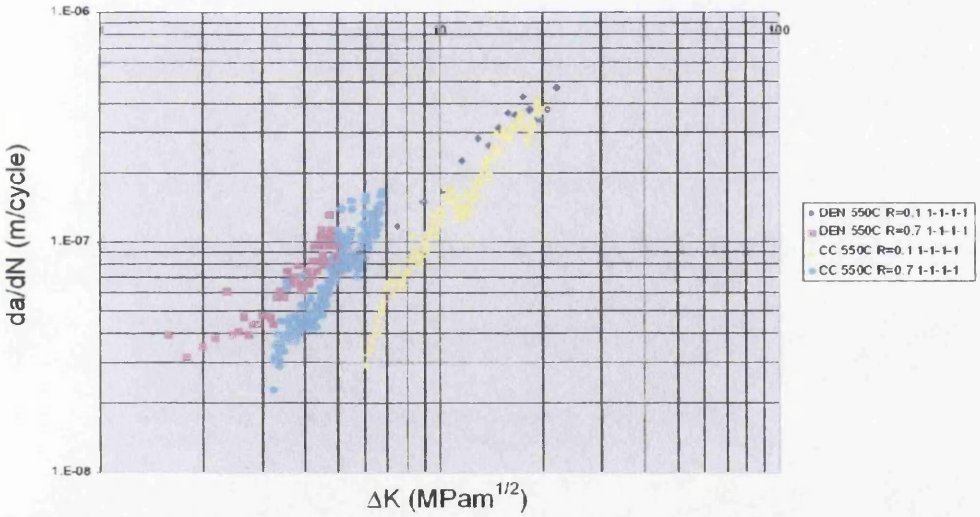


**Figure 5.50– Comparison of plane corner crack and DEN crack propagation tests at 550°C.**

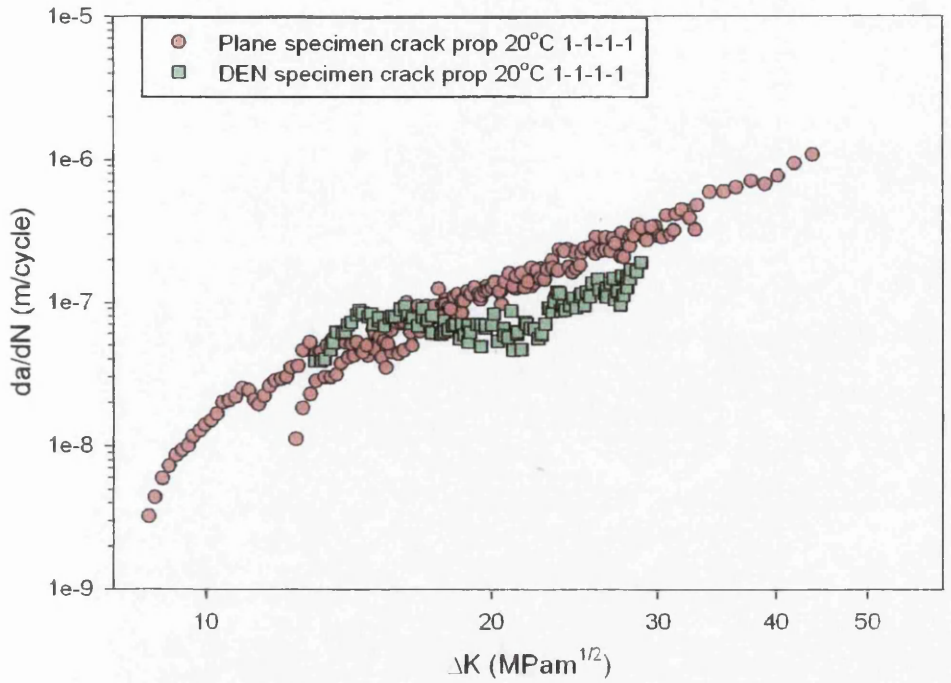


**Figure 5.51 – Comparison of plane corner crack and DEN crack propagation tests at 20°C**

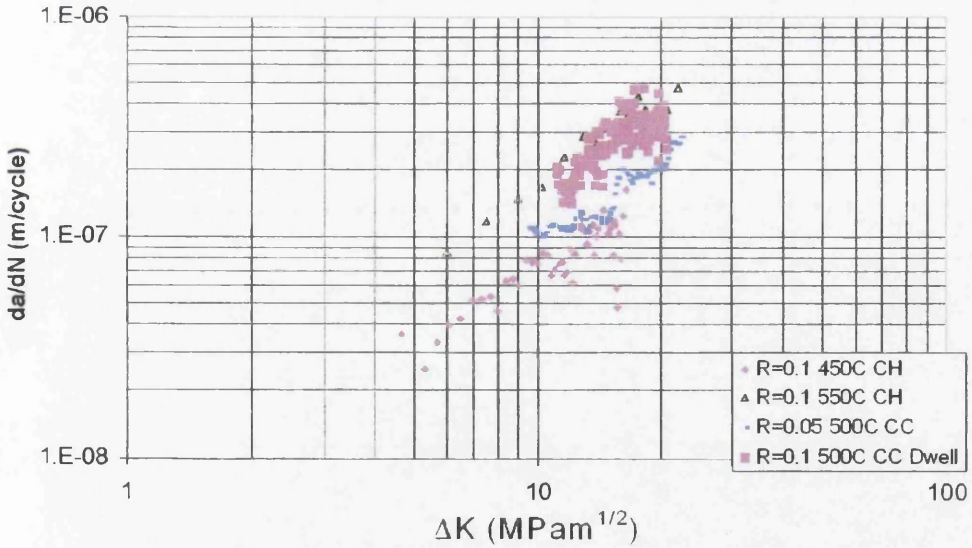


**Figure 5.52 – Comparison of DEN crack propagation tests**

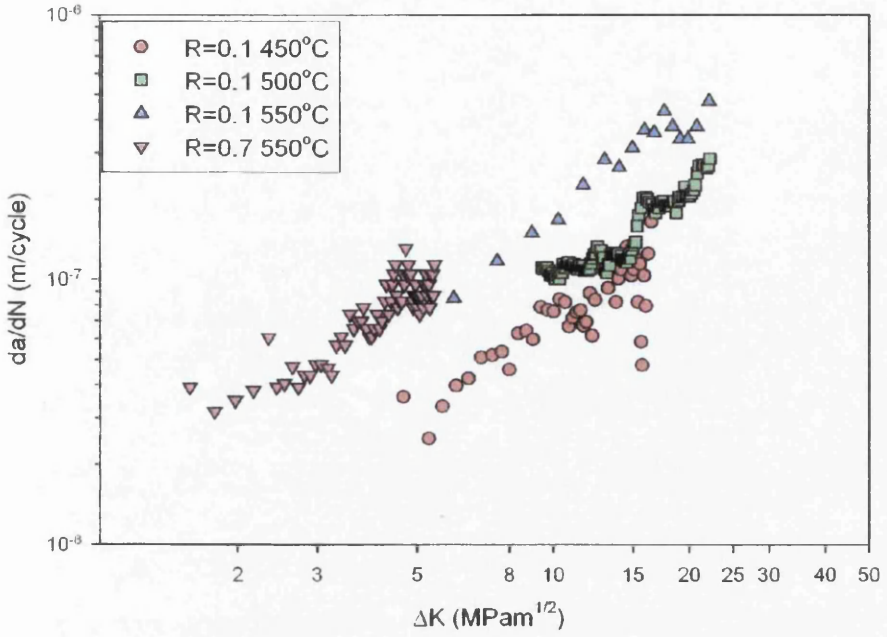


**Figure 5.53 – Comparison of DEN crack propagation data.**

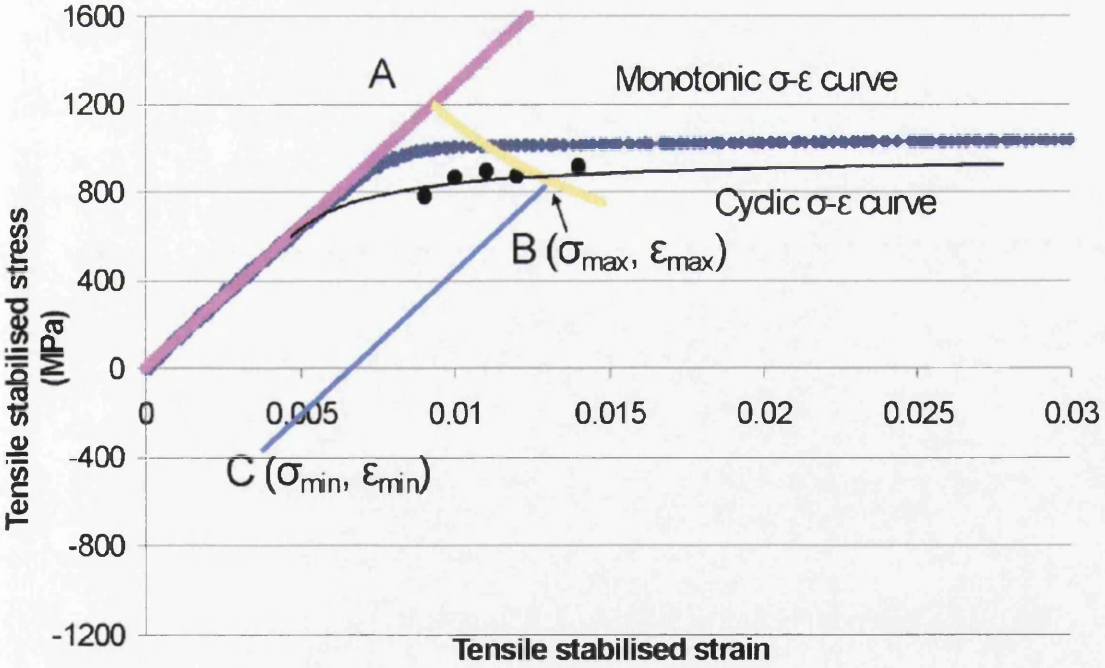


**Figure 5.54 – Notch root description, using Neuber redistribution method.**

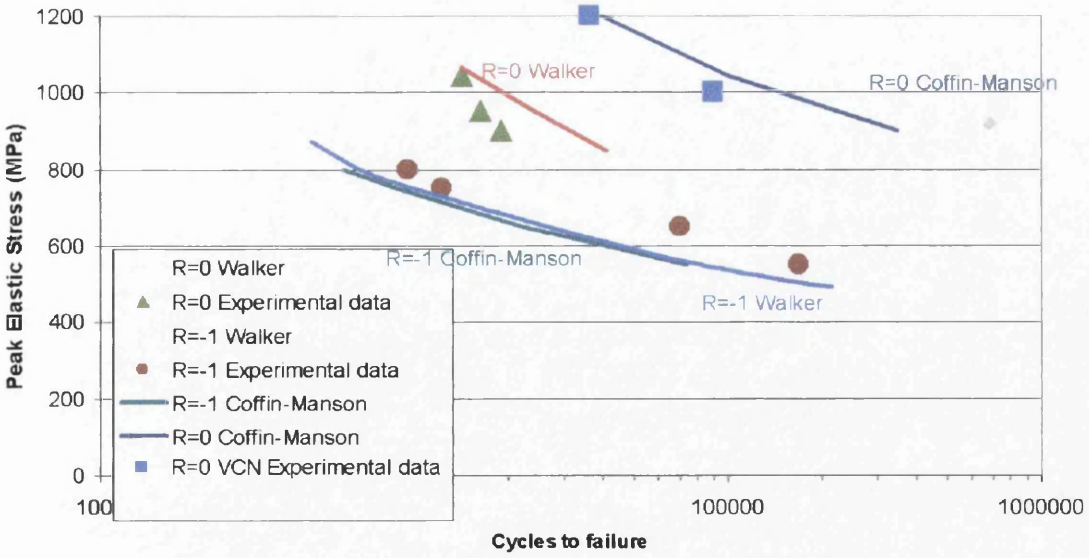


**Figure 5.55 – Comparison of notch prediction methods at 20°C.**

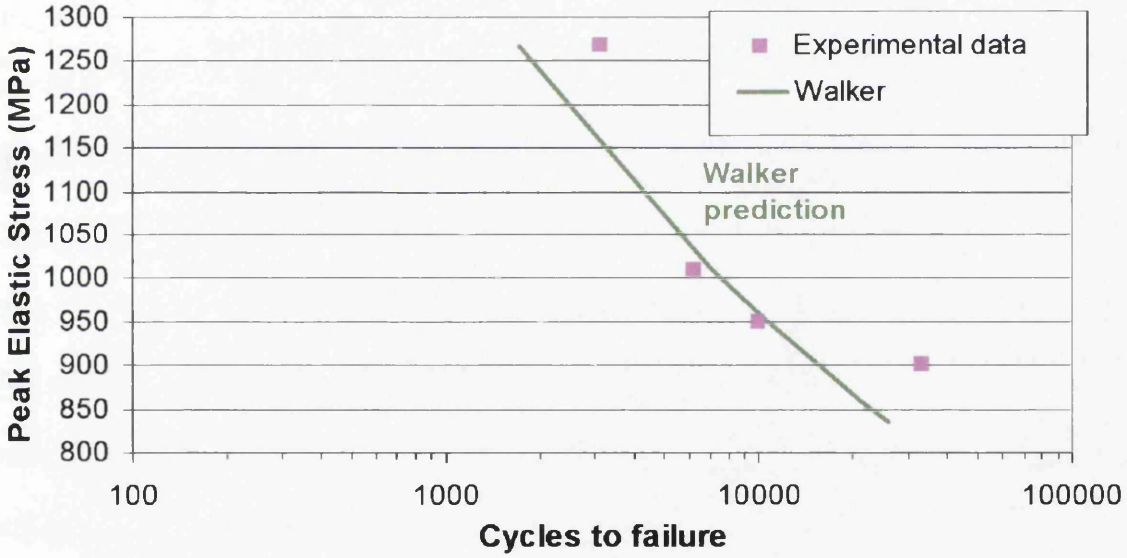


**Figure 5.56 - Comparison of notch prediction methods at 450°C**

# 6.0 DISCUSSION

## 6.1 STRAIN CONTROL

### 6.1.1 Temperature

As stated in the previous chapter the high temperature cyclic fatigue behaviour of Ti6246 was assessed by testing at a range of temperatures from 20°C to 550°C.

The general trend seen during strain control testing on plain specimens was that of cyclic softening at room temperature (Figure 5.2), which then transitioned through a state where neither cyclic softening or hardening was apparent at 300°C (Figure 5.4). The material then exhibited signs of cyclic hardening up to temperatures of 500°C (Figures 5.5 – 5.7) with hardening being greater at higher peak strains, while at 550°C the material once again shows signs of softening (Figure 5.8). The softening seen at room temperatures is likely due to the redistribution of dislocations as the material is cycled, while the cyclic hardening seen at higher temperatures indicates that dislocation recovery occurs prior to the beginning of testing while the specimen is being saturated at the test temperature. At 550°C, kinematic softening can be attributed to creep effects. It is argued that the cyclic softening response at ambient temperatures is due to inhomogeneities in the alloy microstructure, which in this case are the different properties of primary alpha and transformed beta phases in bimodal structures *(Lutjering 1998).*

As temperature increases a decrease in modulus and yield stress is evident, with the drop being most apparent between 20°C and 300°C. At greater peak strains the substantial difference between maximum stress at 20°C and the high temperatures

becomes more pronounced. At greater peak strains widening of the loops and bowing effect in compression (Bauschinger effect) become apparent.

By comparing the initial (Figures 5.10 –5.11) and stabilised loops (Figures 5.14 & 5.15) the large amount of stress relaxation at 20°C is evident, in comparison to the higher temperatures. This corresponds to the data seen in Figure 5.2. The stress relaxation is also reflected in the normalized stress vs cycles plots and is likely due to the lack of dislocation recovery at room temperature.

The effect of elevated temperature on fatigue life is clear from Figure 5.19, with the drop in fatigue life from 20°C to 300°C being greater than the range of fatigue life from 300°C to 550°C. It is therefore reasonable to assume that the stress relaxation seen at 20°C is a major factor in determining the fatigue life of strain control tests. The cyclic hardening seen at elevated temperatures must also be contributing the materials decreasing fatigue performance. At 550°C however, the benefits of cyclic softening are clearly being negated by creep effects (with creep damage ahead of the crack tip shown in Figure 6.1), which cause damage that will accelerate the fatigue process.

Also worth noting here is the steep gradient of the fatigue curve at high temperatures up to $10^4$ lives, which then becomes shallow at longer lives. This trend is not exhibited in the 20°C curve, indicating a change in failure mechanism at high temperatures. This has been shown to be the result of oxide cracking by Mailly (*Mailly 1999*), which shall be discussed in a later section.

Figure 5.20 helps to highlight effect of strain range on strain control lives, with differences in temperature at strain ranges of 2 and 3% having little effect on fatigue life. At strain ranges of 1%, temperature has a marked effect on fatigue life, possibly the result of scatter. It is also interesting to note that at these lower strain ranges, a small change in strain results in a substantial difference in fatigue life. These trends indicate that the fatigue life of the material is dependent on strain level at strain ranges of 2% and above, with this dependence decreasing below 1% as the alloy transitions from elastic to plastic deformation.

All strain control fracture surfaces were taken from R= -1, 1% peak strain tests, for a direct comparison. Figures 6.2 to 6.5 show overviews of the fracture surfaces of strain control specimens tested cyclically at 20, 450, 500 and 550°C respectively. One of the most notable differences is when comparing the 20°C fracture surface to the high temperature fractures. The 20°C specimen has a comparatively featureless fracture surface topography with multiple initiation sites around the circumference, where it is difficult to distinguish the fatigue crack propagation portion of the surface from that of final failure. This is not the case with the high temperature specimens however. At these temperatures, the fatigue fracture is clear, with multiple initiation points being visible.

Views of the specimen gauge lengths are shown in Figures 6.6 to 6.9 at temperatures of 20, 450, 500 and 550°C respectively. A comparison of these images makes the effect of temperature on fatigue initiation clear. At 20°C there is no surface damage visible aside from that of the main fracture site. At elevated temperatures multiple surface cracks are visible, which is particularly apparent at 450°C. Further

increases in temperature do not necessarily result in greater numbers of surface cracks, and therefore initiation sites. Instead, it can be seen that these surface cracks are longer and contain small areas where the crack is almost parallel to the loading direction. This is particularly clear in Figure 6.9. This indicates that these large cracks consist of multiple initiation sites, which have propagated as independent cracks, and then merged through shear to become larger, single crack propagation fronts. This suggests either an increased crack propagation rate at high temperature, or a shorter life to initiation, thus allowing more time for the crack to propagate at the same rate.

A more detailed comparison of the fatigue fracture surfaces highlights the increase in damage as temperature elevates. At 20°C (Figure 6.14) an uninterrupted fracture surface is presented with no visible sub-surface damage. Figure 6.15 shows the fracture surface of the 450°C specimen, where minimal creep and environmental damage is evident. This is expected of Ti6246 at this temperature since creep effects do not generally become severe until 470°C (*Lesterlin 1995*)

The increase in damage at 500°C can be seen in Figure 6.16, with extensive sub-surface cracking normal to the crack propagation direction. Worth noting is the detail shown in Figure 6.17. This is the area of the crack that propagated at 45° to the applied stress, which was attributed to final failure. Here however, the surface has a striation-like appearance.

At 550°C, the severity of the sub-surface cracking is even greater, as shown in Figure 6.18. What is also notable at this temperature is the secondary cracking of the

fracture surface, originating from the specimen surface (Figure 6.19). This relates directly to the surface damage seen in Figure 6.9.

The effects of creep and environment on Ti6246 have been recognised in the high temperature data from the previous section. In order to thoroughly distinguish these creep effects, dwell tests were conducted under strain control.

### 6.1.2 Strain Control - Dwell

Dwell tests were conducted at 450, 500 and 550°C at a peak strain of 1% and R= -1, in order to show the varying effects of creep.

The results for the unbalanced 2 minute dwell tests showed that the decrease in stress during the hold at peak strain becomes more severe as temperature increases (Figures 5.21 – 5.24), likely due to the effects of creep. In the stabilised condition, the tensile mean stress at 450°C indicates a slight amount of cyclic hardening at 450°C, which was also seen in the cyclic tests at 400°C and 450°C. At 500°C and 550°C the shift of the mean stress into compression is due to creep in the tensile part of the cycle.

The comparison of balanced and unbalanced tests at 550°C showed that the shift in mean stress seen in the unbalanced test was not reflected in the balanced test, where the mean stress remains at approximately zero. In combination with the stress relaxation seen in both tension and compression in the balanced test, it can be surmised that there is a level of reversibility of the creep damage in this type of test.

The S-N curve comparing both balanced and unbalanced dwell data with cyclic data of the same temperatures is presented in Figure 5.28. It indicates that dwell has a negligible effect on the fatigue life in this type of test. In relation to this observation, it is worth noting that all strain control dwell tests were conducted at a strain range of 2%, placing them in the strain dependent regime, observed during cyclic testing (shown in Figure 6.10). Therefore the effects of dwell at strain ranges of 1% and below may present a different response.

A similar effect was seen in testing of Ti6246 with R = 0 at 500°C, with a 2 minute dwell by Evans et al (*Evans, Jones & Williams 2005*), where the unaffected fatigue life of the dwell tests were attributed to a greater level of stress relaxation during the dwell periods, thus offsetting the effects of any damage due to strain accumulation.

This corresponds with the data shown in Figures 6.11, 6.12 and 6.13, which compare the stabilised loop for cyclic and dwell tests at 450, 500 and 550°C respectively. At 450°C the dwell period exhibits a small amount of stress relaxation at peak strain, which has very little effect on the stabilised loop, confirming that creep is having a minimal effect at this temperature. At 500°C the stress relaxation (due to creep) during the dwell period (also shown in Figure 5.24) at peak strain in tension results in the reduction of the peak and mean stress, but has no overall effect on the stabilised stress range. The same effect is seen with more severity in the unbalanced 550°C.

The balanced dwell test (2 minutes at tensile and compressive peak strain) provides a clearer comparison with the cyclic loop. Though the stress relaxation due to creep at maximum and minimum strain is clearly visible, it is apparent that the peak stresses in tension and compression are virtually identical for both conditions. This can be attributed to the fact that these strain control tests were carried out at an R = -1. This suggests that while stress relaxation offsets the creep damage that occurs during the unbalanced dwell period, the balanced dwell relies on reversal of creep damage in compression for the same effect.

It is interesting to look at the dwell results on the $\Delta\varepsilon - N_f$ plot (Figure 6.10) in more detail. It indicates that for a given strain range dwell has a beneficial effect on fatigue life at 450°C and to a lesser extent at 500°C, while at 550°C the dwell has a detrimental effect. When compared with the $\Delta\sigma - N_f$ plot (Figure 5.28), the increase in life at 450 and 500°C relates to a decrease in stabilised stress range, while the opposite is true at 550°C. This indicates that dwell is having a net benefit effect on fatigue life up to 500°C, while having a detrimental effect at higher temperatures. This agrees with the notch fatigue data shown in Figure 5.30, where the dwell period at 550°C has a greater effect on life than the 500°C dwell period at higher stresses, indicating that at this temperature, creep is more damaging than beneficial.

Due to the small differences in fatigue life accorded to dwell, these trends may be attributed to scatter. The likelihood of this is reduced however, when compared with trends seen in the notched load control data generated as part of this programme.

### 6.1.2.1 Dwell Fractography

An overview of the fracture surfaces of the 2 minute unbalanced dwell at 450 and 550°C are shown in Figures 6.20 and 6.22. The equivalent 500°C specimen failed due to a 10% drop in stress from the stabilised condition, with the test being stopped before complete fracture, therefore no fracture surface is available. Instead a view of the gauge length is presented in Figure 6.21. The fracture surface of the 2 minute balanced dwell test is shown in Figure 6.23. Comparing these fracture surfaces with those of the cyclic tests at the equivalent temperatures shows similar fracture topographies, with multiple initiation sites around the circumference. This observation reinforces the fact that dwell has a small effect on fatigue life in comparison with cyclic tests at this strain level.

The effects of creep and environment on the specimens are more apparent when looking at the gauge length of the specimens. These are shown for the unbalanced tests in Figures 6.24 to 6.26 at 450, 500 and 550°C respectively. The balanced specimen is shown in Figure 6.27. Multiple surface cracks are visible at all temperatures, though the damage is more severe at 550°C, compared to 450°C. This surface damage is also clear at 500°C in Figure 6.21, and in more detail in Figure 6.25

When looked at in detail (Figures 6.28 – 6.31) for unbalanced dwell at 450, 500 and 550°C and balanced 550°C), the dwell fracture surfaces compare well with the cyclic fracture surfaces, with sub-surface cracking normal to the crack propagation

direction becoming more severe as the temperature increases. Worth noting is the triple point intergranular fracture seen in Figure 6.29, indicating creep effects.

The effect of the surface damage on the fracture surface can be seen at 450°C in Figures 6.32. This is of interest since there is no equivalent surface damage at the same temperature in the cyclic tests. Figures 6.33 and Figure 6.34 show the underlying surface damage of the unbalanced and balanced tests at 550°C, which are also seen at the same temperature during cyclic tests.

## 6.2 PLAIN CRACK PROPAGATION

A dwell period was shown to have no effect on the crack growth rate of plain specimens at 20°C (Figure 5.46), while at 500°C dwell results in a significant increase in the crack propagation rate (Figure 5.47), suggesting this is the result of creep and environmental damage.

## 6.3 NOTCH FATIGUE

### 6.3.1 Load Control - Double Edge Notch (DEN) Fatigue Tests

The flexibility of load control testing allows for the contribution of creep and environment to fatigue at high temperatures to be separated into their individual components, through cyclic and dwell tests in air and vacuum.

To assess the effects of temperature on fatigue, cyclic fatigue tests were conducted at elevated temperatures (Figure 5.34) and resulted in longer fatigue lives at 500°C than 450°C for a given peak stress. Since it is assumed that the constrained

material at the notch root behaves in a similar manner to plain specimen tests in strain control, it is worthwhile to compare these results with strain control tests of the equivalent temperatures. The strain control dwell tests allow for a more detailed analysis of creep effects for a given temperature. It was shown that there was minimal stress relaxation during dwell periods at 450°C, with stress relaxation increasing as temperature increases (Figure 5.24). This increased stress relaxation results in lower peak stresses at the stabilised condition for 500°C, compared to 450°C (Figure 5.23). Therefore it is likely that the increased creep deformation around the notch root at 500°C results in sufficient stress relaxation that the peak stress at this temperature is lower than at 450°C. The larger accumulation of creep strain at the notch root and net section at 550°C leads to a significant reduction in life. Crack propagation tests conducted at this temperature failed away from the machined notch resulting in net section stress rupture, showing the effects of creep at 550°C.

An overview of the fracture surface of a 20°C specimen is shown in Figure 6.56. Only two main initiation sites are visible, with a small crack propagation area surrounding them. As with the 20°C strain control tests, the fracture surface (Figure 6.57) exhibits no sub-surface damage, which is consistent with a lack of creep damage. The 450°C fracture surface presents all the hallmarks of an elevated temperature test in air, with multiple initiation sites at both notch edges (Figure 6.35 and 6.36) and sub-surface damage. At 500°C the type and level of sub-surface damage seen on the fracture surface (Figure 6.47) is equivalent to that seen at 450°C, with a similar number of surface initiation sites at both temperatures. This sits well with the test data since the observed fracture surfaces come from tests with peak elastic stresses of 1268MPa (450°C) and 1120MPa (500°C), which resulted in similar lives.

The further reduction in life for a given peak stress at 550°C is not only reflected in the additional sub-surface cracking perpendicular the direction of crack propagation (Figure 6.43), but also in the damage seen to originate from surface cracks (Figure 6.42).

### 6.3.2 Vacuum Tests

The effects of creep on Ti6246 at 450°C are minimal, therefore the air and vacuum tests at this temperature (Figure 5.29) provide a good example of the effects of environment on fatigue life, with vacuum test lives being approximately an order of magnitude greater than that of air test lives. The comparison of 550°C air and vacuum data show a similar difference in life to the 450°C data. This indicates that environment has a dominant effect on fatigue life at elevated temperatures. This is particularly true at high peak stresses.

Figures 6.35 – 6.38 show the fracture surfaces of a DEN specimen tested in air at 450°C under a cyclic waveform with a peak stress of 1268MPa. Multiple initiation sites are visible on both edges of the notch, with sub surface cracking visible on the fracture surface. Also note the striations on the fracture surface.

The fracture surfaces shown in Figures 6.39 and 6.40 show the fracture surface of a specimen tested at 450°C under a cyclic waveform at a peak strain of 1010MPa in vacuum. Under these test conditions the main crack propagates from a single initiation point, while sub-surface cracking and striations are absent from the fracture surface. With creep effects being minimal at 450°C and similar peak stresses being compared in air and vacuum, the multiple initiation sites and sub-surface cracking seen in the air

test can be largely attributed to environmental effects. This indicates that environment plays a dominant role in the crack initiation stage and also contributes to damage during crack propagation.

The trends that differentiate the air and vacuum fatigue fracture characteristics at 450°C are echoed in the 550°C fractography data, with the vacuum test resulting in a single initiation site (Figure 6.46) and little sub-surface damage. The air test results in multiple initiation sites (Figure 6.41) and extensive sub-surface cracking, both perpendicular to the crack propagation direction (Figure 6.43) and cracks originating from surface damage (Figure 6.42). When comparing vacuum tests at 450°C and 550°C in vacuum the only notable difference is a slight increase in the severity of sub-surface fracture. From this, it can be suggested that the level of creep damage accumulated during cyclic testing is not the dominant factor for fatigue life at high peak stresses (ranging from 1010 – 1120MPa).

### 6.3.3 Load Control DEN Dwell

The comparison of notch cyclic and dwell fatigue tests at 500 and 550°C (Figure 5.30) show that the 2 minute dwell period resulted in a significant decrease in life for a given peak stress, indicating that the interaction of creep and the environment has a detrimental effect at these temperatures, with creep damage ahead of the crack tip one of the most likely reasons for this drop in life (*Ford 2002)*. The results of the strain control dwell tests raised the question as to whether the creep effects are beneficial to the life of the notched specimens by reducing the stresses at the notch root, but this data seems to indicate that it has been outweighed by the damage the creep is doing at 550°C.

This conclusion appears incomplete however. When the strain and load control dwell data is compared on the same plot (Figure 5.31), where the load control data is plotted on a peak elastic stress basis and the strain control data on a stabilised stress range basis, a pattern emerges. As stress increases, dwell test lives and cyclic test lives converge, becoming virtually indistinguishable above 1000MPa, suggesting that fatigue is the dominant factor at high peak stresses. This stress level corresponds with the transition level seen in the strain control tests (Figure 5.20 or Figure 5.28), above which fatigue life becomes strain dependent, which in turn reflects the transition from elastic to plastic deformation. It can be seen in Figure 5.29 that vacuum tests do not show the same transition seen in air tests. This suggests that plastic deformation at these stresses results in surface oxide cracking, which allows ingress of the environment to the material surface, aiding initiation and crack propagation.

At a peak stress of 1120MPa the 2 minute dwell period at 500°C has very little effect on fatigue life (Figure 5.30). This is reflected in observations of the fracture surfaces where there does not appear to be a substantial difference in the number of initiation sites, or any major surface damage away from the main fracture plane (Figures 6.47 and 6.49). However, sub-surface damage does appear to be more severe in the dwell specimen (Figure 6.50) compared to the cyclic test (Figure 6.48). Since comparisons of vacuum and air test fracture surfaces have shown that sub-surface cracking can be largely attributed to environmental effects, this increased severity suggests the dwell period allows greater time for environmental ingress leading to greater material damage. At 550°C, where dwell and therefore creep have a major effect on fatigue life (Figure 5.30), there is significantly more damage at the notch surface of the dwell test (Figure 6.51), compared to the cyclic test (Figure 6.41),

suggesting that creep is interacting with the environment, increasing fatigue crack initiation damage. This is reflected in a comparison of the 500°C and 550°C dwell data, where surface damage is greater at 550°C compared to 500°C.

#### 6.3.3.1 Vacuum

Previous figures have shown the extent of reduction in life cause by creep and environmental effects. Figure 5.32 compares cyclic and dwell tests in air and vacuum at 550°C, and shows the effect of the combined fatigue-creep-environment interaction at high temperatures. In this instance the 550°C cyclic data in vacuum may be treated as a baseline for the creep and environment effects at high temperature since the vacuum negates the environmental mechanisms and the 1 second hold time of the cyclic test results in comparatively less creep damage than the dwell tests. The effect of creep can be assessed, by comparing the baseline with the 550°C dwell data in vacuum. The environmental effect can be determined through comparison with the 550°C cyclic data in air. From this it can be seen that environmental effects account for a greater decrease in specimen life than creep effects. It is also worth noting that the dwell period in air results in a similar decrease in fatigue life to that caused by dwell in vacuum. This suggests that the effect of creep on fatigue life is unaffected by the environment. This complements the observations made of the cyclic data in Figure 5.29 which showed that creep does not affect the amount of damage caused by the environment. A comparison of the baseline data with the 550°C dwell data in air, show the combined effects of creep and environment. From this, it can be seen that the effect is cumulative, with this set of data having the shortest life of all test conditions at 550°C.

The cause of the environmental damage exhibited in Figure 5.32 is a continuing subject of discussion. Some have attributed the damage to water vapour, while others have indicated the ingress and diffusion of oxygen as a possible cause *(Ghonem & Foerch, 1991) (Foerch, Madsen & Ghonem 1993).*

The water vapour model, forwarded by Petit *(Petit 1992,) (Lesterlin, Sarrazin-Baudoux & Petit 1995)* account for crack growth rate differences in air and vacuum suggests there is a critical growth rate $(da/dN)_{cr}$ , which is dependent on material and test condition. This critical value is reached when the crack tip plastic zone is equal to the alloy grain size. When crack growth rate is greater than this value, it advances normally, but at a higher rate due to water vapour adsorption. At rates below the critical value, there is time for water to dissociate, leaving the hydrogen to cause increases in crack growth rate. This model has been further promoted by the recent work of Sarrazin-Baudoux (*Sarrazin-Baudoux, 2005*) and Henaff et al (*Henaff, 2007*) whose research has shown a predominant detrimental effect of water vapour, even under very low partial pressure.

## 6.4 DEN - INITIATION

Though the free initiation data gathered from measurements across the notch root is not highly accurate due to the bulk of material over which the potential difference is recorded, some general trends were observed.

### 6.4.1 Temperature

A comparison of initiation lives at 500°C (Figure 5.42) and 550°C (Figure 5.40) show that temperature has little effect, with both specimens reaching the detection threshold of 2.19mm at approximately 4000 cycles. To see if the transition at 1000MPa has any influence on initiation life it is worth comparing a 750MPa test (Figure 5.38) with a 1120MPa test (Figure 5.41). The results show that initiation, as a proportion of total fatigue life is greater for the lower peak stress. This reinforces previous observations where the damage mechanism in tests greater than approximately 1000MPa has been attributed to oxide cracking. This would encourage surface initiation through environmental ingress, leading to the shorter initiation life seen here.

### 6.4.2. Dwell

To determine whether the dwell effect on fatigue life in the elastic response region is linked to initiation life, it is necessary to compare the initiation data of cyclic and dwell specimens tested below the 1000MPa peak stress threshold. While strain control tests spend up to 95% of their life at the initiation stage the results presented in Figures 5.40 and Figure 5.43, show that crack growth to 2.19mm accounts for approximately 80 - 90% of the fatigue life of the cyclic and dwell tests.

Figures 6.47 shows the fracture surfaces of the specimens tested with a cyclic waveform at 500 and 550°C respectively, while Figures 6.49 and 6.51 show the equivalent fracture surfaces tested with a 2 minute dwell. All specimens were tested at a peak strain of approximately 1120MPa. Multiple initiation points along the notch

root can be seen in all specimens. The effect of the dwell period at 500°C can be clearly seen in the form of surface damage in Figure 6.49. The severity of this surface damage increases dramatically at 550°C. Since the surface damage from multiple initiation sites are not seen during vacuum testing, it can be taken that environmental damage is creating favourable conditions for crack initiation, which are greatly enhanced by the 2 minute dwell period as temperature increases. This suggests an interaction between creep and the environment, which enhances surface initiation.

### 6.4.3 Elevated temperature fatigue

The plot in Figure 5.33 presents a comparison of all the DEN fatigue tests during this programme. The overall trend when comparing all the data is that of a distinct transition of the fatigue curve of air tests from a steep gradient to a shallow gradient below a stress of approximately 1000MPa, corresponding to a life of $10^4$ cycles. This transition is not seen in the vacuum data, which tends to show a more typical decrease in life with increasing stress.

This corroborates the work of Evans et al. (*Evans, Jones & Williams 2005*) who showed that at lives greater than $10^4$ cycles, the fatigue curve in air for Ti6246 transitions from a steep gradient to a shallow gradient, indicating a change in damage mechanism, which corresponded with the level of strain that equates to the onset of plastic deformation. At lives shorter than this transition, and therefore higher strain levels, multiple surface cracks were present, and when compared with vacuum data by Mailly (*Mailly 1999*), the transition was not present, indicating an environmental effect, which Mailly attributes to the lack of integrity of the oxide layer above the

transition strain allowing the ingress of the environment. Below the transition, they found that specimens did not fail, or propagated to failure from one major crack site.

The fracture surfaces of two specimens tested in air under a cyclic waveform at 550°C are shown in Figures 6.54 and 6.55, which were subjected to peak strains of 750MPa and 1119MPa respectively. At 750MPa a single point of initiation is present, while at 1119MPa there are multiple initiation sites on both notch edges, matching Mailly's observations.

### 6.4.4 Freely Initiated Tests

The P.D. monitored freely initiated notch tests were run to failure, allowing not only initiation data to be recorded, but also crack propagation data, providing information on the influence of temperature and dwell. The comparison of this data (Figure 5.44) presented some interesting results in that there was very little difference in crack growth rate between 500 and 550°C, with the only substantial difference occurring at lower $\Delta K$ values. A comparison of these three tests shows that peak stress is the dominant factor in this early stage of crack growth.

The effect of dwell however, is clear at these high temperatures, with the 2 minute dwell resulting in a substantial increase in crack growth rate compared to the equivalent cyclic test, highlighting the effect of creep and environment on crack growth rate.

### 6.4.5 DEN Crack Propagation

The results of DEN corner crack and centre hole crack propagation tests (Figure 5.52) reflect the freely initiated crack propagation results with the dwell period leading to a substantial increase in crack growth rate at a given ΔK at 500°C. Interestingly, the difference between the 500°C and 550°C crack growth rate is greater here, than the freely initiated tests. It is worth noting however, that this temperature difference also involves the comparison of a corner crack and centre hole DEN specimen, though the 500°C comparison in Figure 5.49 indicates that this has no effect on the crack propagation rate.

The relation of the DEN crack propagation data to the freely initiated DEN data (Figure 5.45) showed that the freely initiated crack tests start with a very low crack propagation rate at higher $\Delta K$'s compared to the crack propagation tests, reflecting the high peak stresses of the freely initiated tests. Though not conclusive, it appears that the two sets of data may converge. If this were the case, it would indicate the point at which the freely initiated DEN tests show the same behaviour as the crack propagation DEN tests, suggesting this is the point at which the crack escapes the large plastic zone around the notch root and behaves like a typical crack propagation test.

The DEN notch geometry was shown to have no effect on crack propagation rate at 20°C (Figure 5.51), so to assess how the DEN notch geometry affects fatigue crack propagation at elevated temperatures, a comparison with plain crack propagation specimens is needed. This is presented in Figure 5.50. Though the difference in crack propagation rates is small, their divergence at lower $\Delta K$

approaching the threshold condition suggests that creep and environment effects are occurring close to the notch root or the plastic zone around the notch root is having a substantial effect.

Mean stress effects on crack propagation are also presented in Figure 5.50, with an increase in R ratio resulting in a substantial increase in crack propagation rate, indicating a strong dependence on mean stress. This behaviour can be attributed to time dependent creep deformation, with the high mean stress allowing static creep deformation and damage to occur and environmentally assisted crack growth due to the crack remaining open for a greater proportion of the loading-unloading cycle, allowing the environment to access the crack tip.

## 6.5 V CYLINDRICAL NOTCH (VCN) TESTS

The S-N curve of VCN fatigue data (Figure 5.35) exhibits a significant drop in fatigue life between 20°C and 450°C, which is also reflected in the strain control data conducted during this programme. It is also worth noting that the expected drop in fatigue life from 450°C to 500°C is present, unlike the DEN tests. This is likely due to the differing specimen geometries affecting the levels of stress relaxation at these temperatures.

Fracture surface images of VCN specimens were taken at a peak stress of 1000MPa. At 20°C (Figure 6.58) a single initiation site is visible with the crack propagating (bottom to top) from this point to final failure. At 450 and 500°C (Figures 6.57 and 6.60) multiple initiation sites are present, though final failure still occurs at the specimen surface. Only at 550°C do the multiple initiation sites result in final

failure occurring at a sub-surface location. It is clear from these results that increasing temperature leads to an increase in the number of initiation sites, which in turn contributes to a decrease in fatigue life. This is consistent with the other specimen geometries tested in air during this programme and can therefore be related to environmental damage

The effect of high temperatures on the crack propagation stage of VCN tests can be seen in the relevant fractographs. At 20°C the fracture surface appears intact (Figure 6.62), while at 450°C some sub-surface damage appears. This damage becomes more severe as temperature increases, as shown in Figures 6.64 for 500°C and Figures 6.65 and 6.66 for 550°C.

### 6.5.1 Stress Concentrations Effects

Certain comparisons have been made between plain and double-edged notched specimen data in previous sections, which mostly involved the use of strain control deformation data to help define the effects of temperature and dwell on DEN tests. Analysis of VCN test data and fracture surfaces has been used to reinforce observations made of plain and DEN data. In order to assess the overall effects of the specimen geometries on fatigue life, direct comparisons of these geometries are required.

A comparison of DEN and VCN S – N data (Figure 5.36) allows the effect of different $K_t$ values on fatigue life to be evaluated. In previous sections the main differences highlighted were longer lives at 500°C compared to 450°C in the DEN data, attributed to creep effects at the notch root of the 500°C tests. This was a trend

not seen in the VCN data. When compared on the same axes however, the general correlation of the two sets of data at a given temperature can be seen reflecting a similarity in the behaviour at the notch root. This is interesting since the stress field imposed by the VCN notch is smaller than that of the DEN specimen, making it less likely that there will be a weak link within the stress field. This tends to result in longer lives for VCN tests.

Of particular interest is a comparison of plain and notched specimen geometries. For clarity, DEN and VCN data is compared with plain specimen strain control data on separate axes, shown in Figures 6.67 and 5.36 respectively. Both graphs are plotted on a stress range vs. life basis (stabilised stress range for strain control data). From this comparison a general trend is immediately apparent. At lives of approximately $10^4$ cycles and greater, there is a good correlation between the plain specimen strain control and notched load control data. At shorter lives (higher stresses) however, the strain and load control data diverges, with the strain control tests having significantly shorter lives for a given stress.

By referring back to the strain control deformation data (Figures 5.9 to 5.12) it can be seen that the correlation of strain and load control data relates to stress ranges where the material is exhibiting elastic behaviour. The point at which the plain and notched specimen data diverges relates to the onset of plastic deformation, which results in oxide cracking, allowing environmental ingress. Therefore, it is clear that this failure mechanism is resulting in greater damage to plain specimen geometries, than in notched specimens. A possible explanation for this may be because the stress field surrounding the notch, which represents the condition of the strain control

specimen, does not act on the bulk of the notched specimen material. For the notched specimens, this could result in less environmental damage once the fatigue crack has transitioned from the notch stress field, into the bulk of the specimen, where stresses are lower. This would not be the case for the strain control tests, where the stress over the cross-section of the specimen is constant, and would therefore not lead to a reduction in environmental damage.

It is worth noting however, that due to scatter, it is difficult to determine the behaviour of the 20°C VCN data. Without further VCN testing at higher peak stresses it is unclear whether this data matches the trend seen in the elevated temperature VCN data, or that of the 20°C strain control data, though the Coffin-Manson prediction with R= 0 VCN data suggests that there is a correlation between the 20°C strain control and notched specimen data.

### 6.5.2 Prediction of Notched Specimen Behaviour

Though the Coffin-Manson method resulted in a good correlation with R= -1 DEN data, R= 0 predictions overestimated the corresponding experimental data (Figure 5.55). This is likely because the actual R= 0 tests still experience a mean tensile stress, despite plastic deformation at the notch root forcing unloading into compression. The Coffin-Manson method provides a good prediction since it is based on R= -1 strain control data and is therefore suitable for fully reversed loading at the notch root. This accounts for the correlation of predicted and experimental R= 0 VCN data indicating that the conditions at the notch root represent those of R= -1 strain control tests after an initial shakedown. These results also indicate that using the Neuber rule for stress/strain redistribution at the notch root leads to reasonable

predictions under certain conditions. The Walker strain method resulted in adequate predictions at 20°C for R= 0 and R= -1 and at 450°C for R= 0.

*Discussion*

*Appendix*

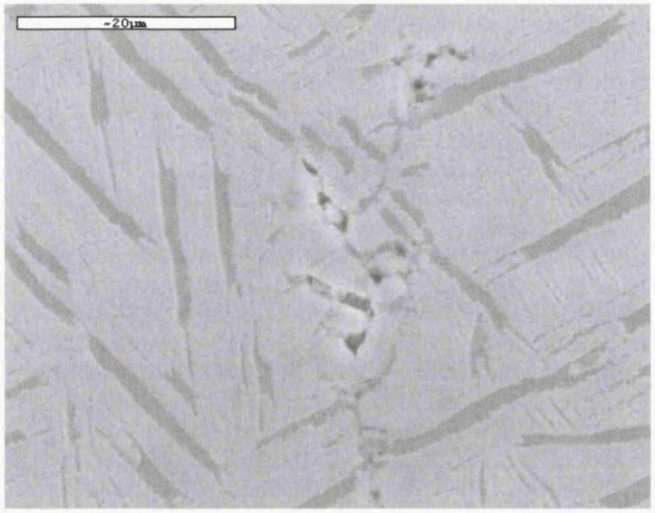


**Figure 6.1 - Voids ahead of the crack tip at 550°C**

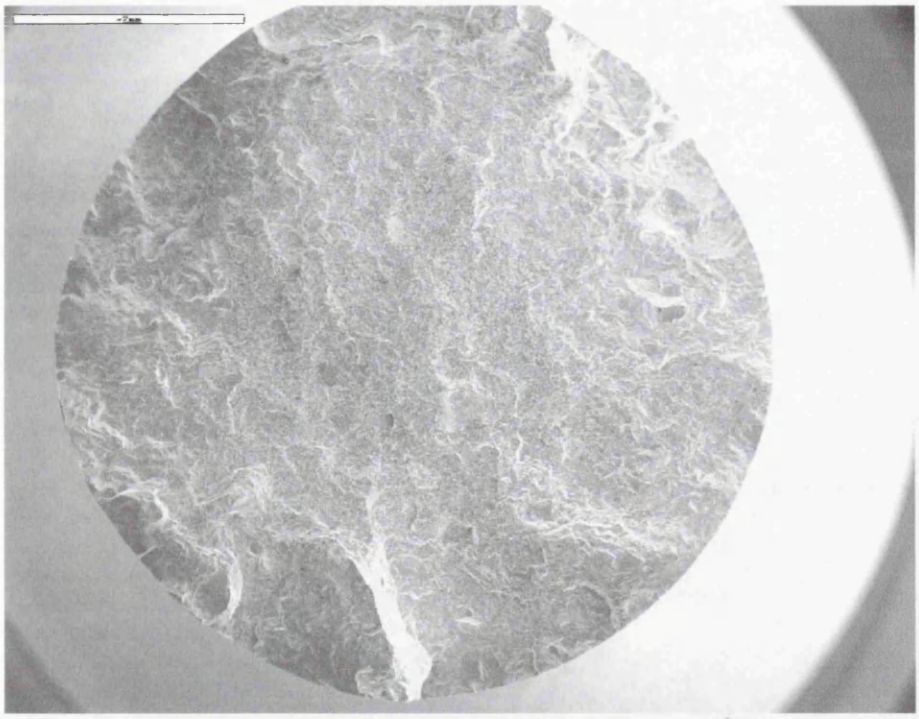

**Figure 6.2 – Overview of strain control fracture surface (20°C, cyclic waveform)**

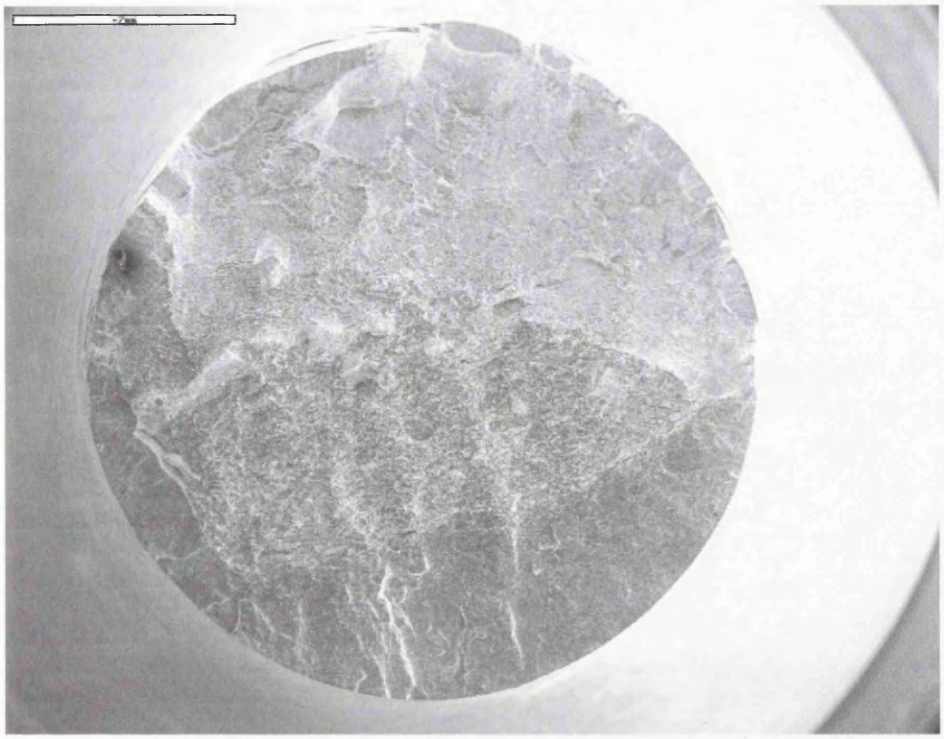

**Figure 6.3 - Overview of strain control fracture surface (450°C, cyclic waveform)**

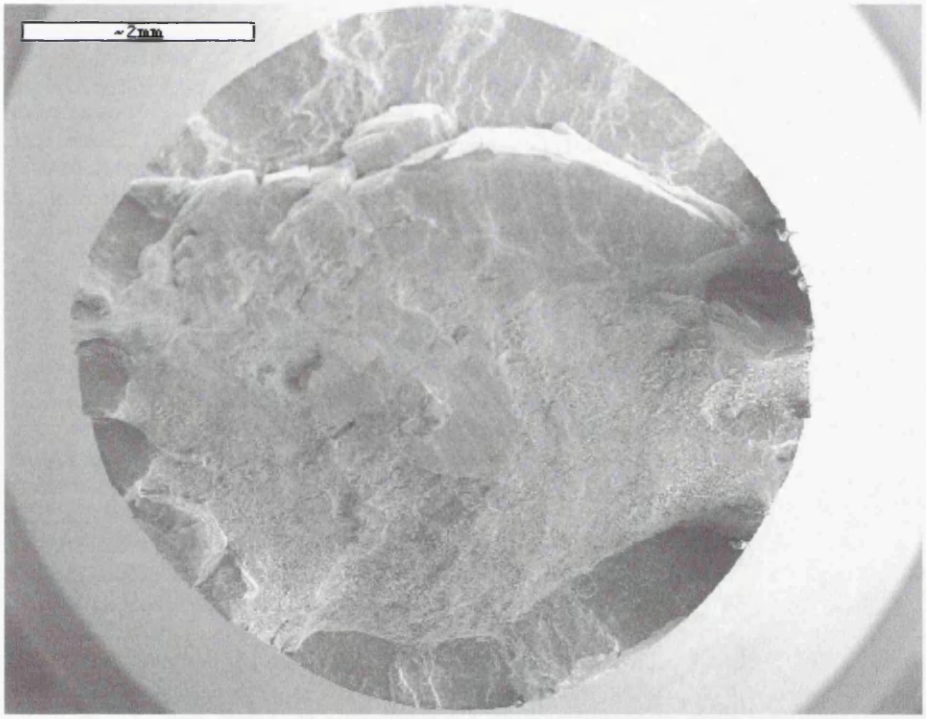


**Figure 6.4- Overview of strain control fracture surface (500°C, cyclic waveform)**

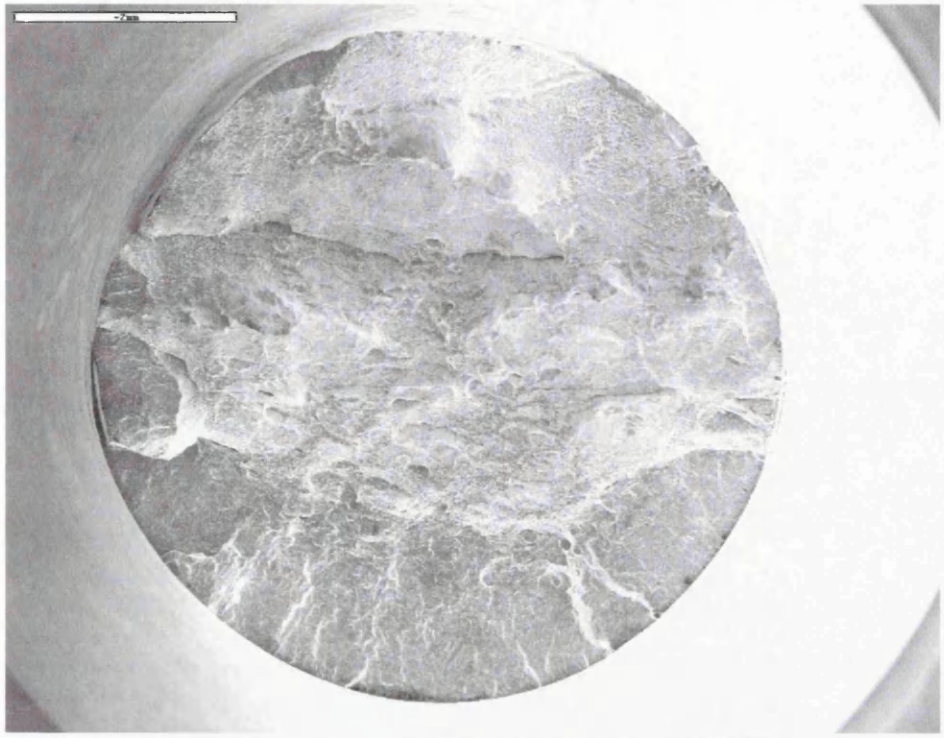

**Figure 6.5 - Overview of strain control fracture surface (550°C, cyclic waveform)**

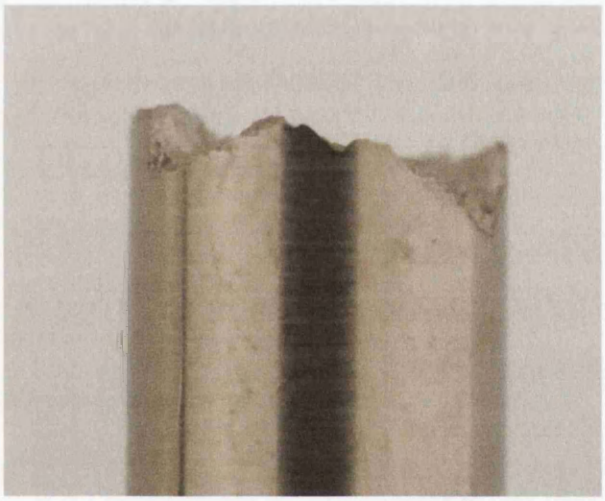

**Figure 6.6 - Strain control gauge length (20°C, cyclic waveform) with no surface cracking**

**Figure 6.7 - Strain control gauge length (450°C, cyclic waveform), with multiple surface cracks**

**Figure 6.8 - Strain control gauge length (500°C, cyclic waveform), with multiple surface cracks**

**Figure 6.9: Strain control gauge length (550°C, cyclic waveform), with multiple surface cracks**

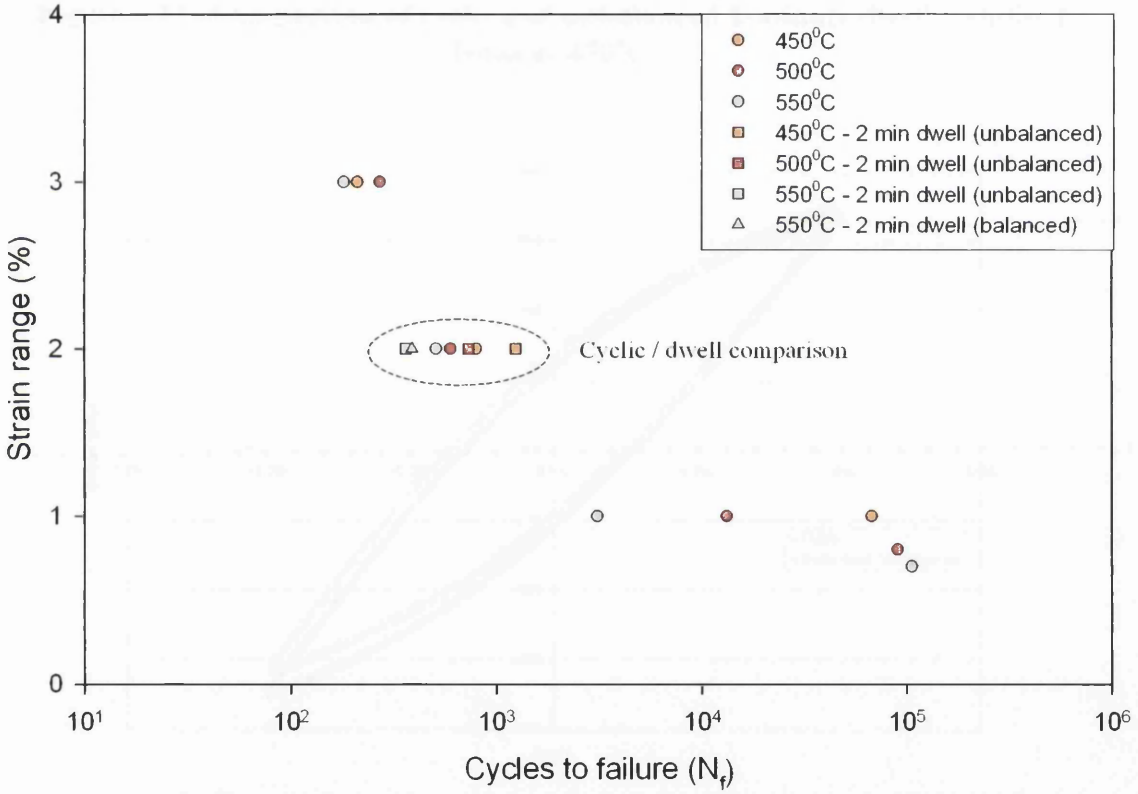


**Figure 6.10: Strain range – life comparison of dwell and cyclic tests**

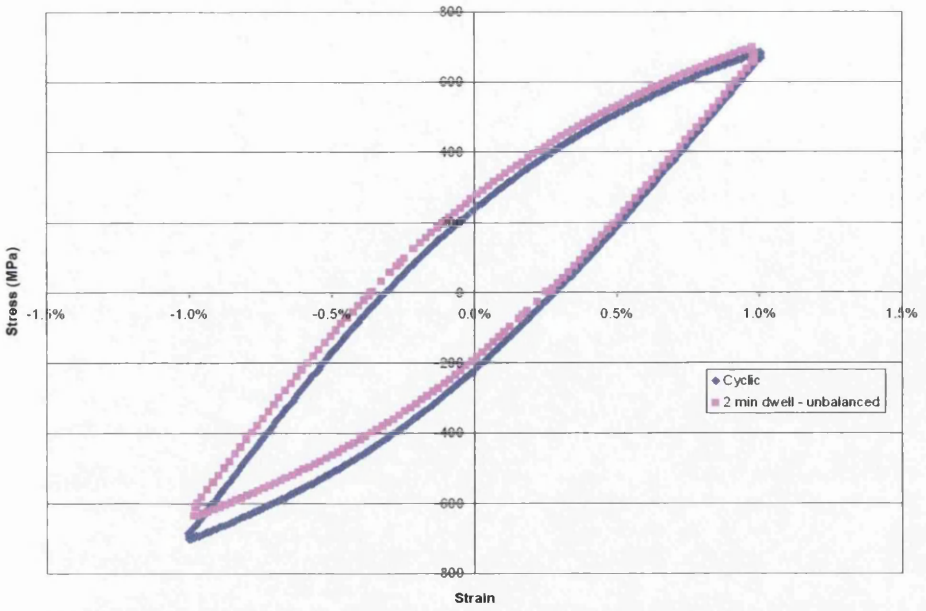


**Figure 6.11: Comparison of cyclic and unbalanced 2-minute dwell stabilised loops at 450°C**

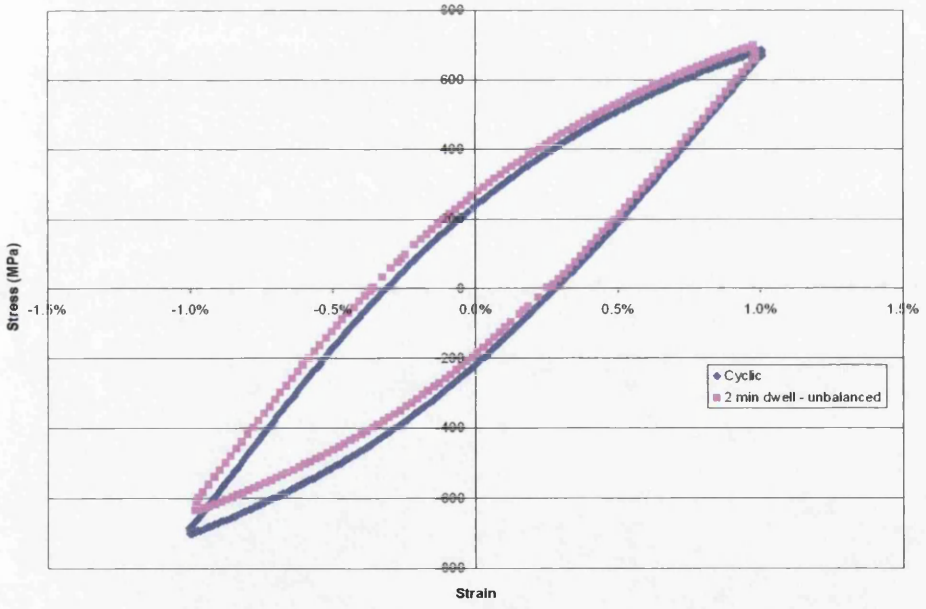


**Figure 6.12: Comparison of cyclic and unbalanced 2 minute dwell stabilised loops at 500°C**

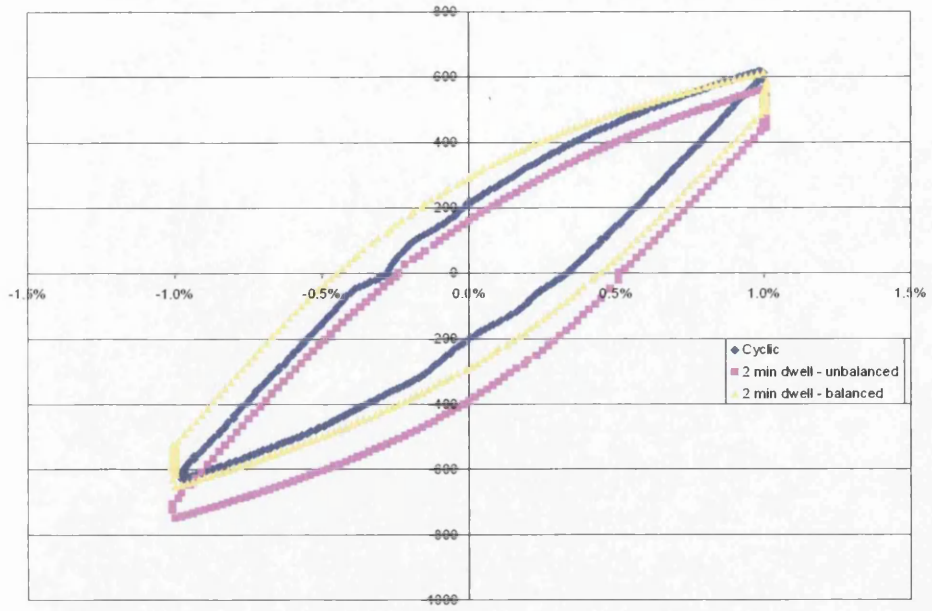


**Figure 6.13: Comparison of cyclic and balanced / unbalanced 2 minute dwell stabilised loops at 550°C**

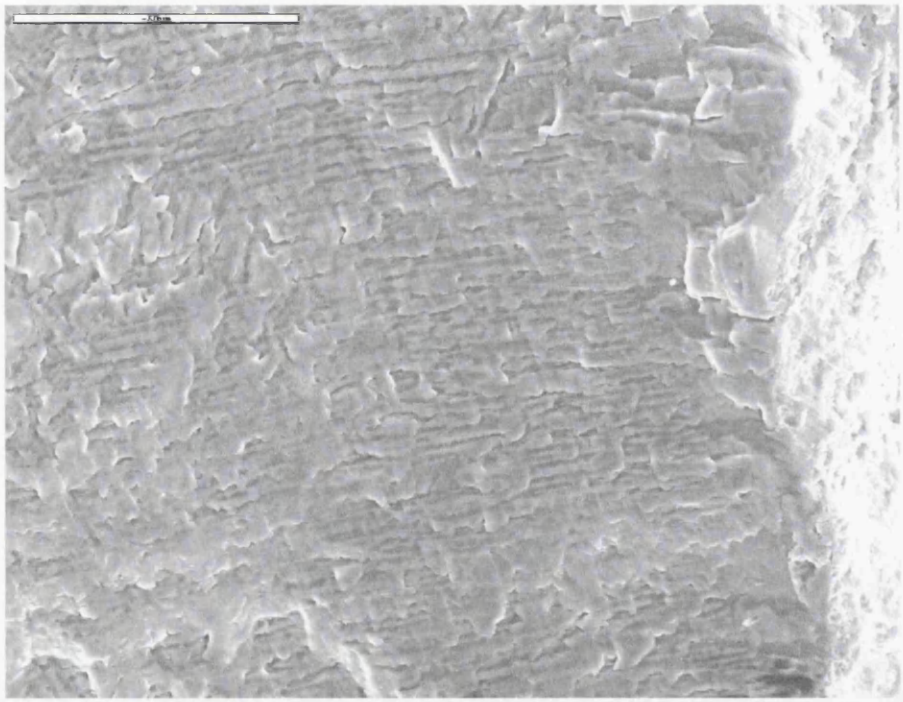

**Figure 6.14 - Strain control fracture surface (20°C, cyclic waveform)**

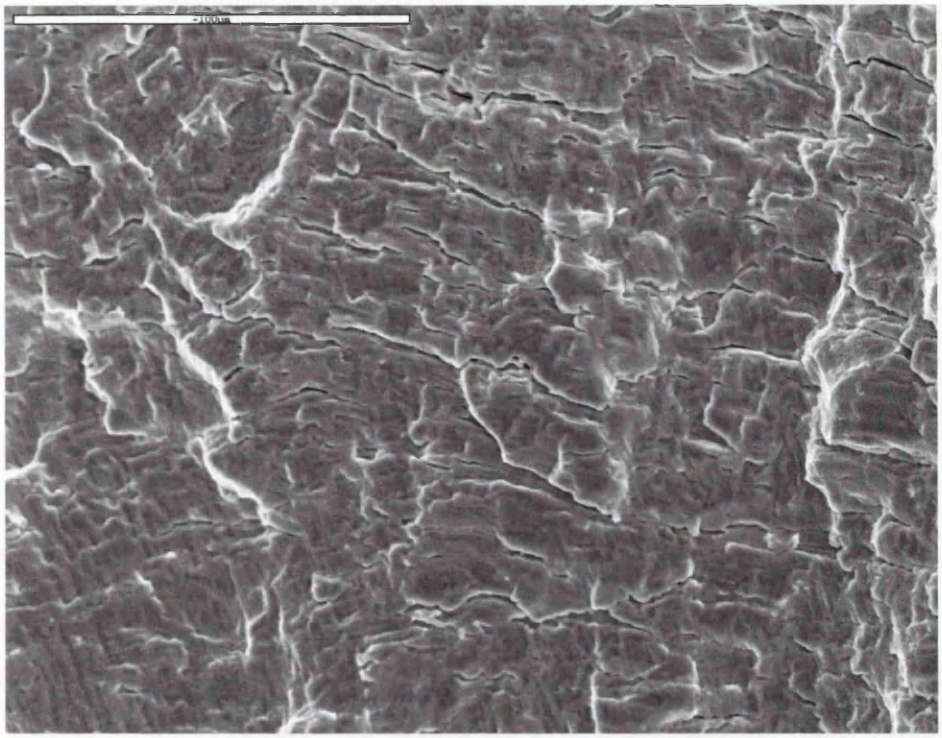

**Figure 6.15 - Strain control fracture surface (450°C, cyclic waveform), with surface delamination (secondary cracking)**

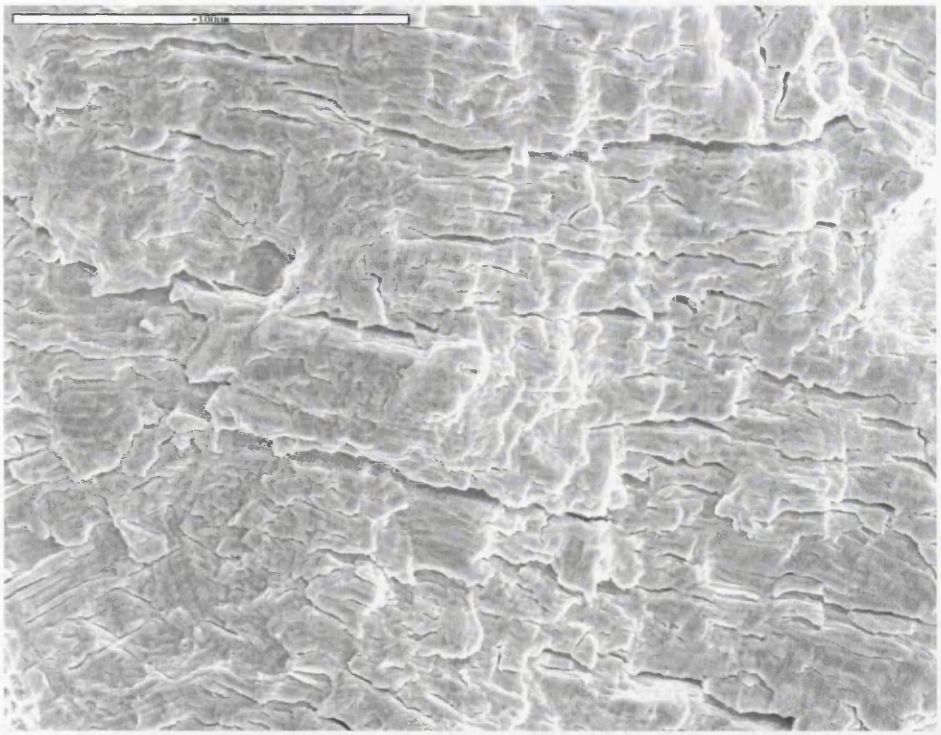

**Figure 6.16- Strain control fracture surface (500°C, cyclic waveform), with sub-surface cracking**

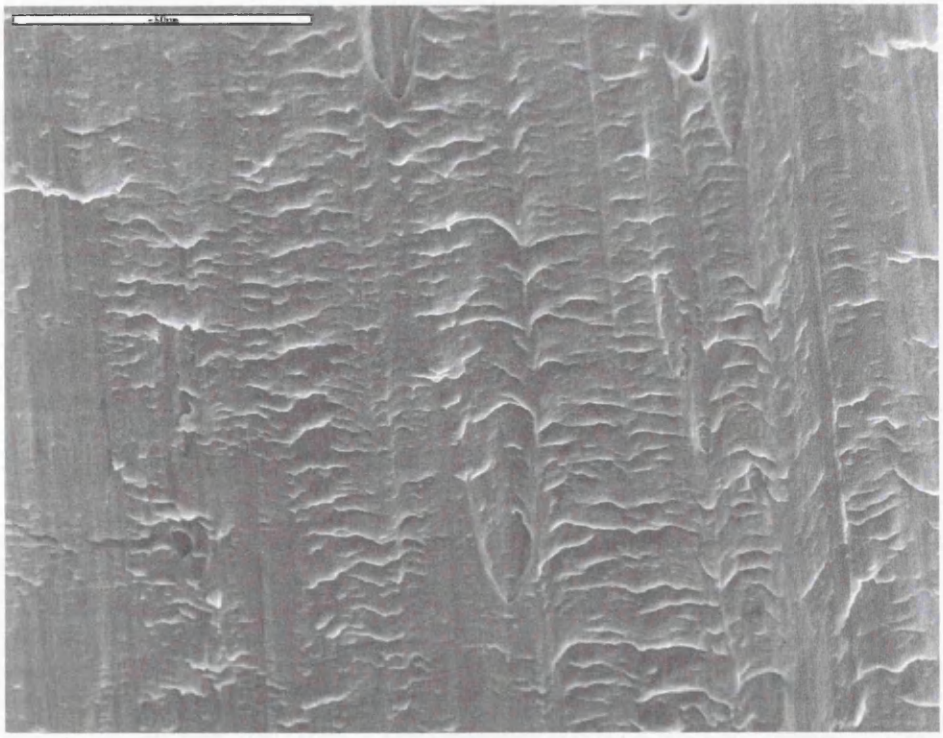

**Figure 6.17 - Strain control fracture surface (500°C, cyclic waveform) due to shear**

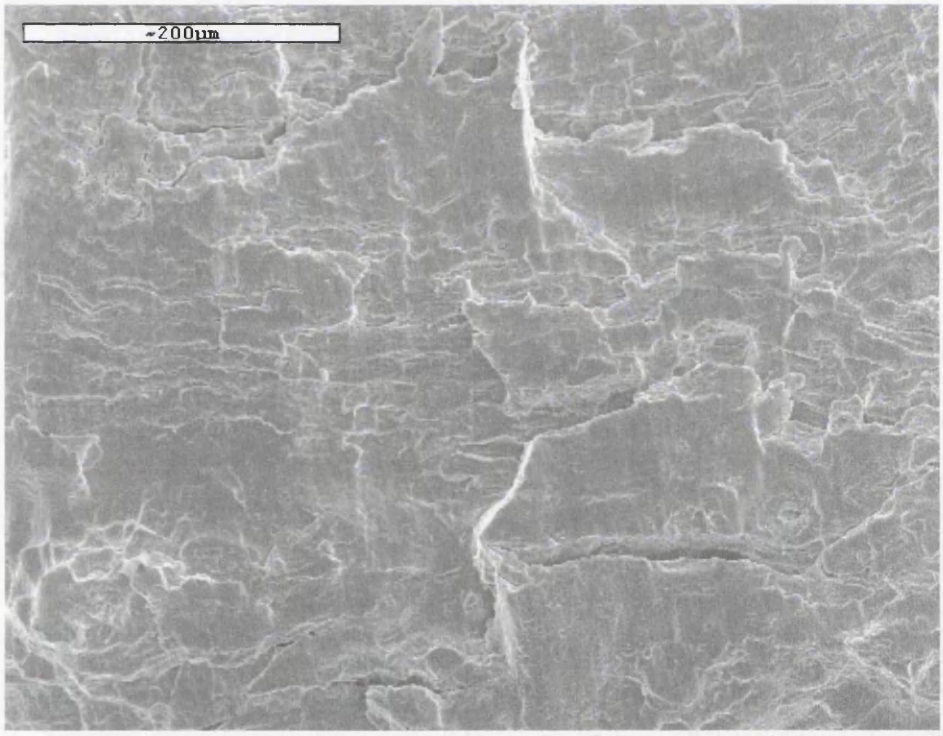


**Figure 6.18 - Strain control fracture surface (550°C, cyclic waveform), with sub-surface cracking**

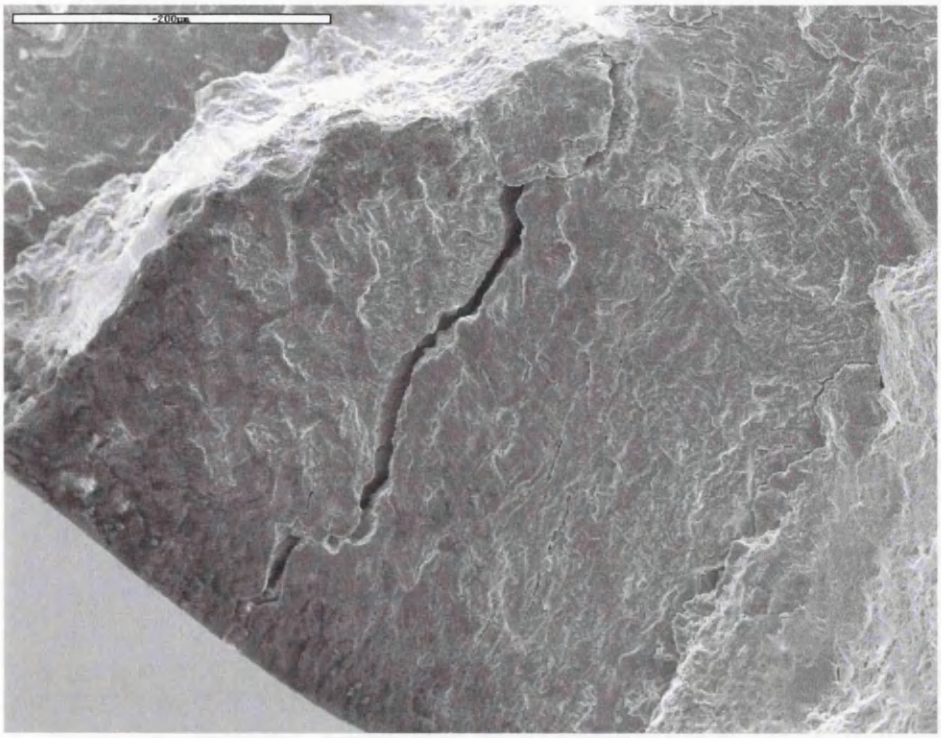

**Figure 6.19 - Strain control fracture surface (550°C, cyclic waveform), with fracture originating from surface.**

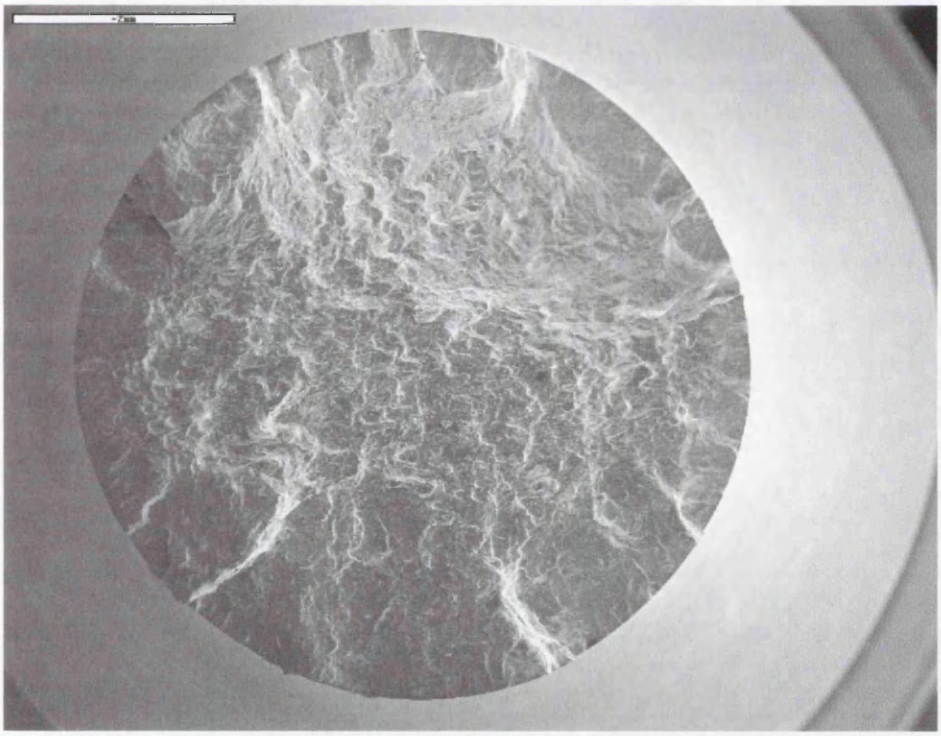

**Figure 6.20 - Overview of strain control fracture surface (450°C, 2 min dwell in tension)**

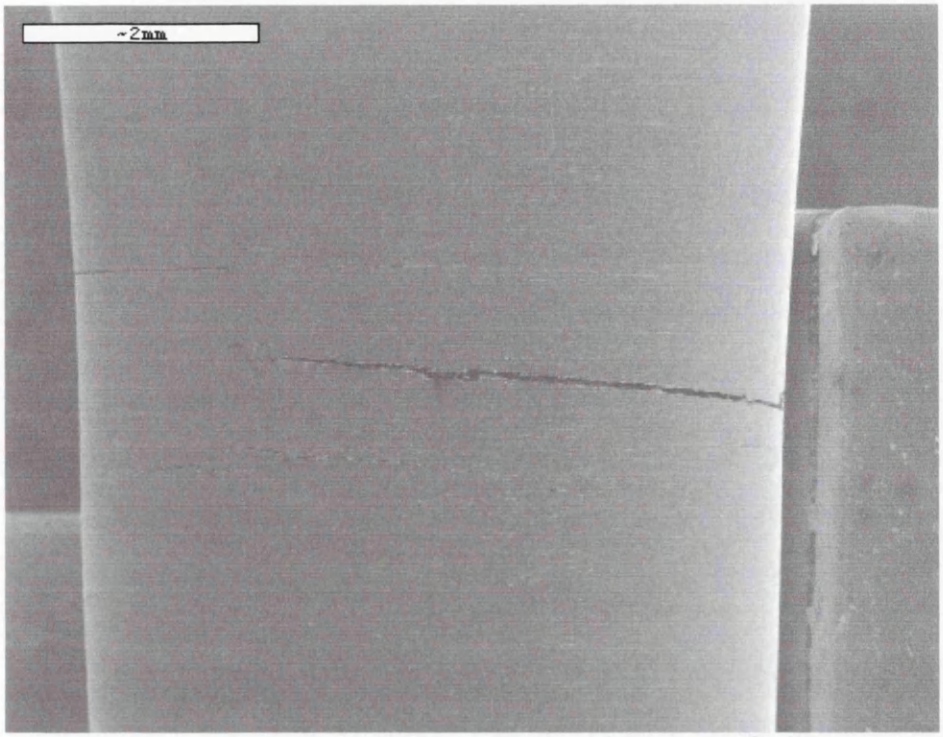


**Figure 6.21 – Gauge length of strain control specimen (500°C, 2 min dwell in tension), with surface cracks.**

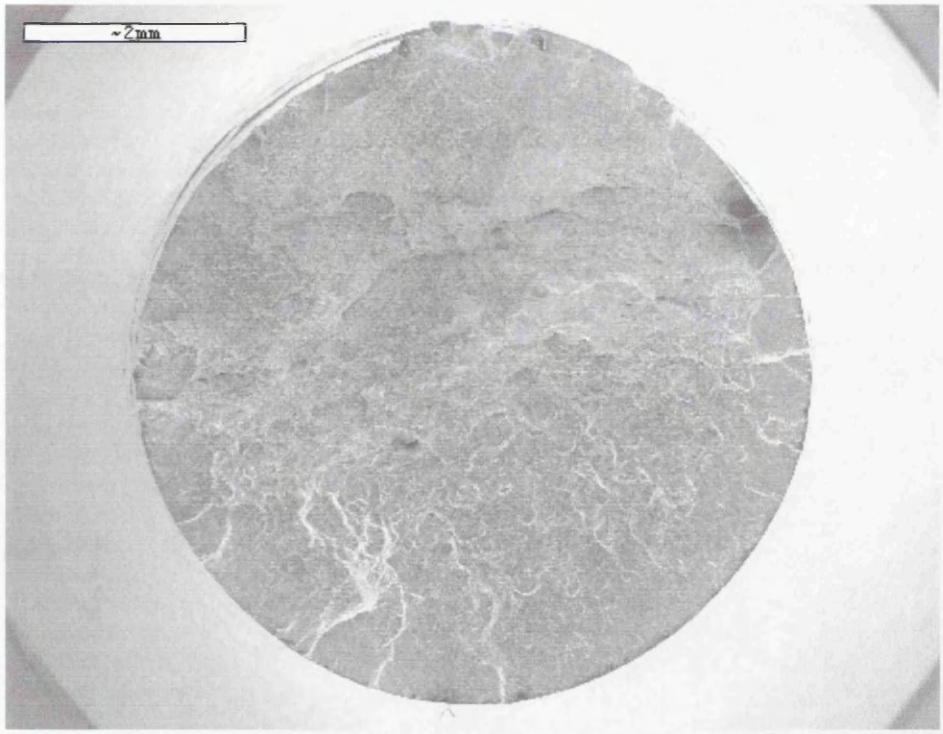


**Figure 6.22 - Overview of strain control fracture surface (550°C, 2 min dwell in tension)**

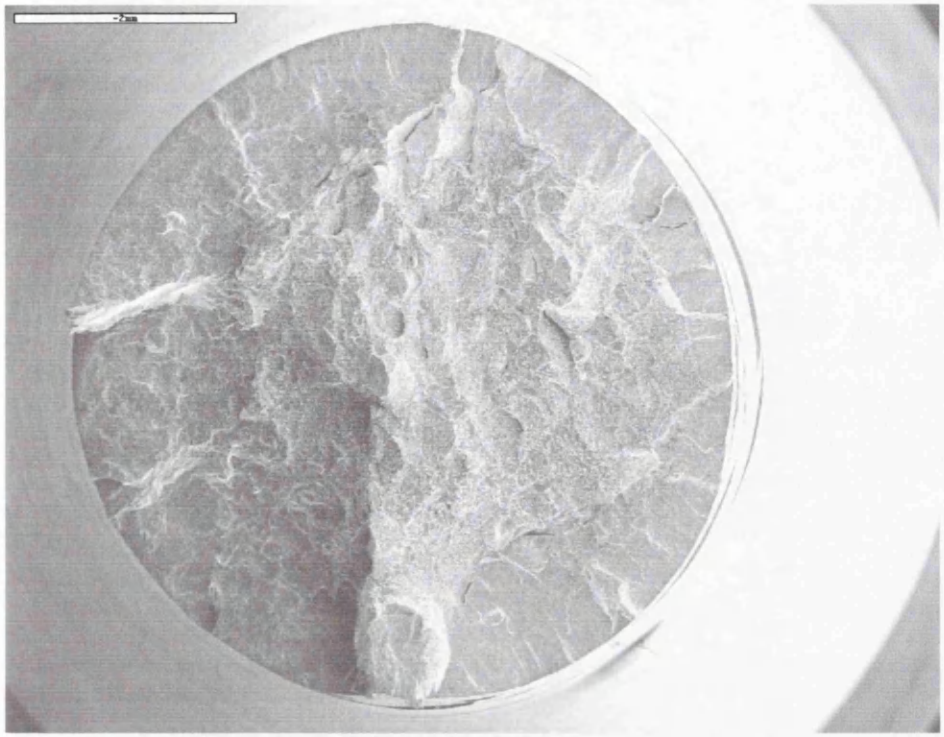

**Figure 6.23 - Overview of strain control fracture surface (550°C, 2 min dwell in tension and compression).**

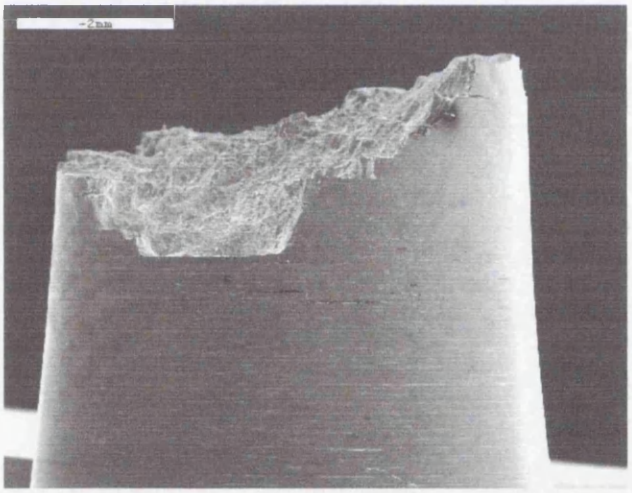

**Figure 6.24 - Strain control gauge length (450°C, 2 min dwell in tension), with multiple surface cracks**

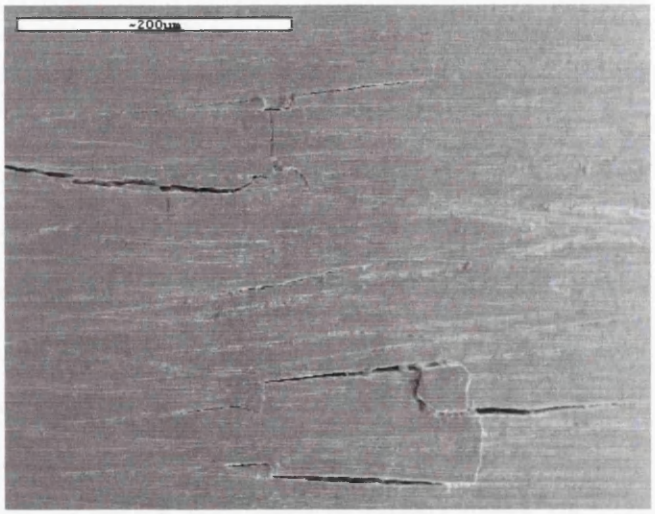


**Figure 6.25 - Strain control gauge length (500°C, 2 min dwell in tension), with multiple surface cracks**

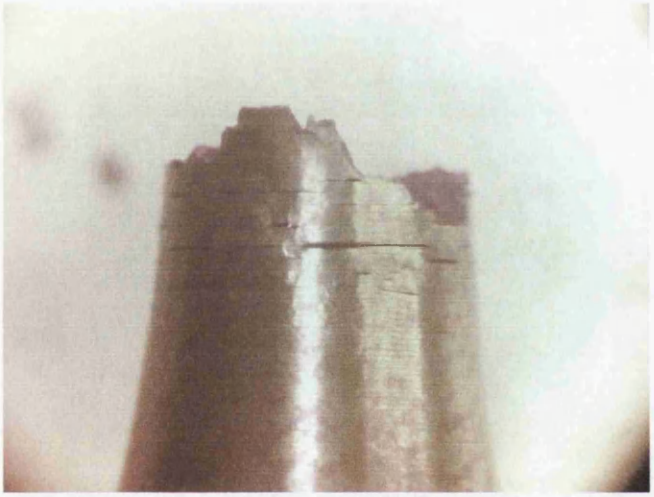

**Figure 6.26 - Strain control gauge length (550°C, 2 min dwell in tension), with multiple surface cracks.**

**Figure 6.27 - Strain control gauge length (550°C, 2 min dwell in tension and compression), with multiple surface cracks**

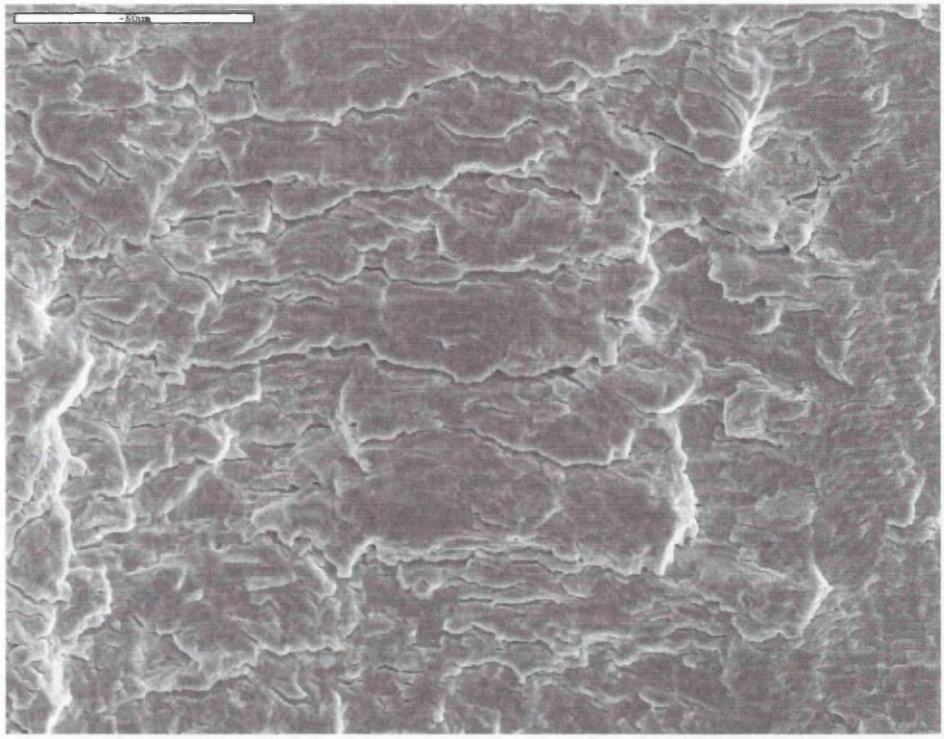

**Figure 6.28 - Strain control fracture surface (450°C, 2 min dwell in tension), with surface delamination.**

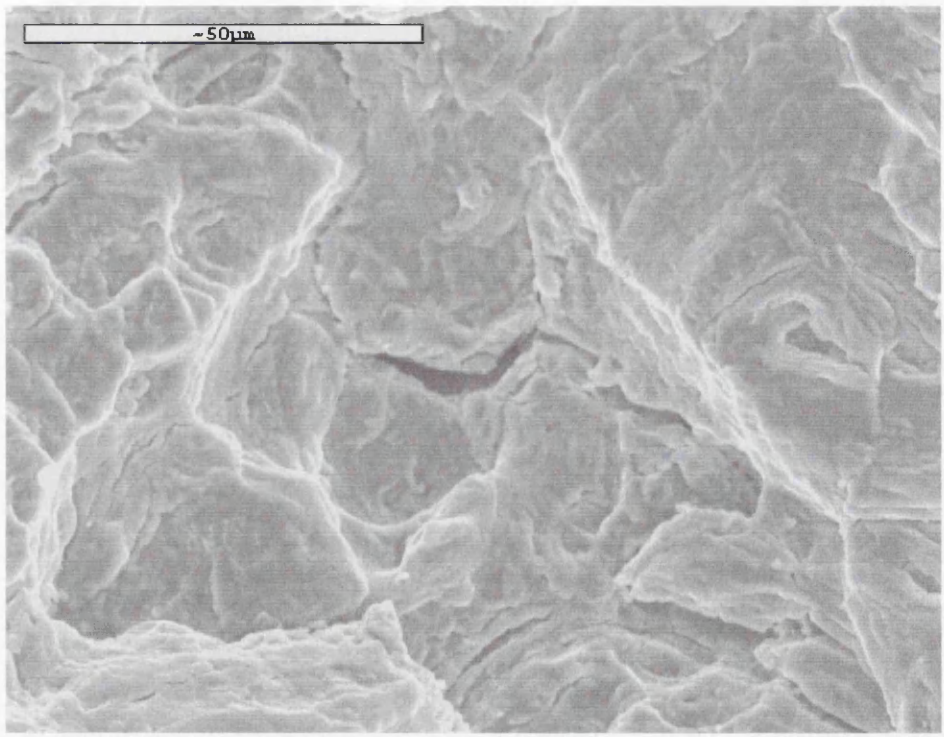


**Figure 6.29 - Strain control fracture surface (500°C, 2 min dwell in tension), with intergranular fracture**

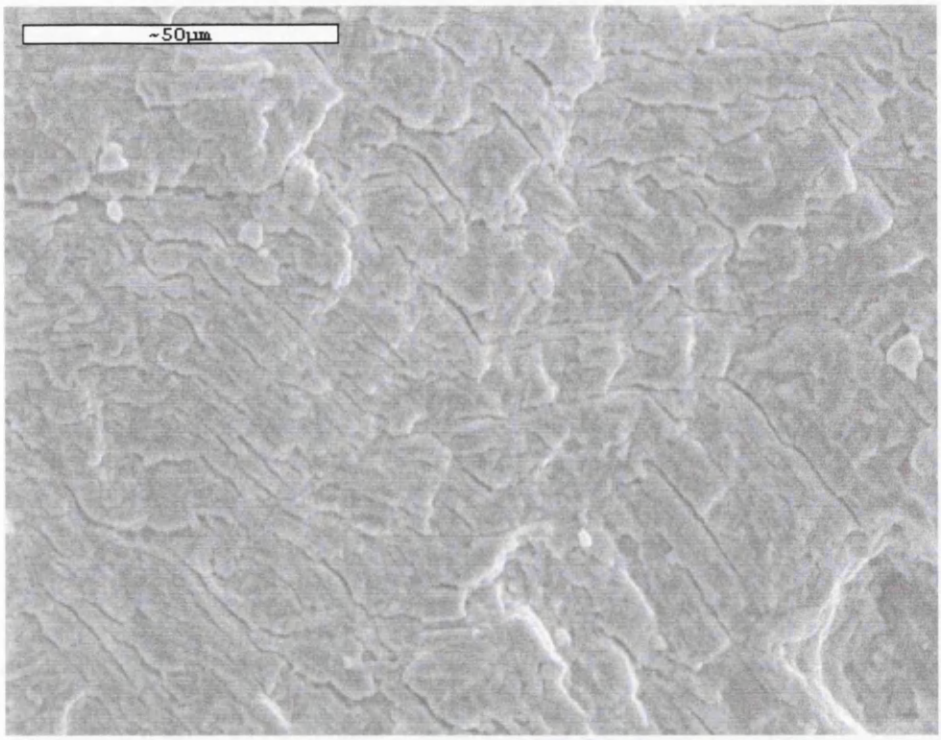


**Figure 6.30 - Strain control fracture surface (550°C, 2 min dwell in tension), with sub-surface cracking**

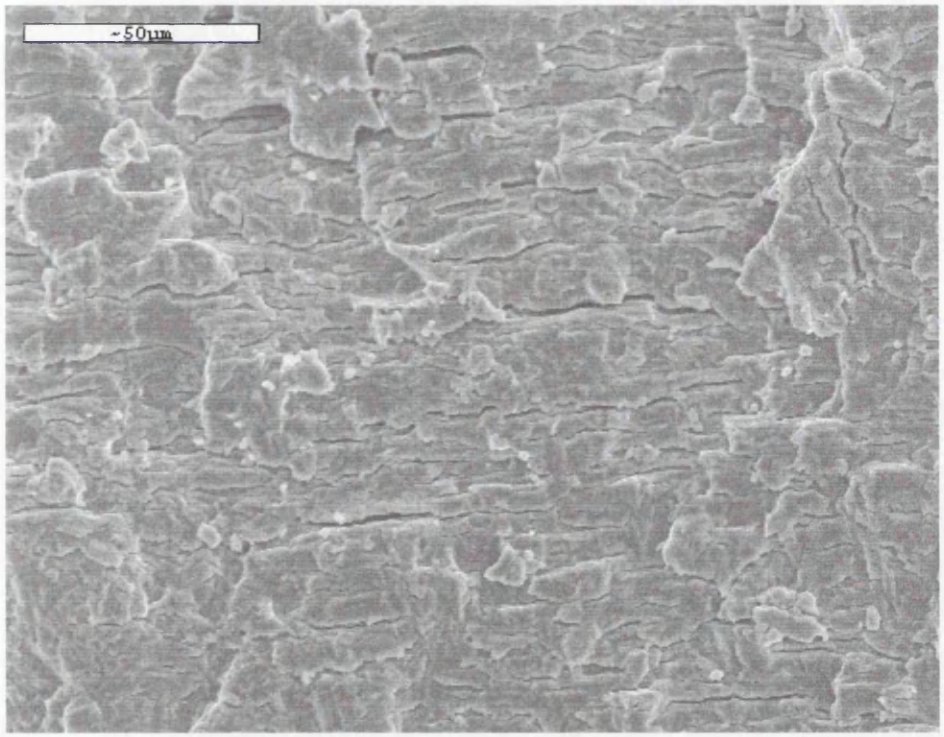


**Figure 6.31 - Strain control fracture surface (550°C, 2 min dwell in tension and compression), with sub-surface cracking**

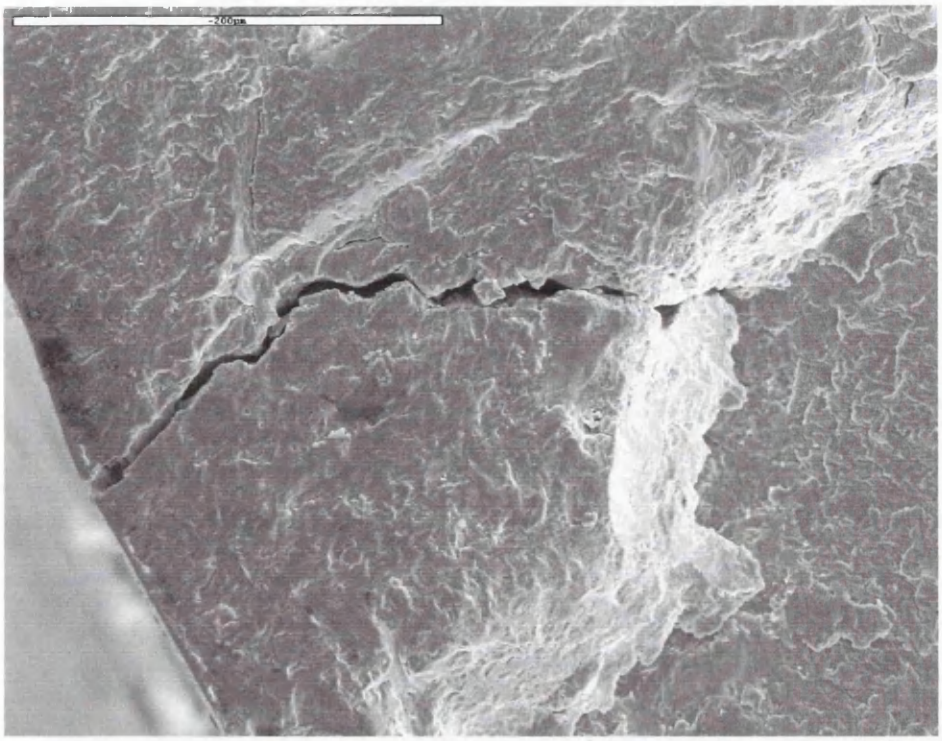

**Figure 6.32 - Strain control fracture surface (450°C, 2 min dwell in tension), with fracture originating from surface.**

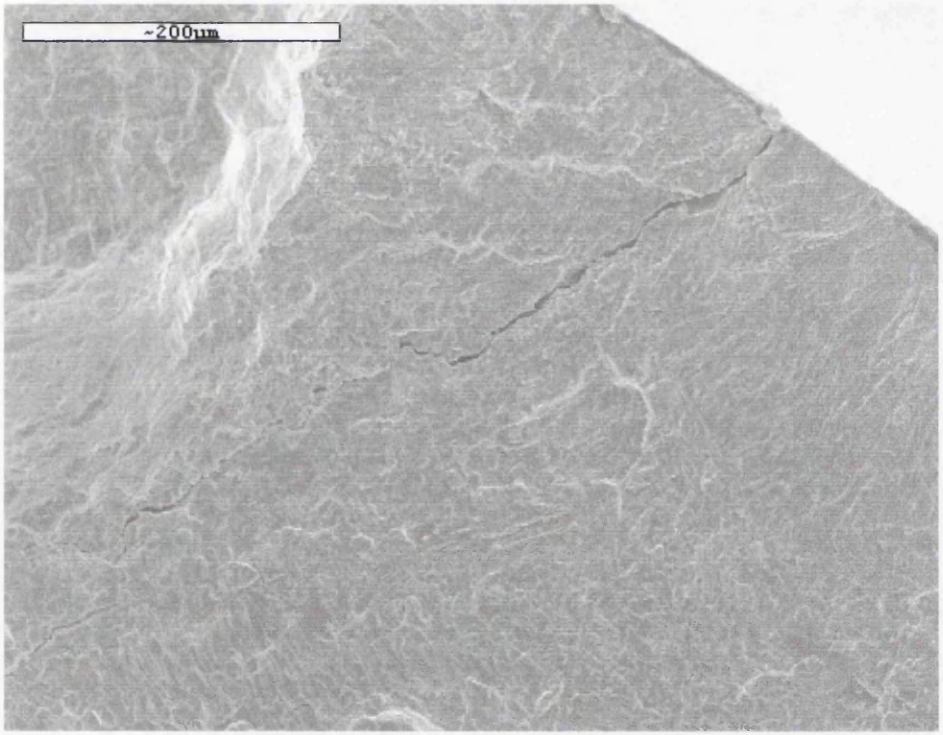


**Figure 6.33 - Strain control fracture surface (550°C, 2 min dwell in tension), with fracture originating from surface.**

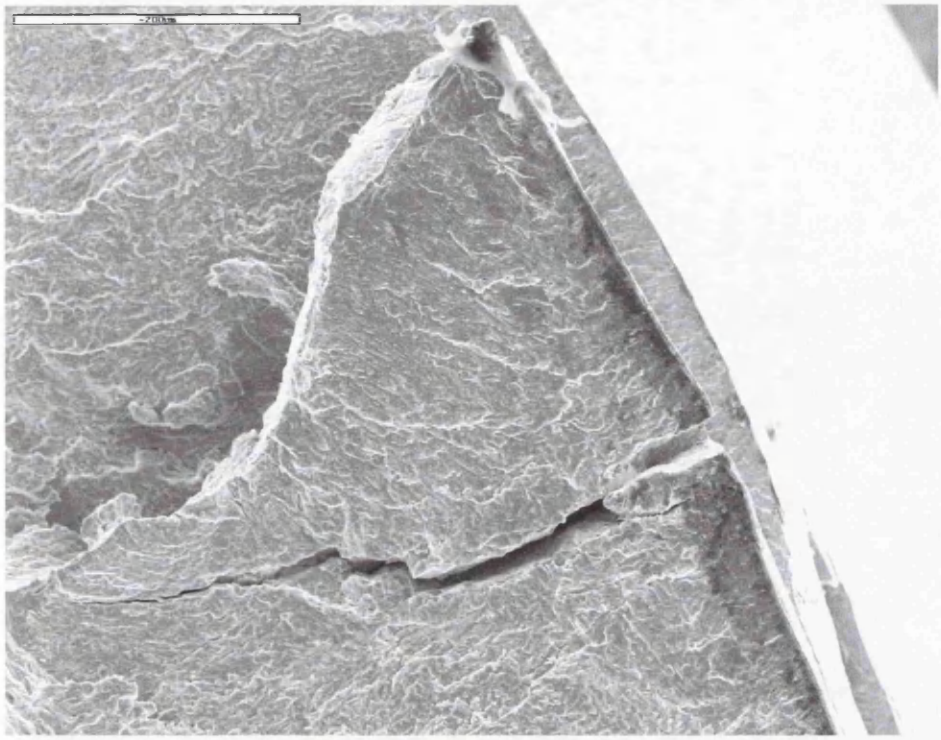

**Figure 6.34 - Strain control fracture surface (550°C, 2 min dwell in tension and compression), with fracture originating from surface.**

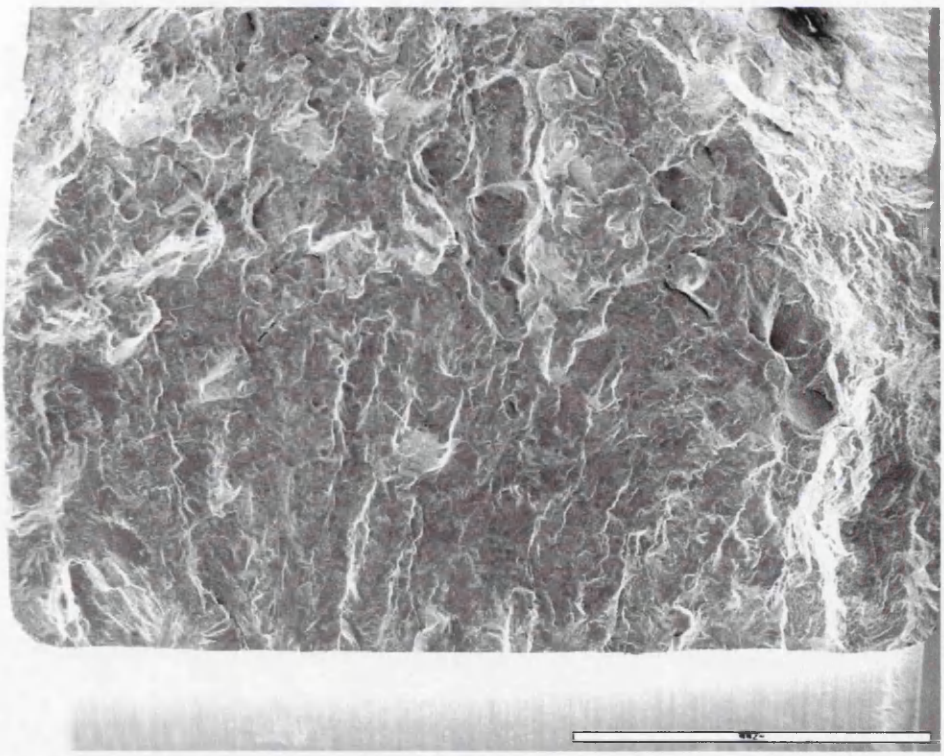

**Figure 6.35 – Overview of DEN fracture surface (450°C, in air, cyclic waveform), with multiple surface initiation**

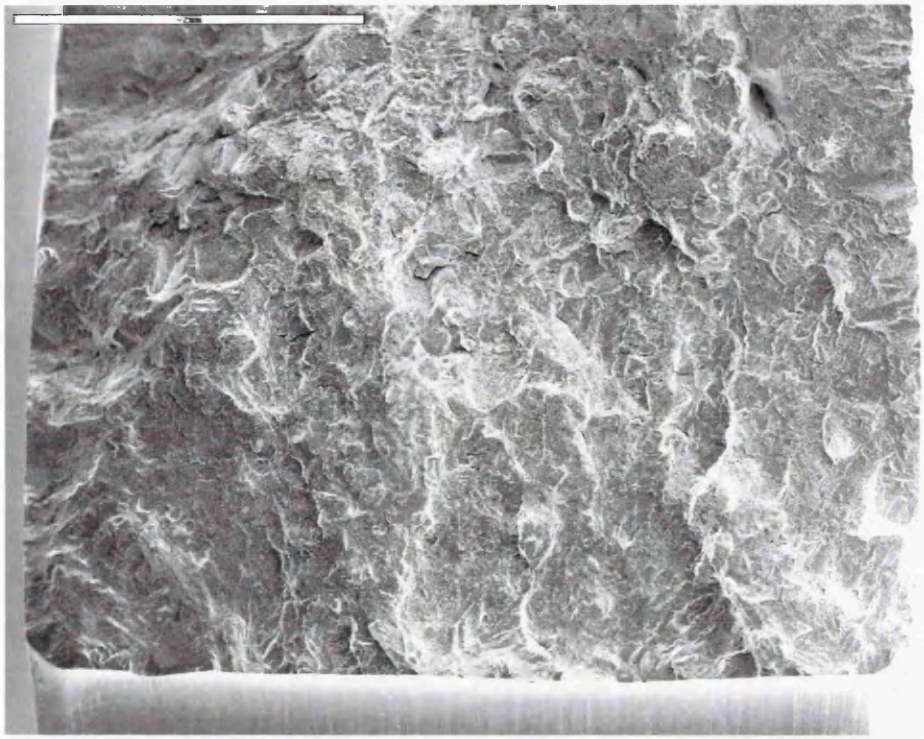

**Figure 6.36 - Overview of DEN fracture surface (450°C, in air, cyclic waveform), with multiple surface initiation**

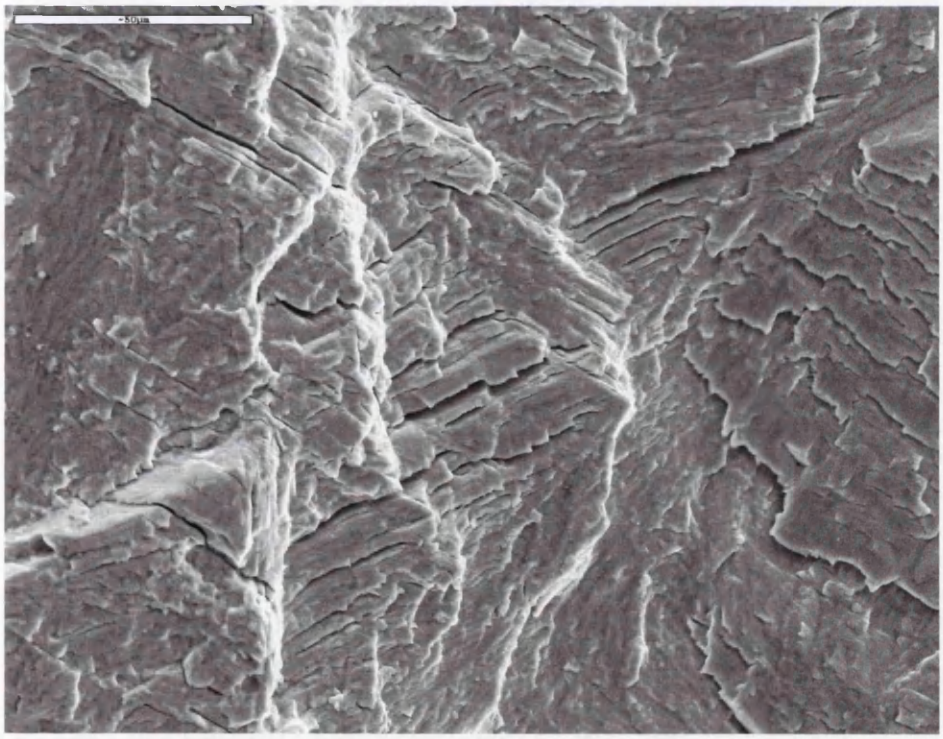

**Figure 6.37 - DEN fracture surface (450°C, in air, cyclic waveform), with sub-surface cracking at the α–β interface**

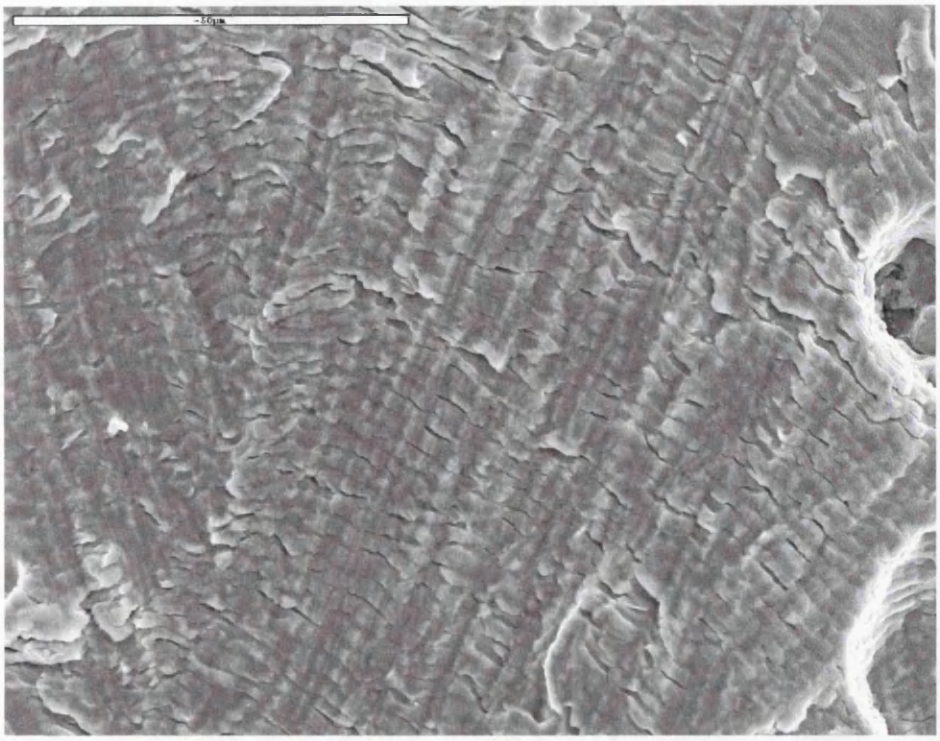

**Figure 6.38 - DEN fracture surface (450°C, in air, cyclic waveform), with striations**

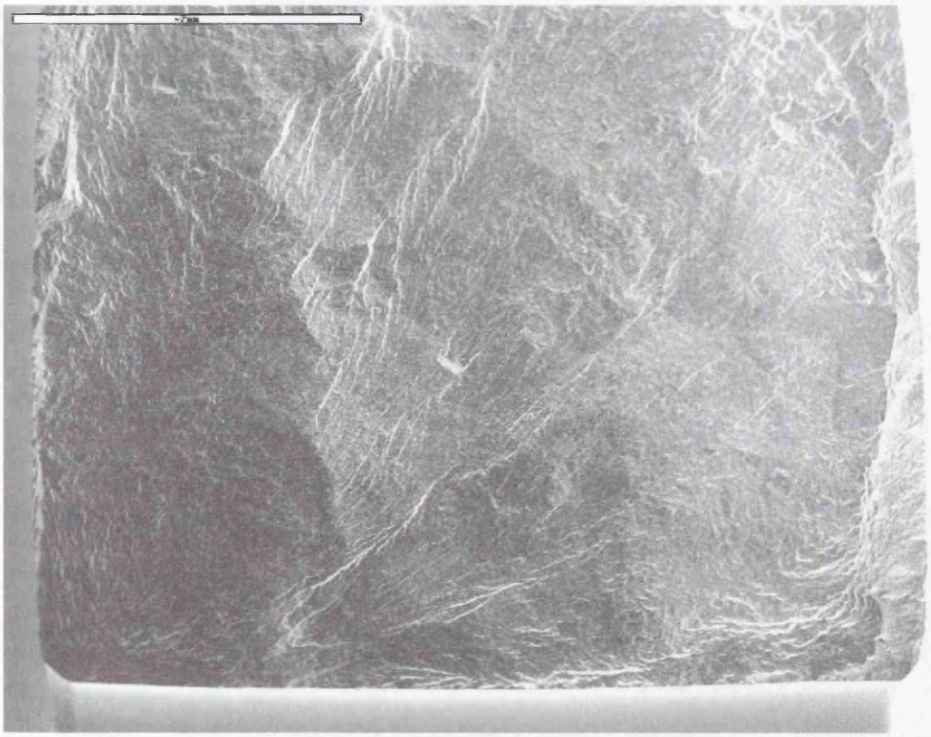

**Figure 6.39 - Overview of DEN fracture surface (450°C, in vacuum, cyclic waveform), with single surface initiation**

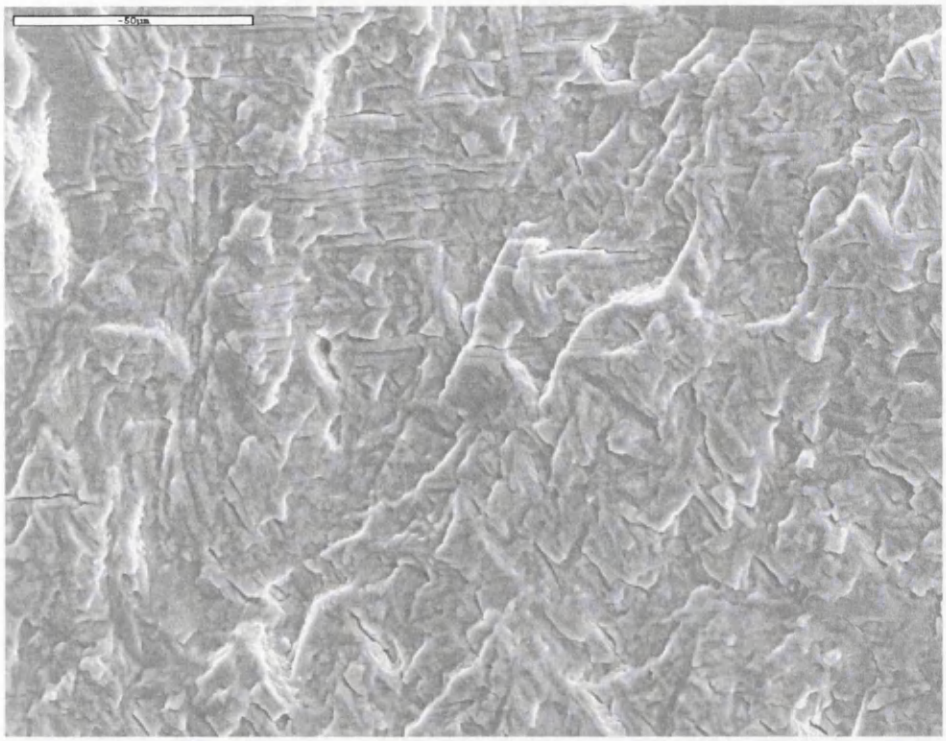

**Figure 6.40 - DEN fracture surface (450°C, in vacuum, cyclic waveform)**

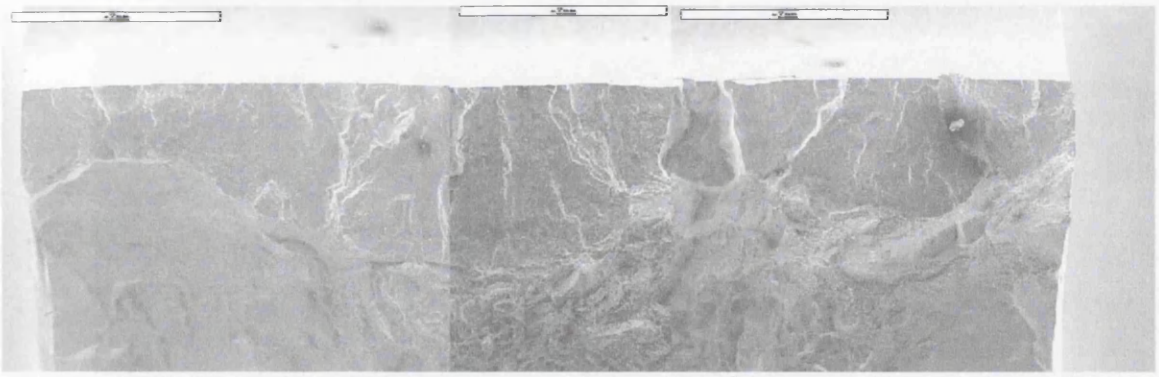

**Figure 6.41 - Overview of DEN fracture surface (550°C, in air, cyclic waveform), with multiple surface initiation**

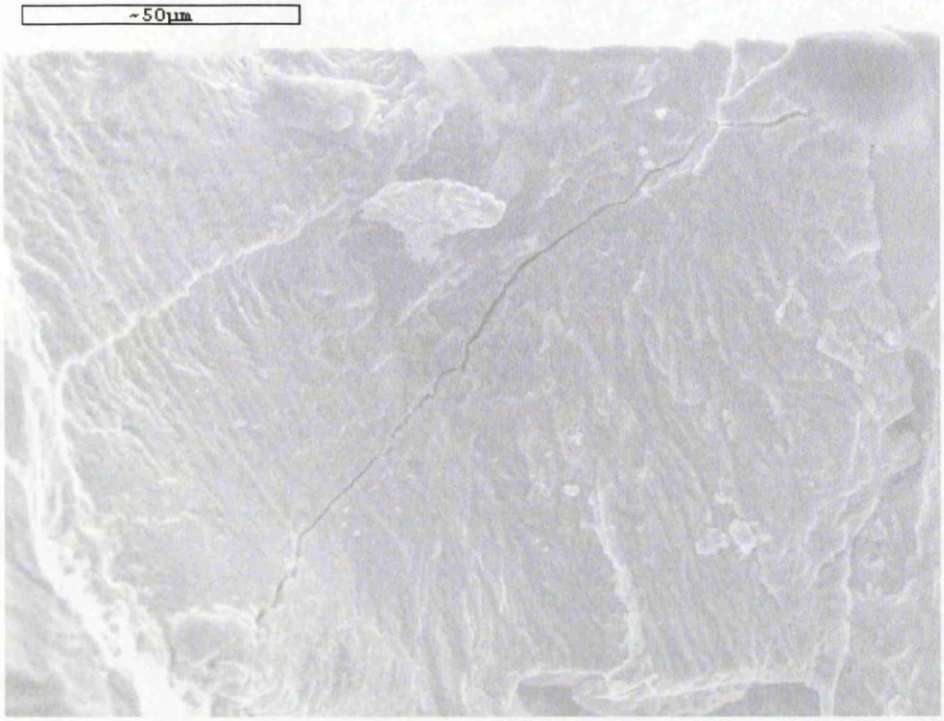


**Figure 6.42 - DEN fracture surface (550°C, in air, cyclic waveform), with fracture originating from surface**

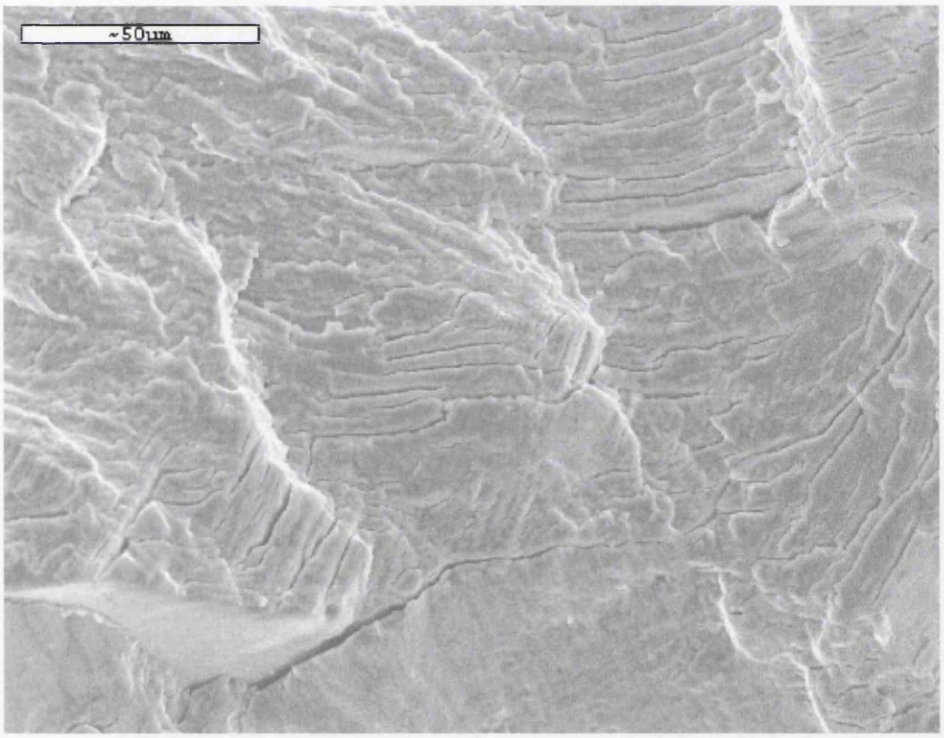


**Figure 6.43 - DEN fracture surface (550°C, in air, cyclic waveform), sub-surface cracking**

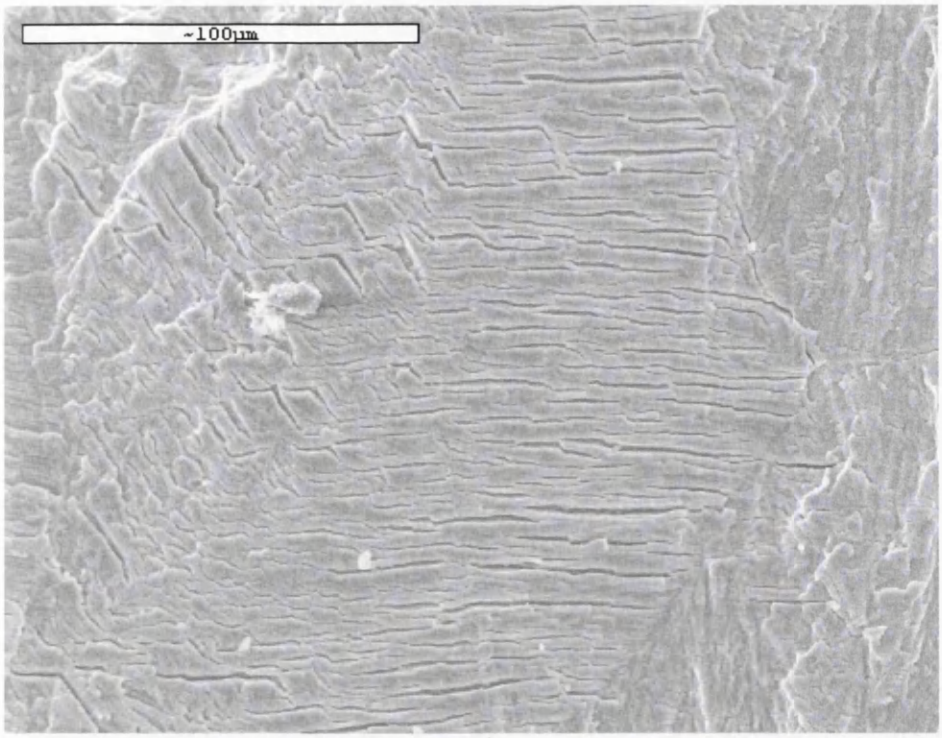


**Figure 6.44 - DEN fracture surface (550°C, in air, cyclic waveform), with sub-surface cracking at the α–β interface**

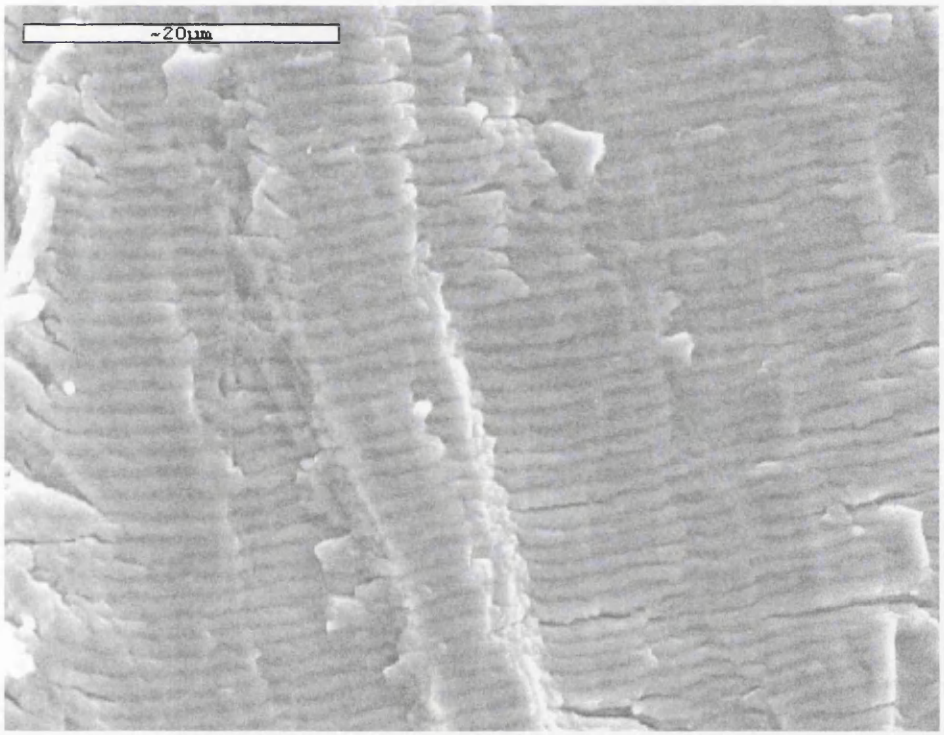


**Figure 6.45- DEN fracture surface (550°C, in air, cyclic waveform), with striations**

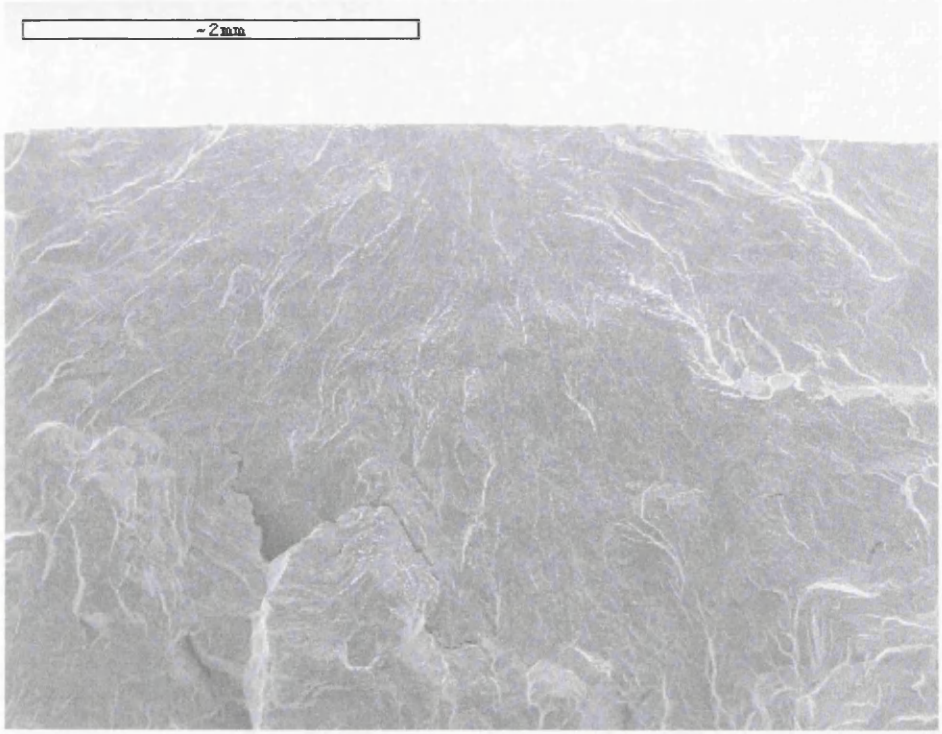


**Figure 6.46 - Overview of DEN fracture surface (550°C, in vacuum, cyclic waveform), with single surface initiation site**

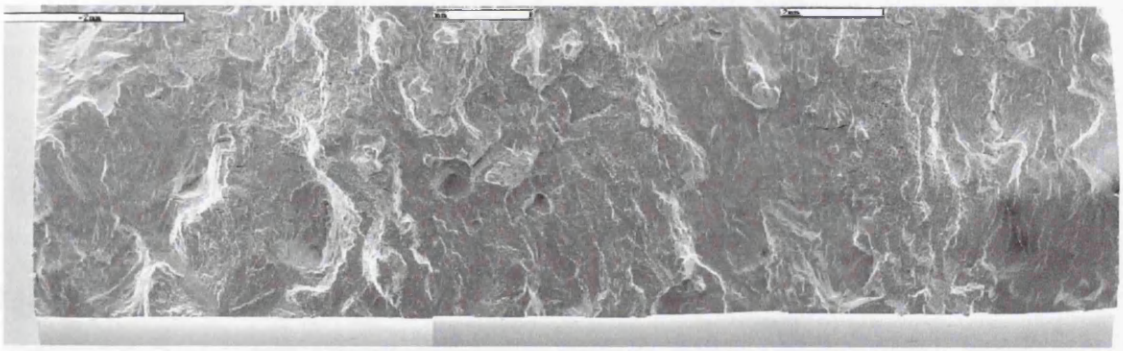

**Figure 6.47 - Overview of DEN fracture surface (500°C, in air, cyclic waveform)**

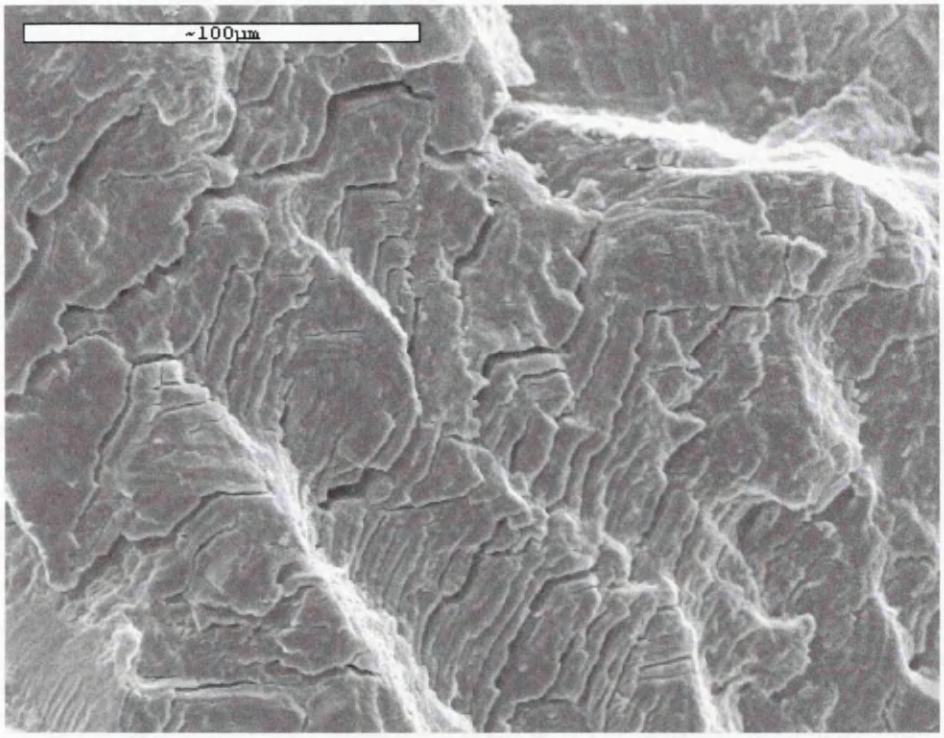


**Figure 6.48 - DEN fracture surface (500°C, in air, cyclic waveform), with sub-surface cracking at the α–β interface**

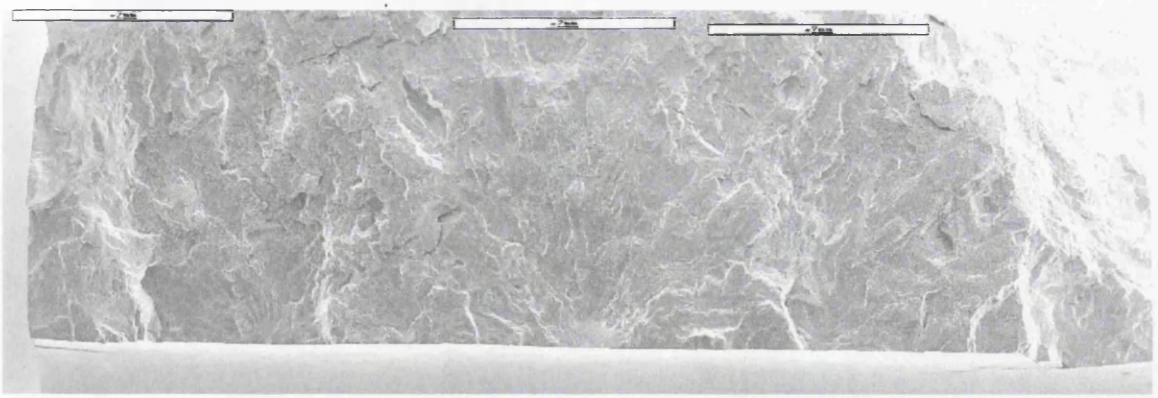

**Figure 6.49 - Overview of DEN fracture surface (500°C, in air, 2 min dwell)**

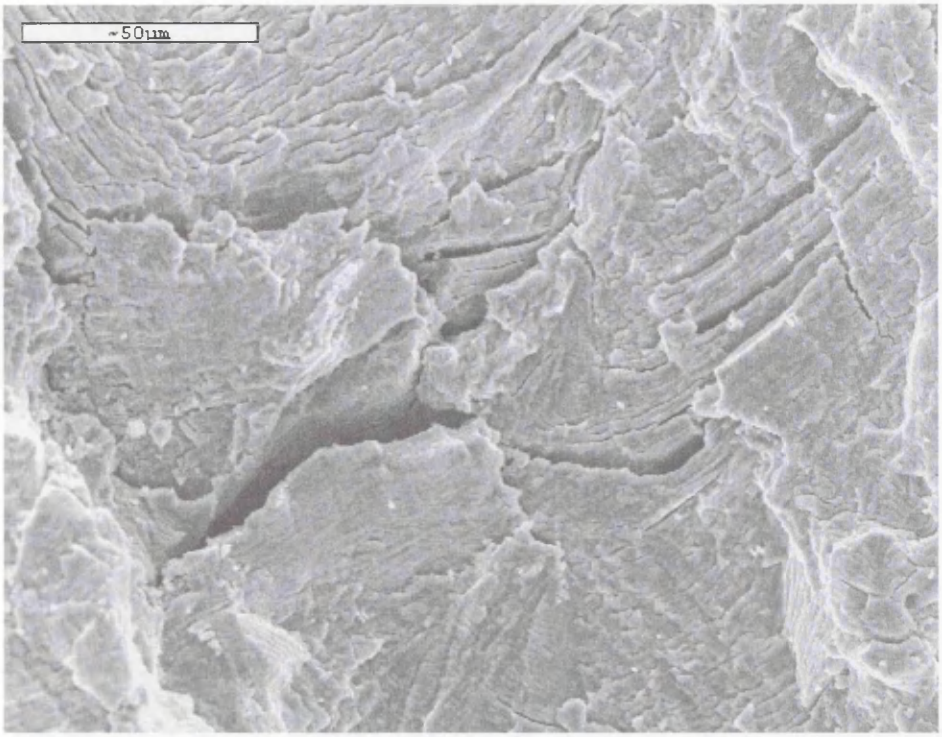


**Figure 6.50 - DEN fracture surface (500°C, in air, 2 min dwell), with sub-surface cracking**

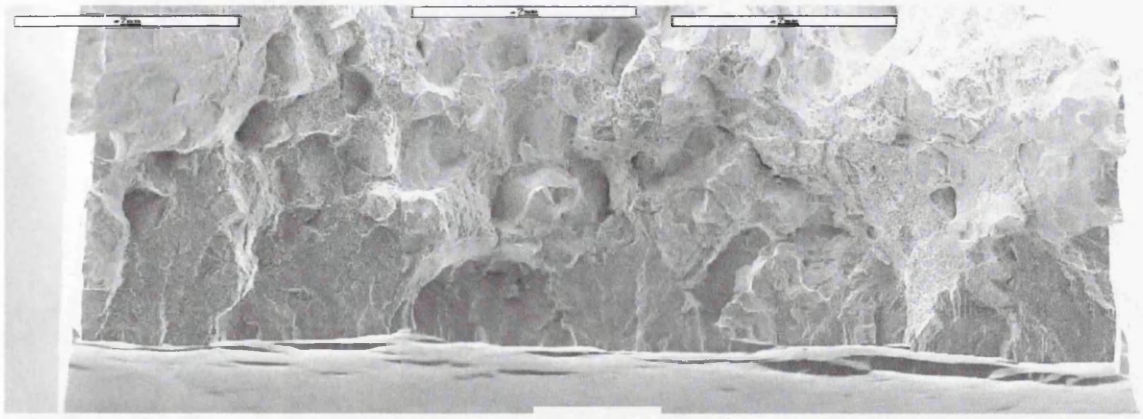

**Figure 6.51 - Overview of DEN fracture surface (550°C, in air, 2 min dwell), with multiple surface cracks**

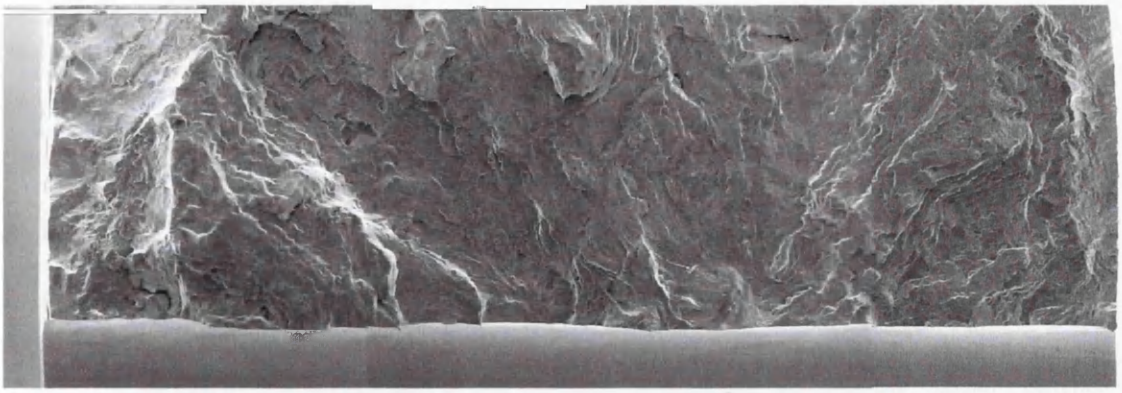

**Figure 6.52 - Overview of DEN fracture surface (550°C, in vacuum, 2 min dwell)**

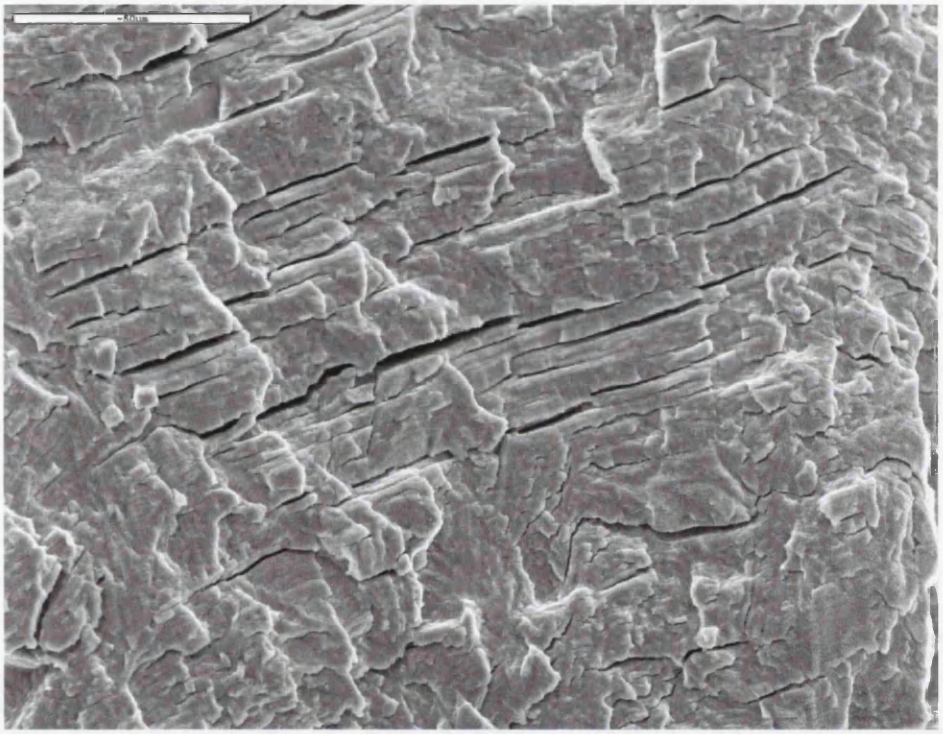

**Figure 6.53 - DEN fracture surface (550°C, in vacuum, 2 min dwell), with sub-surface cracking**

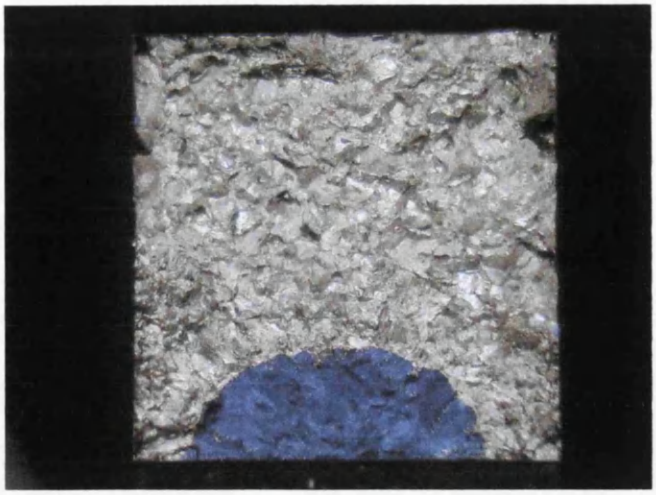

**Figure 6.54 – Overview of DEN fracture surface (550°C, in air, cyclic waveform, peak elastic stress of 750MPa), with single surface initiation site**

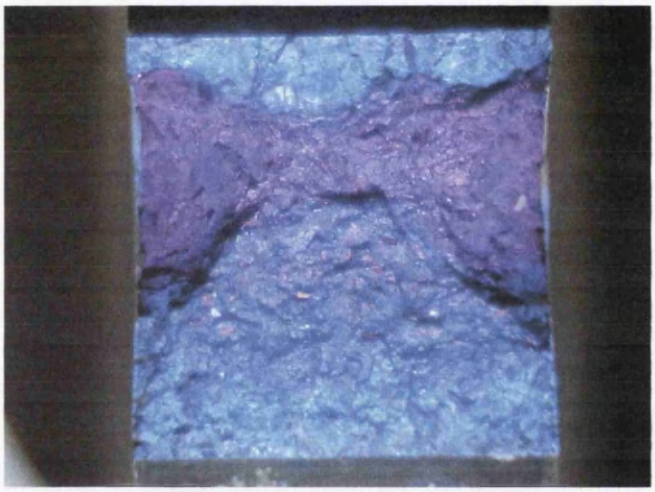

**Figure 6.55 - Overview of DEN fracture surface (550°C, in air, cyclic waveform, peak elastic stress of 1120MPa), with multiple surface initiation sites**

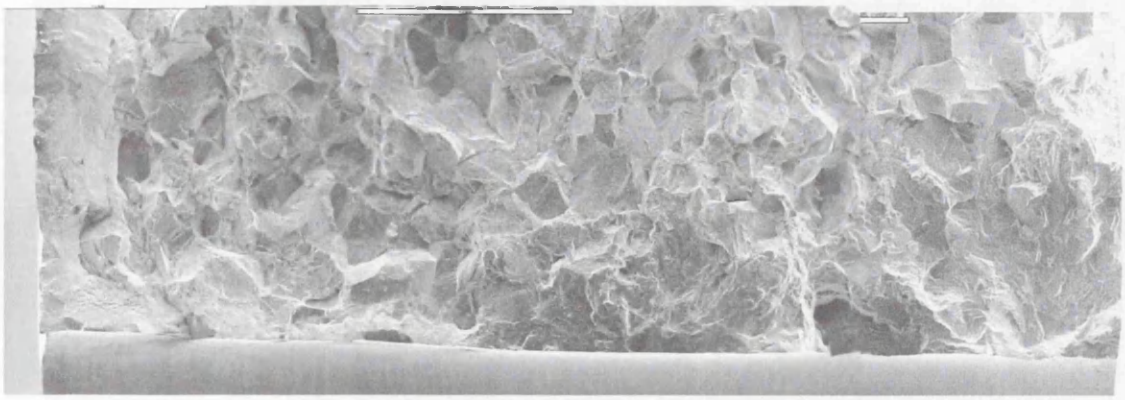

**Figure 6.56 - Overview of DEN facetted fracture surface (20°C, in air, cyclic waveform)**

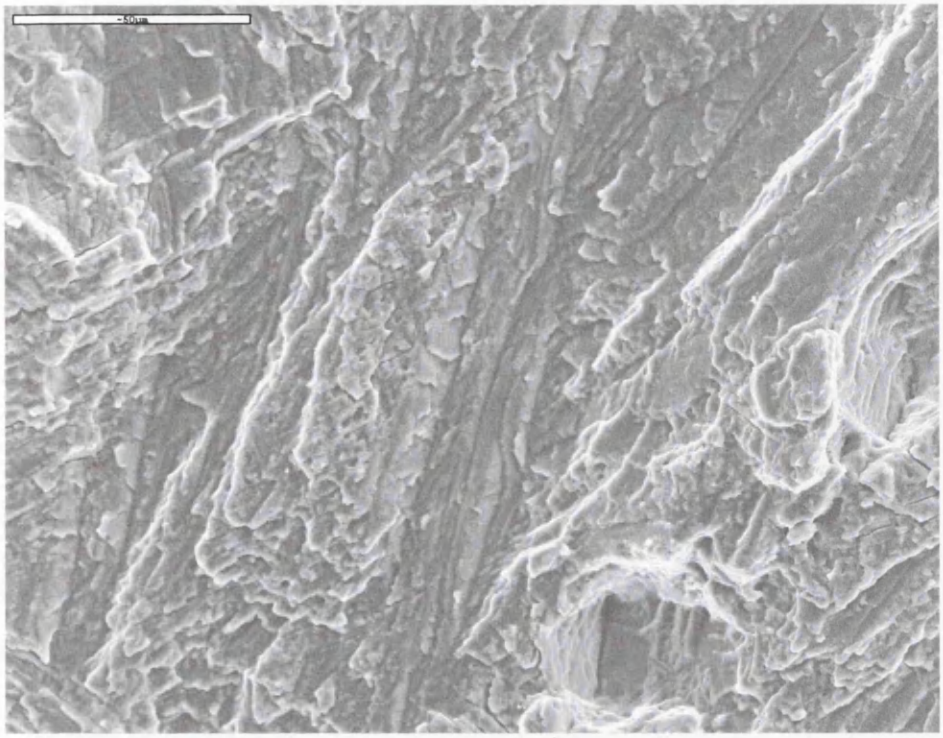

**Figure 6.57 - DEN fracture surface (20°C, in air, cyclic waveform)**

**Figure 6.58 – Overview of VCN fracture surface (20°C, in air, cyclic waveform)**

**Figure 6.59 - Overview of VCN fracture surface (450°C, in air, cyclic waveform)**

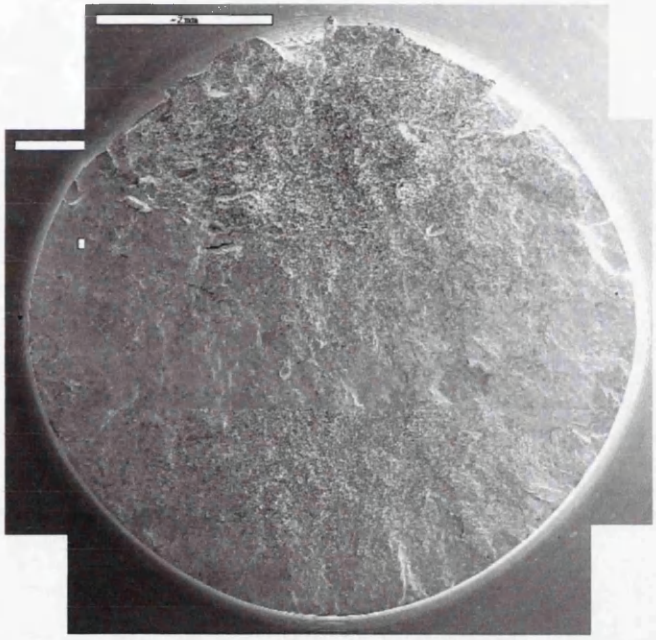

**Figure 6.60 - Overview of VCN fracture surface (500°C, in air, cyclic waveform)**

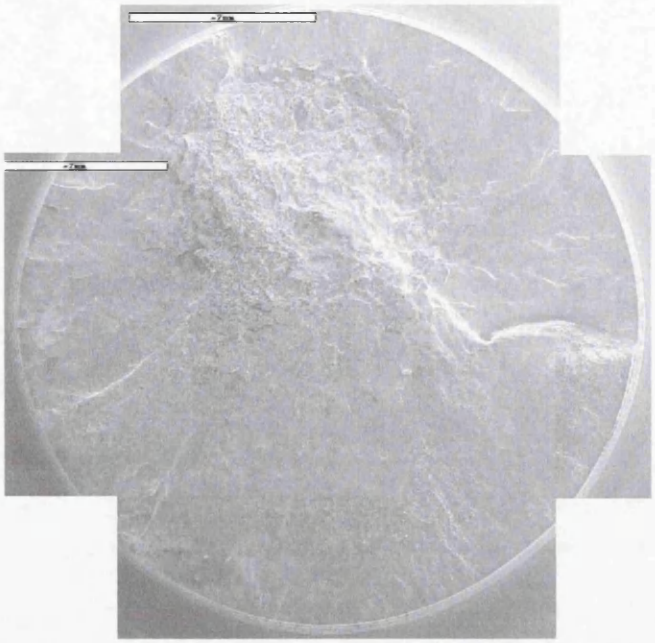

**Figure 6.61 - Overview of VCN fracture surface (550°C, in air, cyclic waveform)**

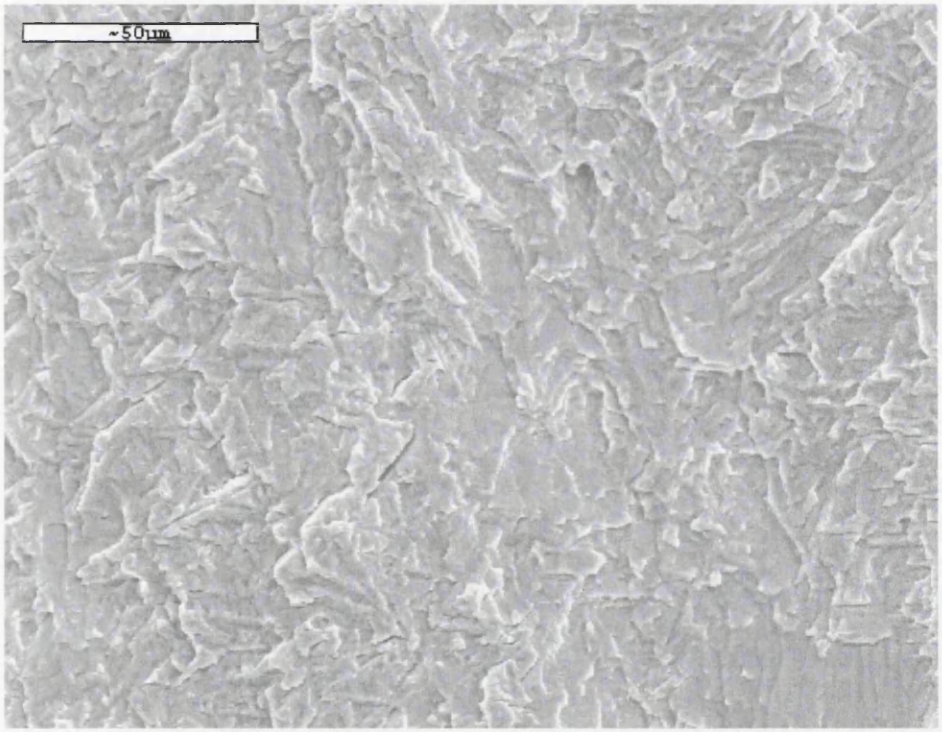


**Figure 6.62 - VCN fracture surface (20°C, in air, cyclic waveform)**

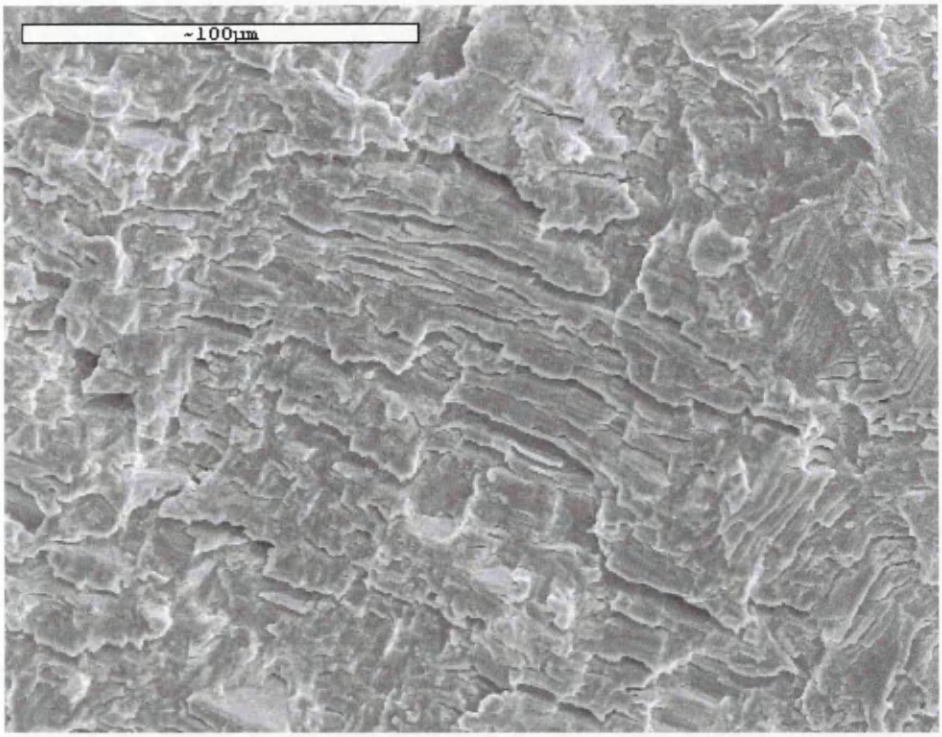


**Figure 6.63 - VCN fracture surface (450°C, in air, cyclic waveform), with sub-surface cracking**

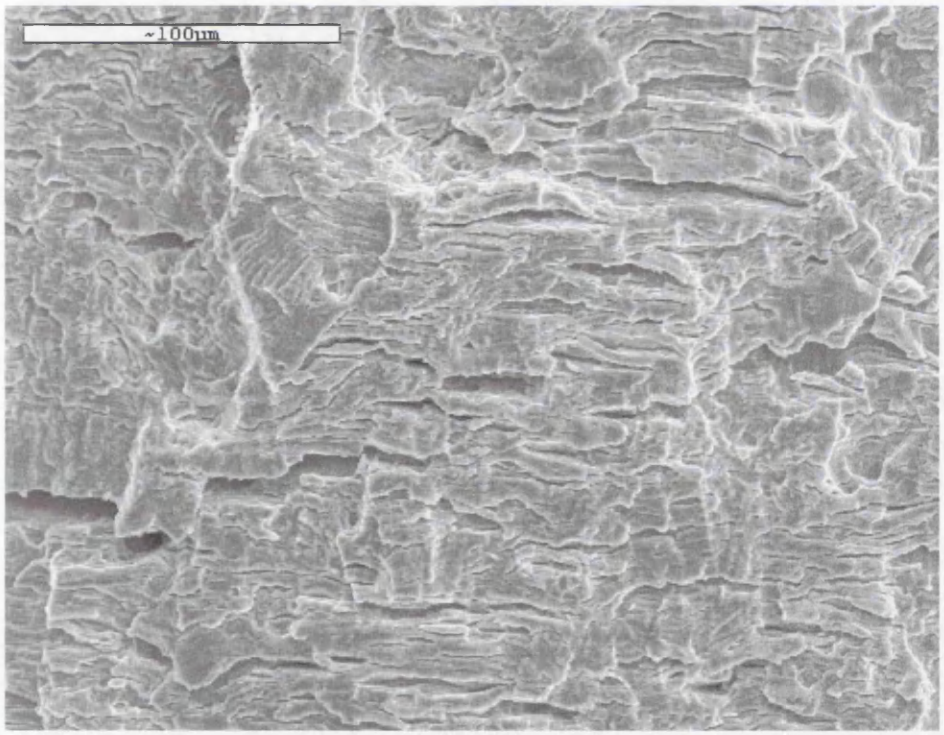


**Figure 6.64 - VCN fracture surface (500°C, in air, cyclic waveform), with sub-surface cracking**

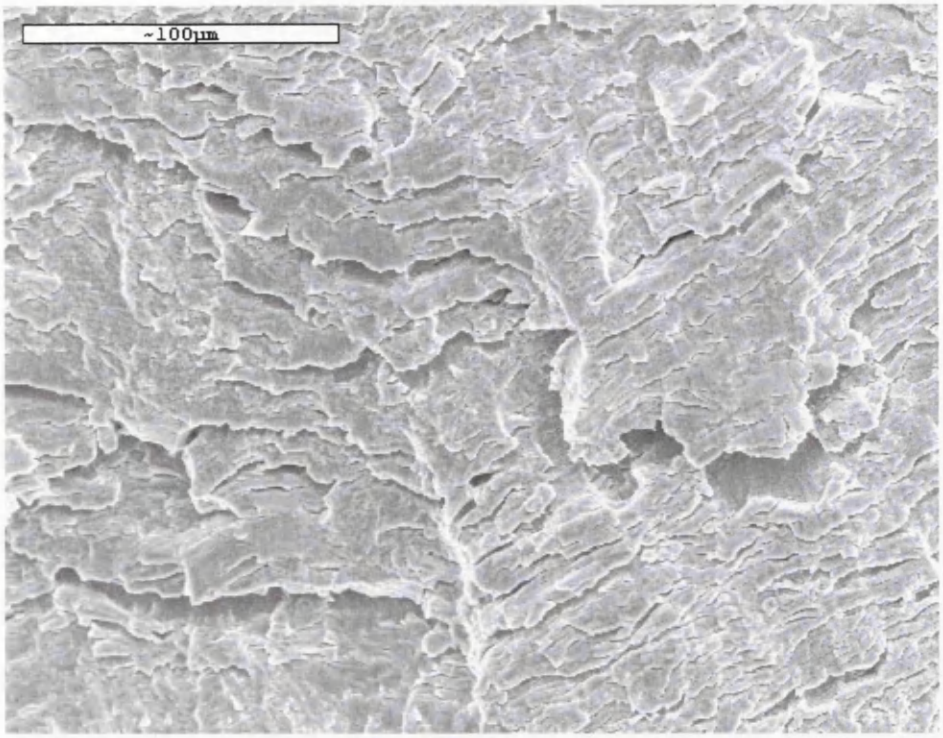


**Figure 6.65 - VCN fracture surface (550°C, in air, cyclic waveform), with sub-surface cracking**

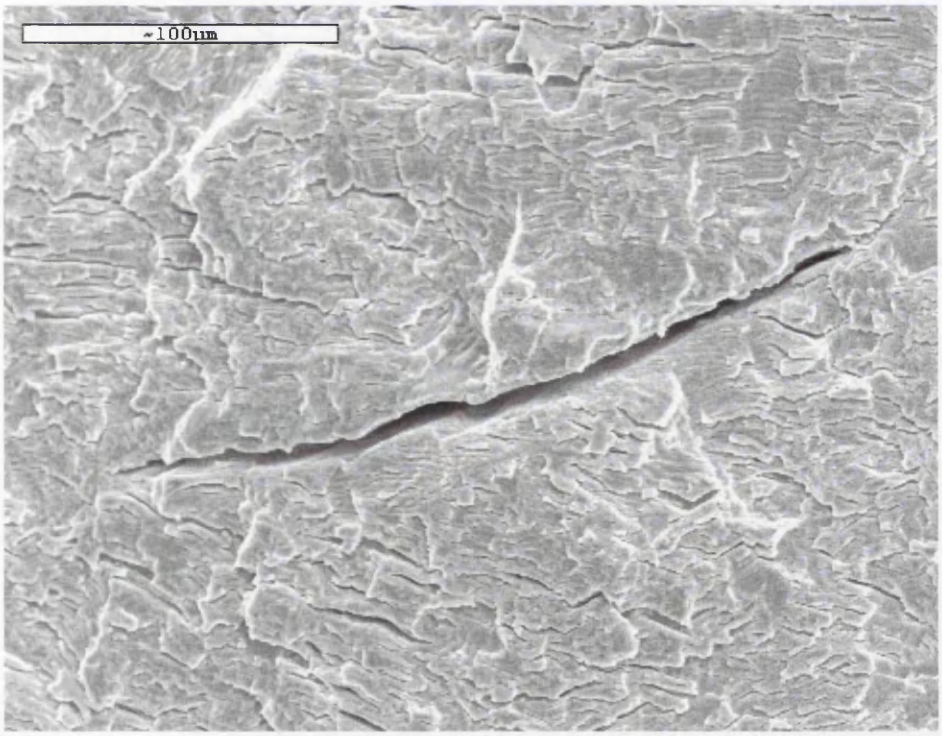


**Figure 6.66 - VCN fracture surface (550°C, in air, cyclic waveform), with large sub-surface crack**

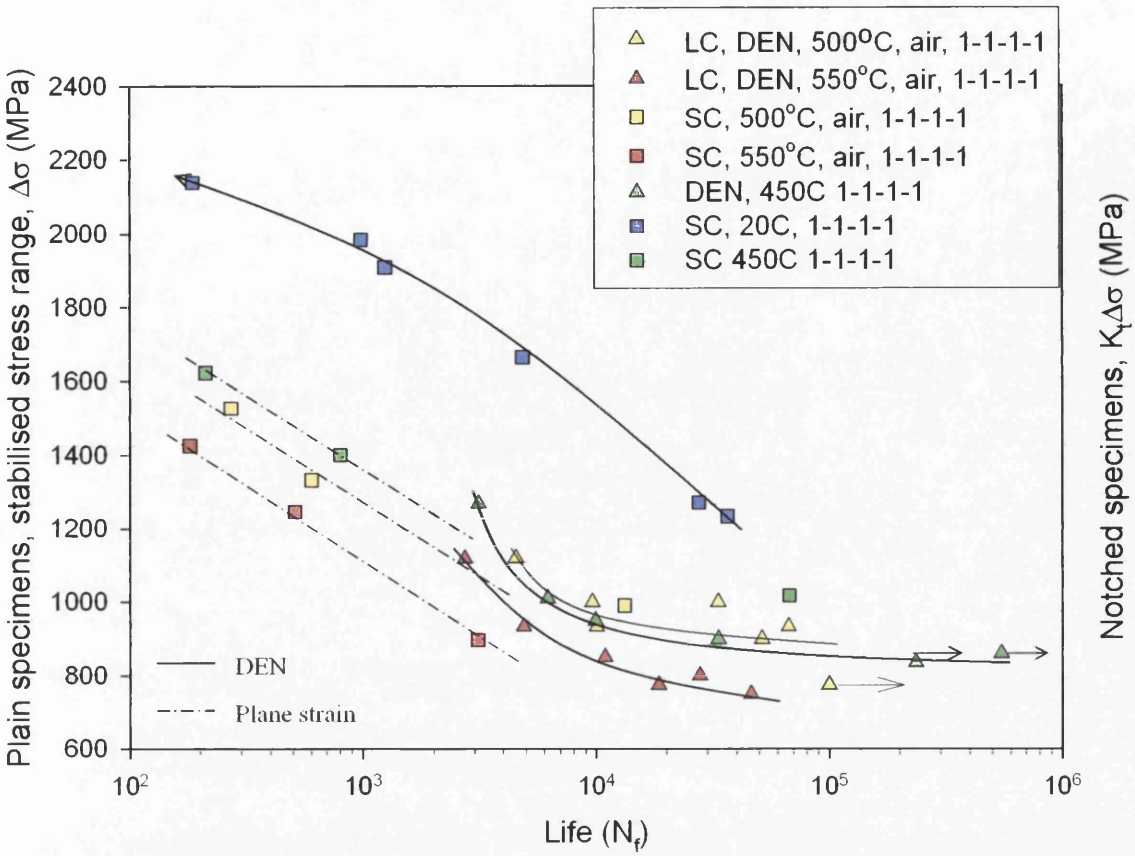


**Figure 6.67 – Comparison of plane strain and DEN data**

## 7.0 CONCLUSIONS

- The lack of dwell sensitivity of strain control tests was attributed to stress relaxation during the dwell period at peak tensile strain offsetting the damage of strain accumulation. During tests where there was a dwell period at peak tensile and compressive strains, strain damage accumulated during the tensile hold period was shown to reverse during the compressive hold period.

- Initiation was shown to account for 80 – 90% of total fatigue life for freely initiated DEN tests.

- Dwell crack propagation tests at elevated temperatures showed that the interaction of creep and environment with fatigue results in an increase in the crack propagation rate.

- Comparison of air and vacuum data indicates that for temperatures up to 550°C, environmental effects account for a significantly greater decrease in fatigue life, compared to creep effects. The dominance of environmental effects on high temperature fatigue is even more significant at higher stresses.

- At temperatures of 500°C it was shown through the analysis of plane strain control deformation data that creep leads to a reduction in peak stress (i.e. stress relaxation) at the DEN notch root, which results in a greater fatigue life than the lower temperature of 450°C. This indicates that creep is beneficial to fatigue life up to 500°C. While at the higher temperature of 550°C, the larger accumulation of creep strain at the notch root and net section leads to a

significant reduction in fatigue life. This effect was not seen in VCN tests, indicating that differing specimen geometries affect the levels of stress relaxation at these temperatures.

- A transition in damage mechanisms was seen for high temperature fatigue tests in air as the stress range reaches approximately 1000MPa. It was shown that this stress range corresponds to the onset of plastic deformation, which results in cracking of the surface oxide layer, allowing ingress of the environment, which facilitates crack initiation and propagation.

- For elevated temperature tests at stress ranges greater than approximately 1000MPa, plane strain control tests experienced significantly shorter fatigue lives than notched tests when compared using a peak elastic stress concentration factor ($K_t$). This was attributed to a reduction in environmental damage in the notched specimens once the fatigue crack had transitioned from the notch stress field into the net section experiencing bulk stress, where damage is less than that experienced during strain control tests.

- At 20°C, the Coffin – Manson method gives accurate predictions of fully reversed (R= -1) DEN data, due to the method being based on R= -1 strain control data. R= 0 lives were overestimated, as a result of the actual tests experiencing a mean tensile stress, despite plastic deformation at the notch root forcing unloading into compression. This also accounts for the accurate prediction of R= 0 VCN data, due to the conditions at the notch root matching those of R= -1 strain control tests.

- The Walker strain method gave adequate notch life predictions at 20°C for R= 0 and R= -1 test conditions. It also results in reasonable predictions at 450°C for R= 0.

## 8.0 FUTURE WORK

- Initiation tests with a 2 minute dwell, in order to compare with cyclic initiation tests, to see how dwell affects initiation life at high temperature in DEN specimens.
- Load control DEN tests (cyclic and dwell) at higher $K_t\sigma_{max}$ in order to compare with plain specimen strain control and load control VCN data at these higher stresses.
- Strain control dwell tests below 1% strain range.
- Repeat strain control cyclic and dwell tests at 450, 500 and 550 to help reduce scatter and resolve the trends seen in these tests.
- Vacuum tests at 500C, dwell and cyclic
- Vacuum dwell and air dwell at 450C
- Vacuum crack propagation, dwell and cyclic.
- Further VCN testing at higher peak stresses
- Isothermal pre-exposure tests followed by fatigue (with and without prestrain) to explore the effects of alpha case on crack initiation.

## 9.0 REFERENCES


Allison, J.E., PhD Thesis, Carnegie Mellon University, Pittsburgh, Pa., 1982.

Baik, S. & Raj, R., Mechanisms of creep-fatigue interaction, Metallurgical Transactions 13A, 1982, p.1215-1221.

Bache, M.R., Talseem, M., Fatigue life prediction techniques for notch geometries in titanium alloys, International Journal of Fatigue 21, 1999, p.187-197.

Bache, M., A review of dwell sensitive fatigue in titanium alloys: the role of microstructure, texture and operating conditions, International Journal of Fatigue, 25, 2003, p.1079 – 1087

Bomberger, H.B., The general corrosion resistance of titanium, Titanium for the Chemical Engineer, DMIC Memorandum 234, 1968, p.29-34.

BS 3518, 'British Standard Methods of fatigue testing', British Standards Institution.

BS 7270, 'British Standard Method for constant amplitude strain controlled fatigue testing', British Standards Institution.

Coffin, L.F., A study of the effects of cyclic thermal stresses on a ductile metal, Transactions of the American Society of Mechanical Engineers 76, 1954, p.931-950.

Coffin, L.F., Fatigue at high temperatures, ASTM STP520, 1973, p.744-782.

Coles, A., Material considerations for gas turbine engines, Mechanical Behaviour of Materials, K.J. Miller & R.F. Smith, vol. II, Pergamon Press, Oxford, 1980, p.3-11.

Collings, E.W., The Physical Metallurgy of Titanium Alloys, ed. H.L. Gegel, American Society for Metals: Metals Park, Ohio, 1984.

Demulsant, X., Mendez, J., Influence of environment on low cycle fatigue damage in Ti-6Al-4V and Ti6246 titanium alloys, Materials Science and Engineering A, 219, 1996, p.202 -211

Donachie, Jr., M.J., Introduction to Titanium and Titanium Alloys, from Titanium and Titanium Alloys Source Book, ed. M.J. Donachie, Jr., American Society for Metals, Metals Park, Ohio, 1982, p.3

Donachie, Jr., M.J., Titanium and its alloys, Materials Engineering 79-80, 1974, p.61-70

Duquette, D.J., Enviromental effects I: General fatigue resistance and crack nucleation in metals and alloys, Fatigue and Microstructure, ed. M. Meshii, Metals Park: American Society for Metals, 1979, p.335-363.

Evans, W.J., Bache, M.R., McElhone, M., Grabowski, L., Environmental interactions with fatigue crack growth in alpha/beta titanium alloys, International Journal of Fatigue, Vol. 19, no. 1, 1997, p.177 – 182.

Evans, W.J., Microstructure and the development of fatigue cracks at notches, Materials Science and Engineering A, 263, 1999, p.160-175.

Evans, W.J., Bache, M.R., Nicholas, P.J., The prediction of fatigue life at notches in the near alpha titanium alloy Timetal 834, International Journal of Fatigue, Vol. 23, 2001, p103 – 109

Evans, W.J., Design against Fatigue and Fracture, Course notes, 2003, Materials Engineering Dept., University of Wales, Swansea, p.61-63

Evans, W.J., Jones, J.P, Bache, M.R., High-temperature fatigue/creep/environment interactions in compressor alloys, Journal of Engineering for Gas Turbines and Power, Vol. 125, p. 246 – 251, 2003

Evans, W.J., J.P. Jones, J.P., Williams, S., The interactions between fatigue, creep and environmental damage in Ti 6246 and Udimet 720Li, International Journal of Fatigue, 27, 2005, p.1473 – 1484

Flower, H.M., High Performance Materials in Aerospace, Chapman & Hall, 1995, p.105-112.

Foerch, R., Madsen, A., and Ghonem, H., 1993, "Environmental Interactions in High Temperature Fatigue Crack Growth of Ti-1100," Metall. Trans., 24, p. 1321.

Ford, B., Creep - Fatigue - Environment Interactions in Titanium 6246 for Compressor Disc Applications, PhD thesis, University of Wales, Swansea, 2002.

Ford, B., Creep - Fatigue - Environment Interactions in Titanium 6246 for Compressor Disc Applications, PhD thesis, University of Wales, Swansea, 2002.

Forsyth, P.J.E. & Ryder D.A., Fatigue fracture, Aircraft Engineering 32, 1960, p.96-99.

General Principles for Fatigue Testing of Metals, International Organization of Standardization, Geneva, 1964

Ghonem, H., and Foerch, R., 1991, "Frequency Effects on Fatigue Crack Growth Behavior in a Near Alpha Titanium Alloy," Mater. Sci. Eng., 138, pp. 69–81.

Goodman, J., Mechanics applied to Engineering, Longman Green, London, 1899.

Gough, H.J. & Sopwith, D.G., Atmospheric action as a factor in fatigue of metals, Journal of the Institute of Metals 49, (1932), 93-122.

Haigh, B.P., Report on alternating stress tests of a sample of mild steel received from the British Association Stress Committee, Report of the Brtitish Association 85, 1915, p. 163-170.

Haigh, B.P., Experiments on the fatigue of brasses, Journal of the Institute of Metals 18, 1917, p.55-77.

Henaff, G., Odemer, G., Tonneau-Morel, A., Environmentally-assisted fatigue crack growth mechanisms in advanced materials for aerospace applications, International Journal of Fatigue, 2007.

Irwin, G.R., Analysis of stresses and strain near the end of a crack traversing a plate, Journal of Applied Mechanics 24, 361-364.

Lesterlin, S., Sarrazin-Baudoux, C., and Petit, J., 1995, "Temperature- Environment Interactions on Fatigue Behaviour in Ti6246 Alloy," Titanium'95: Science and Technology, edited by P. A. Blenhinsop, W. J. Evans, and H. Flower, eds., The Institute of Materials, The University Press, UK, p. 1211–1218.

Lesterlin, S., Sarrazin-Bardoux, C., Petit, J., Effects of temperature and environment interactions on fatigue crack propagation in a Ti alloy, Scripta Materialia, Vol. 34, No. 4, 1996, p.651 – 657

Lutjering, G., The influence of processing on microstructure and mechanical properties of ($\alpha$+$\beta$) titanium alloys, Materials Science and Engineering A, 243, 1998, p.32-45

Mailly, S., Effect de la temperature et d'l'environment sur la resistance a la fatigue d'ailliages de titane, Phd Thesis, L'Universite de Poitiers, 1999.

Majumdar, S. & Maiya, P.S. A mechanistic model for time-dependent fatigue, Journal of Engineering Materials and Technology 102, 1980, p.159-167.

Manson, S.S., Journal of Experimental Mechanics, Volume 5, No. 7, 1965, p.193-226.

Meyn, D.A., Observations of micromechanisms of fatigue crack propagation in 2024 aluminium, Transactions of the American Society for Metals 61, 1968, p.42-51.

Mitchell, M., Fundamentals of modern fatigue analysis for design, Fatigue and Microstructure, ed. Meishi, M., Metals Park: American Society for Metals, 1978, p. 385 – 437.

MMM 31002, 'Crack propagation in corner crack test pieces – test procedure', Rolls Royce document, 15th May 1995.

Neeraj, T., Savage, M.F., Tatalovich, J., Kovarik, L., Hayes, R.W., Mills, M.J., Observation of tension-compression asymmetry in $\alpha$ and $\alpha/\beta$ titanium alloys, Philosophical Magazine, vol. 85, 2 & 3, 2005, p. 279-295.

Manson, S.S., Behaviour of materials under conditions of thermal stress, National Advisory Commission on Aeronautics: Report 1170, Cleveland: Lewis Flight Propulsion Laboratory, 1954

Neuber H, Theory of stress concentration for shear-strained prismatical bodies with arbitrary nonlinear stress-strain law, Transactions, ASME, Journal of Applied Mechanics, 1961;28:544-550.

Paris, P.C., Gomez, M.P. & Anderson, W.P., a rational analytic theory of fatigue, The Trend in Engineering 13, 1961, p.9-14.

Paris, P.C. & Erdogan, F., a critical analysis of crack propagation laws, Journal of Basic Engineering 85, 1963, p.528-534.

Pelloux, R.M.N., Mechanisms of formation of ductile fatigue striations, Transactions of the American Society for Metals 62, 1969, p.281-285.

Pelloux, R.M.N., Crack extension by alternating shear, Engineering fracture mechanics 1, 1970, p.697-704.

Petit, J., Mendez, J., Berata, W., Legendre, L., and Muller, C., 1992, "Influence of Environment on the Propagation of Short Fatigue Cracks in a Titanium Alloy," *Short Fatigue Cracks*, edited by K. J. Miller and E. R. de los Rios, eds., Mechanical Engineering Publications, London, ESIS13, pp. 235–250.

Pitt, F., Ramulu, M., Post-processing effect on the fatigue behavior of three titanium alloys under simulated SPF condition, Journal of Materials Engineering and Performance vol. 16(2), 2007, p.163

Remy, L., Pineau, A. & Thomas, B., Temperature dependence of stacking fault energy in close-packed metals and alloys, Materials Science and Engineering 36, 1978, p.47-63.

Riedel, H., Fracture at High Temperatures, Springer-Verlag, Berlin, 1987.

Sarrazin-Baudoux, C., Modelling of fatigue-corrosion in Ti6246 alloy at 500°C, Fatigue Fract Engng Mater Struct, 28, 2005, p.1161-1168.

Seagle, S.R., Bartlo, L.J., Metals Engineering Quarterly, ASM, vol. 8, 1968, p.1-10

Soderberg, C.R., Factor of safety and working stress, Transactions of the American Society of Mechanical Engineers 52, 1939, p.13-28.

Schubert, R., Low Cycle Fatigue, Ph.D.thesis, Technische Universität Braunschweig, 1989

Si-Young Sung, Young-Jig Kim, Alpha-case formation mechanism on titanium investment castings, Materials Science and Engineering A, 405, 2005, p.173–177

Suresh, S., Fatigue of Materials, Cambridge University Press, Cambridge, 2003, p.11-14, 91-92, 221, 224-226.

Walker, K., Effects of environment and complex loading history on fatigue life, ASTM STP 462, 1970, p.1-14.

Westergaard, H.M., Bearing pressures and cracks, Journal of Applied Mechanics 61, 1939, p.49-53.

Wohler, A., (1860) Versuche uber die Festigkeit der Eisenbahnwagenachsen, Zeitschrift fur Bauwesen 10, English summary, Engineering 4, 1867, p.160-161

Zappfe, C.A. &Worden, C.O., Fractographic registrations of fatigue, Transactions of the American Society for Metals 43, 1951, p.958-969.